University of Stavanger

FACULTY OF SCIENCE AND TECHNOLOGY

MASTER'S THESIS

Study programme/specialisation: Engineering Structures and Materials, Mechanical systems	Spring semester, 2020 Open
Author: Minas Birihane	
Programme coordinator: Professor Vidar Folke Hansen Supervisor(s):	
Title of master's thesis: Microstructure and Mechanical properties of a Reversed Engineered Inconel 625 Produced by Direct Energy Deposition	
Credits: 30	
Keywords: Inconel 625 Direct Energy Deposition Additive manufacturing Reverse engineering Microstructural investigation Mechanical properties	Number of pages: 76 + supplemental material/other: 7 Stavanger, 15.07.2020

Master Thesis

Microstructure and Mechanical properties of a Reversed Engineered Inconel 625 Produced by Direct Energy Deposition

Minas Birihane

July 2020

Abstract

The purpose of this study is to investigate the micro-structural and mechanical properties of reverse engineered Inconel 625 manufactured by direct energy deposition (DED). A costume made 4kW robotized DED machine was used for the manufacturing of specimens. Mechanical and micro-structural properties of the specimens are studied in as-build condition and after heat treatment for 60-, 120- and 300 minutes at 1175°C. This study provide a comparison of micro-structural and mechanical properties of as-build and heat treated specimens. Mechanical properties of the specimen are studied by performing Vickers hardness and tensile test. Analysis of the micro-structural properties is performed using scanning electron microscope (SEM), transmission electron microscope (TEM), X-ray spectroscopy (EDS), electron backscatter difraction (EBSD) and X-ray diffraction (XRD). It was found that the super alloy is very durable and shows average hardness (HV5) of 257.7HV in as-build condition which decreased to 215HV on heat treatment (30 min) due to reduction of residual stress and relaxation of dislocations. Difference in mechanical properties is observed within the specimen e.g hardness differs from top to bottom. Change in tensile strength is observed in as-build and heat treated specimens. The tensile test resulted in a brittle fracture in both as-build and heat treated specimens. As-build specimens showed cellular and columnar structures, while equiaxed structure and coarse grains are observed in heat treated specimens. Welding defects such as cracks and pores are also observed in both as-build and heat treated specimens. EBDS shows misorientation angle of most of the grains is between 1° to 3.5° in as-build specimen and 0° to 60° on the 300 minute heat treated specimen. It is observed that recovery of grains happened in the heat treated specimens. However, there was no evidence of recrystallization in any of heat treated specimen. No precipitates or any change in chemical composition was observed in heat treatment (1175°C) specimens. The hardness, yield strength and residual stress of additive manufactured (AM) Inconel 625 super alloy decrease on heat treatment while the alloy become more ductile.

Acknowledgements

I would like to thank Professor Vidar Hansen for providing me the opportunity to conduct this thesis and improve my knowledge and understanding of super-alloys. He has been supportive and encouraging throughout this period and providing me the motivation and constant guidance.

I am thankful to Head Engineer Johan A. Thorkaas and Senior Engineer Wakshum M. Tucho for their guidance, support and helping me with specimen preparations and other lab works. I would also like to thank Professor Biljana, Pejova for performing the X-ray diffraction analysis. Appreciation is also due to RD Engineer Pål Idar Ingebo from Westad Industri AS for providing the additive manufactured specimens used in this project.

Nomenclature

keV	$1.60217662 \times 10^{16}$ joules
k	Coefficient of proportionality, k= 5.65
HMS	Environment health and safety
HT	Heat treatment
HIP	Hot isostatic pressing
S_o	Original cross section area
L_o	Original guage lengt
σ_R	Residual stress
SDSS	Super duplex stainless steel
HV	Vickers hardness
σ_Y	Yield stress
STL	Standard tessellation language

Glossary

Alloy A metal made by combining two or more metallic elements, especially to give greater strength or resistance to corrosion.. 1

Dendritic structure A dendrite in metallurgy is a characteristic tree-like structure of crystals growing as molten metal solidifies, the shape produced by faster growth along energetically favourable crystallographic directions.. 25

HIP Hot isostatic pressing (HIP) is a manufacturing process, used to reduce the porosity of metals and increase the density of many ceramic materials.. 27

Micro-strain A strain with a magnitude of ($\mu\epsilon$) ϵ x 0.000001.. xii, 61

Precipitation hardening Precipitation hardening, also called age hardening or particle hardening, is a heat treatment technique used to increase the yield strength of malleable materials, including most structural alloys of aluminium, magnesium, nickel, titanium, and some steels and stainless steels.. 8

Recrystallization Recrystallization is defined as the process in which grains of a crystal structure come in a new structure or new crystal shape.. 2

Solute particles Solute particles can be atoms, ions, or molecules, depending on the type of substance that has been dissolved.. 14

Solution heat treatment Solution treatment is a broad term in heat treating used to refer to the heating of a material to temperatures sufficient for the dissolution of its soluble phases.. 2

Stress-relief treatment Stress relieving is a heat treatment process in which a metal is subjected to a constant temperature that is below the metal's critical temperature, followed by controlled cooling.. 26

Thermal stress ($\sigma_{thermal}$) Thermal stress is stress caused by differences in temperature or by differences in thermal expansion. . viii, 18

Contents

List of Figures

List of Tables

1 Introduction

The industry's need for metals having high weldable properties, high corrosion resistance, high tensile and yield strength at elevated temperatures have lead to several years of research and experiments for development of such metals. By investigating several effects of alloying elements on the basic Ni-Cr-Mo-Nb Alloy system, the patent for Inconel 625 was issued to H.L Eiselstein and J.Gadbut in 1964 [1]. Since today's metallic manufacturing developments are creating a highly competitive metals, the use of additive manufacturing technology in the metallic manufacturing industry seems to be unavoidable.

There are some defects observed with the additive manufacturing (AM) products (alloys). In order to produce a reliable and consistent product, micro-structural and mechanical properties (yield strength and hardness) have to be investigated. For development of such alloys, additive manufacturing process is a revolutionary step. The two most common AM categories used for metal or alloy printing are Powder Bed Fusion (PBF) and Direct Energy Deposition (DED). Commonly used techniques to print metals by PBF and DED are shown in Table 1 [2].

Table 1: Techniques used to print PBF and DED metals [2].

Powder Bed Fusion (PBF)	Selective Laser Sintering (SLS) Selective Laser Melting (SLM) Direct Metal Laser Sintering (DMLS) Electron Beam Melting (EBM)
Direct Energy Deposition (DED)	Laser-based DED Arc - Directed Energy Deposition Electron Beam Directed Energy Deposition (EB-DED)

This thesis project comprises a comprehensive study of the micro-structural and mechanical properties of Inconel 625 alloy. The Laser-based DED was used to manufacture the specimen that is used for the experimental work. DED can be used to manufacture large structures, this technology have high potential for commercialization and research opportunities.

1.1 Aims and Objectives

The objective of the thesis is to investigate properties of Inconel 625 super alloy, that is produced by Laser-based DED. The properties that are aimed to be studied include:

1. Residual stress in additive manufactured Inconel 625 and effect of heat treatment on residual stresses.
2. Micro-structural integrity of the super alloy.
3. Investigation of top, middle and bottom of the flat bar specimen for differences in hardness.
4. Strength of the specimen after different heat treatment duration at the same temperature.
5. Recrystallization after heat treatment.

The objectives are achieved by solution heat treatment of the small flat bar specimens of Inconel 625 alloy. Observing the flat bar specimens under optical Microscope (OM), scanning electron microscope (SEM), and transmission electron microscope (TEM). X-ray diffraction (XRD) studies of the specimen is also performed.

The SEM is used for observation of the grain structure and existence of any carbides, dendtric or intermetallic phases and other precipitates. TEM is used to observe the precipitate phases and dislocation. XRD is used examine the existence of the precipitate phases. Hardness test is performed to observe the changes due to stress relief on heat treatment. Solution heat treatment of tensile bar specimen is also applied to examine the change of the yield strength.

1.2 Manufacturing and Demand of Inconel 625 super-alloy

Inconel 625 alloy can be manufactured by both PBF and DED. Properties of the super alloy manufactured using different processes vary from each other as described by researchers such as Giulio et al. [3]. Super alloy used for this research is printed using laser based DED explained in section 2.4.2.

The demand for a fast production and delivery of a complicated, critical and non-critical high quality products have caused the acceptance for the use additive manufactured products in the offshore and sub-sea industries. There will be an increase in demand of additive manufactured commercial products in near future [4].

1.3 Importance of the research

Effect of heat treatment on residual stresses, micro-structural integrity of the Inconel 625 alloy that is manufactured by DED is not well understood now. Difference in hardness due to thermal diffusion effect between top, middle and bottom of the flat bar specimen is also not well known. The response of the alloy on heat treatment and re-crystallization process due to impact of heat is not well studied. Observing existence and extent of precipitated phases in the alloy also need to be studied. There is always room for improvement of these products, and that's why this research is necessary. This research intend to provide critical insight of the properties in AM Inconel 625 super alloy in as-build condition and after being exposed to high temperatures. Understanding these mechanical and micro-structural properties are important for making decision for using the super alloy in manufacturing components for several industries like offshore, aerospace, turbines etc. Information about micro-structural changes in the alloy after heat treatment is also studied, that is important for use of the alloy in parts exposed to high temperatures. The research also provides an insight of the changes in the properties of alloy from top to bottom of the specimen that are important for durability and strength.

1.4 Limitations

Due to Covid-19 situation it was challenging to perform all the tests and experiments that have prohibited to study all the properties of the alloy properly. It was intended to study the specimens in more detail, but the research was restricted due to restrictions on use of lab and equipment due to lock down.

2 Literature Review and Theory

Published data related to the topic are studied to understand the problem. The reviewed publications were evaluated by comparing their observation and results found against each other. Metal additive manufacturing (AM) have a great advantage over the metal manufacturing using the conventional techniques as mentioned by Arrizubieta, Jon Iñaki, et al. [5]. According to Yan et al. [6] the alloys manufactured by AM technologies have relatively small heat zone of heat effect, the grain size is finer along with other good properties. Along with high temperature and pressure bearing capacity the alloy material formed by DED allows easy printing of the complex parts [7].

There are various types of DED systems that are explained in Table 1. A stream of raw material along with a concentrated energy source is used for the manufacturing of super alloy like inconel 625. The concentrated energy source and the raw material stream meet at a common focal point, this process is performed in the presence of inert shield gas. Raw material is melted around the the point where it meets the concentrated energy stream and alloy is made due to melt pool formation [7].

2.1 Supper Alloys

Super alloy is made by combining alloy metals to heat and wear resistant metals to enhance their properties. Alloy elements such as aluminum, titanium and chromium are added in significant amount to a mixture of elements to make a super alloy [8]. Super alloy products are resistant to high temperatures, corrosion, oxidation, creep, rapture and maintain strength at the high temperatures [9]. Super alloys are used in offshore valves, chemical industry, sea water systems, oil and gas production facilities and other high temperature applications.

Micro-structural and mechanical properties of common metals changes at high temperature. This cause the metal to lose its strength when operating at high temperature such as in power plants, jets, oil and gas production and processing units. this result in causing creep and mobility of dislocations due to vacancy diffusion, where atoms move to the lattice of its neighboring site creating new deformation failure [10]. For metals operating at high temperature these

types of defects can be restrained by designing an alloy that can withstand high temperature conditions [10]. A super alloy is excellent heat resistant, have high dimensional stability, retain stiffness, have high strength and toughness [11].

There are three main classes of supper alloys [11];

1. Nickel base.
2. Nickel-iron base.
3. Cobalt base.

This thesis deals with the properties of nickel-base supper alloys. Inconel 625 super alloy have wide range of application and is discussed in this thesis.

2.2 Inconel 625 (N06625)

Choosing a material for a part depends on several factors such as cost, availability and mechanical properties [12]. Inconel 625 is a nickel based alloy which is used within petroleum, offshore industry and aeronautical industry. It is very expensive material and used only when highly durable material is required to tolerate high temperature, pressure and corrosion. As Inconel 625 alloys has high corrosion resistance, great strength, excellent fatigue strength, good weld-ability, and is oxidation resistance at high temperatures. It is also resistant against nitric, hydrofluoric and phosphoric acid solutions. Therefore, it is used in aggressive environments that pose the challenges mentioned above [13]. Chemical composition of AM Inconel 625 super alloy is shown in Table 2. .

Table 2: Chemical Composition of Alloy 625 (N06625) [14]

Chemical	**Weight Percent (wt%)**
Chromium	20.0 - 23.0
Molybdenum	8.0 - 10.0
Cobalt	1.00 max
Columbium + Tantalum	3.15 - 4.15
Aluminum	0.40 max
Titanium	0.40 max
Carbon	0.10 max
Iron	5.00 max
Manganese	0.50 max
Silicon	0.50 max
Phosphorus	0.015 max
Sulfur	0.015 max
Nickel	Balance

Elements mentioned in Table 2 are combined in certain weight percentages to make good quality Inconel 625 super alloy. Each alloying elements have certain physical and chemical properties. Depending upon these properties each element impacts the properties of super alloy.

2.3 Effects of Alloying Elements on Nickel-Base Alloys

Nickel keeps a constant FCC structure until its melting point, making it the key element in designing metals operating at high temperatures [15]. However, by adding alloying elements such as Cr, Mo, Al, Ni, Fe, W, C, Ti, Cu, and Co the micro-structural and mechanical properties can be enhanced to obtain the desired characteristics in supper alloys. Some of these elements are carbide formers, which precipitates at grain boundaries and blocks grain boundary sliding [13]. Blocking of grain boundaries from sliding improves the strength and toughness of the super alloys [16].

Nickel alloys are very important as they have excellent properties. Evolution of nickel based alloys is shown in Figure 1. Inconel 625 was developed by adding Mo, Nb, Cr and Fe to nickel 200/nickel 201, that is highlighted in Figure 1 [17]. Impact of important elements persent in Inconel 625 alloy is discussed as following.

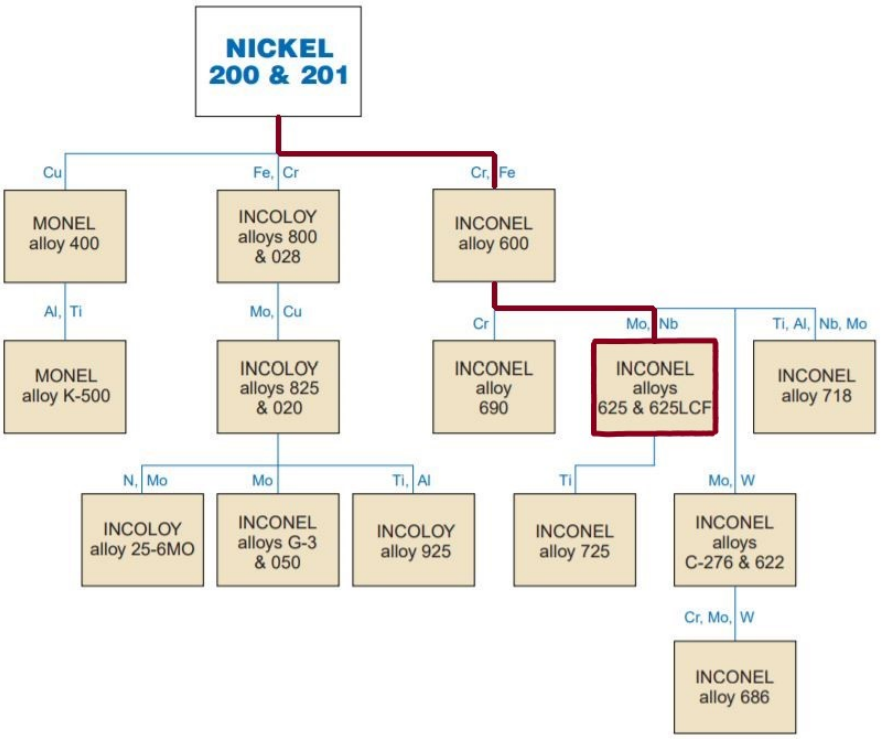

Figure 1: Supper alloys and alloying elements [17].

2.3.1 Nickel

Nickel improves resistance to stress crack corrosion and provides metallurgic stability. It also improves the materials strength at high temperature and increase resistance against carburization, halogenation, oxidation and nitridation [9].

2.3.2 Chromium

The amount of Cr added in alloys is in the range of 15% to 30%, there are some alloys which may have upto 50% Cr [9]. Adding Cr improves resistance to corrosion and oxidization against nitric and chromic acids like HNO_3 and H_2CrO_4. It also improves resistance to high temperature oxidation and hot sulfur bearing gases [9]. Hardness of Inconel 625 is improved due to presence of Cr [18].

2.3.3 Molybdenum

For metallic material, Molybdenum improves the strength for high temperature services. It also improves the resistance to pitting and crevice corrosion [9]. Ductility can be controlled by adding carbon and molybdenum, but the content should be controlled to prevent formation of inter-metallic phases [19].

2.3.4 Columbium (Niobium) + Tantalum

Elements like Columbium and Tantalum are used to give a high temperature strength by solid solution and Precipitation hardening mechanism. These elements are added as stabilizing elements that prevents inter-granular corrosion at grain boundaries due to carbide precipitation. Columbium (Niobium) makes it also possible for the metal to be weldable [9].

2.3.5 Aluminum and Titanium

Small amounts of aluminum and titanium is used for improvement of corrosion resistance. Combining these elements will enable age-hardenable material for applications in low and high

temperature. Adding aluminum promotes formulation of a material that can resist attack by oxidation at high temperature, carbourization and chloronation [9].

Table 3: Other alloying elements and their effects [2].

Carbon	Carbons helps prevent corrosion and provide strength at high temperature [9].
Iron	Iron is used to reduce costs, it provides nickel with resistance against H_2SO_4 and resistance to high temperature carburizing environments [9].
Manganese	Manganese improves tensile strength, hardenability and provides good corrosion resistance [20], it also prevents hot cracking in welds and control the effects of sulfur [19].
Silicon	Silicon provides resistance to oxidation during cyclic heating and improves material strength [9].
Sulfur	Sulfur reduces grain boundary cohesion and decreases tensile ductility [21]. It can also be harmful to the metal but it is controlled by addition of manganese and magnesium [19]
Phosphorus	Phosphorus resists attack by hydrochloric acid and increases stress rupture life, creep life and ductility [21].

2.4 Additive Manufacturing (AM)

Additive manufacturing (AM) is one of the processes that are used to manufacture Inconel 625 super alloy. The specimen of Inconel 625 super alloy that was used in this study was produced using AM.

Additive manufacturing is actually an old technology, sewing cloths and gluing wood are also considered additive manufactured products. With additive manufacturing complicated and large assembly products can be produced with fewer pieces, reducing time and weight. Mobile AM facilities can also be used to reproduce or repairement of defected parts all over the world. Hence, AM also contributes in increasing a products life-time and reduce the usage of resources [22].

2.4.1 Additive Manufacturing of Metals

Additive manufacturing of metals is a process where the metallic components are started from the bottom and built upwards incrementally layer by layer. The metals that are usually printed using AM are aluminum, titanium, inconel, stainless steels, nickel alloy with good mechanical property. In the micro-structural level, investigation of the grain size is the main interest for material engineers and how dislocations and grain size effects the mechanical properties. Grain size can be controlled using AM, which leads to production of alloys with desired properties. [22].

The procedure of an additive manufactured part consists of several steps. The process starts with The concept design, where the idea is first generated and further modeled using a 3D modeling software to visualize the 3D design. The 3D model is then saved as an .STL format where the desired set-up are applied in the AM software. The AM software is used to control the printing process such as the scaling, build volume, orientation for printing, building support material etc. The 3D model is sliced into layers and sent further for printing. Post processing is performed by removing the support material, machining or assembling of parts [23].

The 3D designs can be stored, modified and used later if needed. 3D scanners are used to scan parts with complicated geometry with possibility of modification using CAD software. In the

coming years, the oil and engineering companies will be able to provide cloud services, where the designers can directly meet the service employer creating possibilities for outsourcing design jobs globally [22]. Figure 2 shows the AM process followed from the concept design to final product.

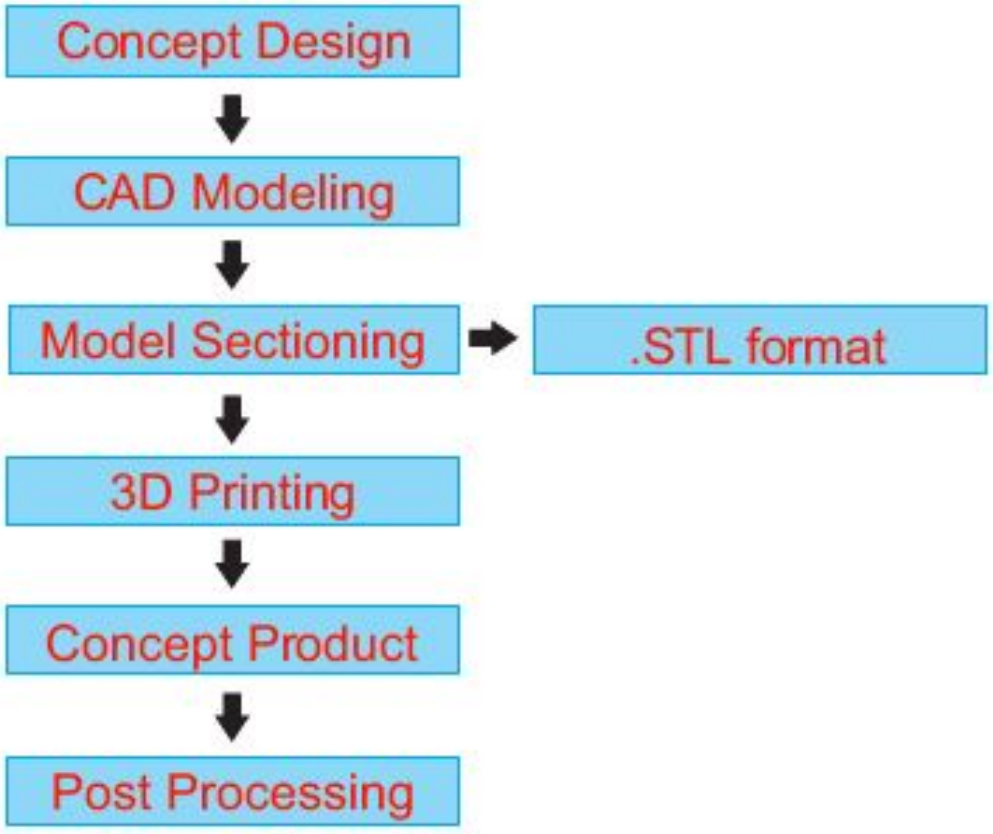

Figure 2: AM process diagram [24].

Additive manufactured Inconel 625 is mostly produced by Direct Energy Deposition (DED) and Selective Laser Melting (SLM) [3]. These two methods will be briefly explained, in this thesis DED method is used to produce the flat bar and the tensile bar specimens.

2.4.2 Direct Energy Disposition (DED)

In 1997 DED was commercialized for manufacturing of expensive aerospace parts that were made of titanium [2].

The Direct Energy Deposition is currently categorized into three processes, the Laser Engineered Net Shaping (LENS), the Electron Beam Freeform Fabrication (EBFF) and the Wire and Arc Additive Manufacturing (WAAM) [25].

The specimens used for this thesis was produced using LENS. In this process The metallic powder is delivered through a nozzle and directed towards a power output from a laser beam onto a melt-pool. The metallic powder is melted by the laser beam, solidifying the powder into a metal, by manipulating the spatial location and the melting pool. The metallic component is built layer by layer into a 3D part. The process is usually applied in a sealed chamber where oxidation of reactive metals can be avoided by applying inert gas (Argon) [25]. Figure 3 shows the several DED processes available today [7]. Figure 4 illustrates a schematic diagram of a DED, with a 2000 W laser energy, the part is built on the base plate [26]. Table 4 shows the advantages and disadvantages of the DED process.

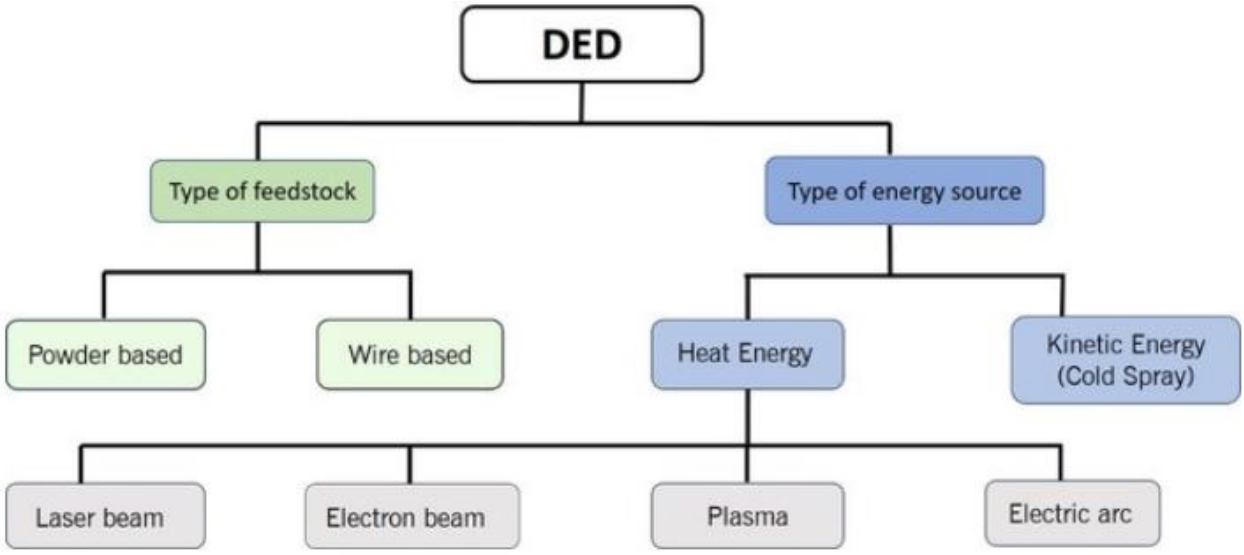

Figure 3: AM process diagram [7].

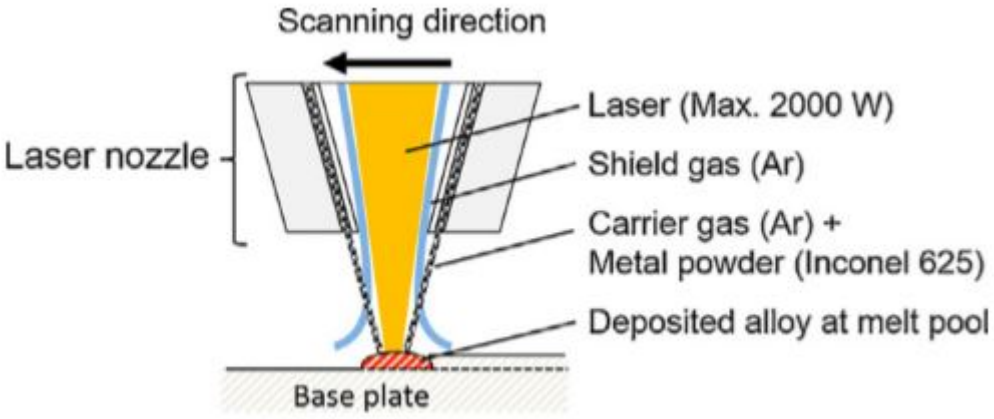

Figure 4: Schematic drawing of DED [26].

Table 4: Advantages and Disadvantages of DED [27].

Advantages	Disadvantages
Fast building rate	Expensive
Parts are built with good mechanical properties	Low build resolution
Require less post processing work	No support
Parts can be built with several different powders, custom alloys	
Easy to refill the feeding material	
Less material waste	

2.4.3 Common defects in material casted using DED

Following are the most common defects in DED casted materials.

2.4.3.1 Porosity

Porosity maybe induced during the process of casting. Porosity can be either inter-layer porosity or intra-layer porosity. If there is lack of input energy that is required to melt the input material then it will develop some un-melted regions this phenomena leads to inter-layer porosity [7]. Inter-layer porosity develops near the substrate. This type of porosity may also appear due to rapid cooling rate. Pores developed due to inter-layer porosity is irregular shaped and are large in size. Intra-layer porosity on the other hand is related to the entrapment of inert shielding gas. This porosity is distributed randomly, and the pores developed due to this type of porosity are round shaped. Intra-layer porosity usually occurs in areas that have lower cooling rates [7].

The characteristic of the initial powder also have impact on the porosity values [28]. If the initial powder have variable grain size, it will result in increase in porosity of final material. Given that it is important to control the size and shape of the powder to make a homogeneous alloy with less porosity [28].

2.4.3.2 In-homogenity

Solute particles redistribution occurs as several layers of the alloy are deposited during the AM. This redistribution leads to the formations of micro-structural bands of heterogeneous material that are known as heat affected zones. Apart from redistribution, solidification cooling rates also affect the homogeneity of the alloy. If the cooling rate is higher there is more possibility of element trapping and heterogeneity [7]. As a result of these changes, compositional in-homogeneity is developed in the alloy [29]. Different boiling points of elements present in the casting powder results in preferential vaporization of these elements, which contributes to increase in-homogenity. Several other factors contribute to the in-homogenity such as loss of stabilizers, that can lead to an increased hardness in the upper part of the alloy (built direction) [30].

2.4.3.3 Cracks

Cracks reduce the integrity and strength of the alloy. Micro-cracks are developed in the alloy due to abrupt change in heat. Subsequently heating also induce cracks in the alloy [31]. During cooling and solidification, the restriction of compression process will induce residual stresses and generate cracks in the alloy. Presence of porosity also eases the development of cracks in the alloy. The extent of the crack development in a alloy is dependent upon the composition or the raw material [32]. Delimitation i.e. the separation of the adjacent layers also induce cracking in the alloy [33]. Cracks may also be induced due to over heating of the specimen [34].

2.4.3.4 Fatigue

The fatigue behaviour of Inconel 625 is inconsistent [7]. Presence of defects such as cracks and pores influence the development of fatigue in the super alloys [35]. Presence of un-melted powder also decrease the fatigue life of the super-alloys [36]. Development of fatigue is influenced by in-homogeneity in the material [37]. Development of fatigue is also dependent upon the casting properties of the Super alloys, and are difficult to predict [7].

2.4.4 Selective Laser Melting (SLM)

Selective Laser Melting (SLM) is another AM method that can be used for manufacturing of Inconel 625. SLM has slower build rate but higher dimensional accuracy, higher relative density and higher mean value of hardness compared to DED [3].

SLM printing process starts with taking a thin layer of metallic powder that is spread across the build platform. A high-powered laser is used to melt the layer of metallic powder. The thickness of the layer vary between 20 μm - 100 μm. The next thin layer of metal powder is spread on top of the first layer which is laser melted again, the process is repeated until the desired product is achieved [22]. The laser beam source emits a power between 20 W and 1 kW, directed with a scan speed of 15 m/s across the build platform. Laser beams with single mode fibre lasers is applied. The laser continuously emit radiation with wavelength of 1060 nm – 1080 nm. The laser spot sizes are between 50 μm – 180 μm according to requirement [22].

There are some defects that can be found in the products such as small holes, cracks and pores. These defects can be reduced by adjusting the process parameters and conducting stress relief annealing [38]. Table 5 lists the advantages and disadvantages of SLM method. Figure 5 shows a schematic drawing of how the principle of SLM process works.

Table 5: Advantages and Disadvantages of SLM [22].

Advantages	The produced metals have high quality The system can build almost every type of metals Economically it have low cost compare to other AM processes Complex geometries can be produced The product is dimensionally accurate
Disadvantages	A large space is required for the parts High power consumption The process is relatively slow

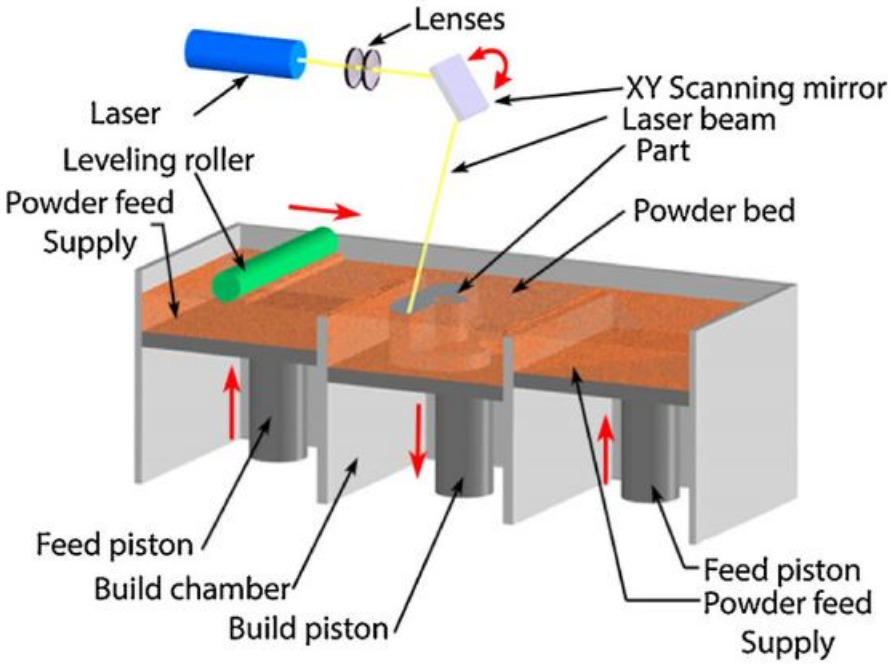

Figure 5: Schematic drawing of SLM [39].

2.5 Residual Stress

In the alloys created by AM process residual stress (RS) is caused by the repeated thermal cyclic effect, which applies to both DED and SLM. This results in causing undesirable changes in the mechanical properties that reduces the products life-time. Depending on which AM method is used, three types of residual stresses can be found which can be Macro-, Micro- and Sub-micro RS. Macro RS result in the change of final dimension of the part, Micro-RS results in change of size of grains and Sub-micro RS results in creating dislocations [40].

There are two reasons for the induction of residual stress in AM of metals. The first case is when both top layer and the previously solidified layer is melting during the printing process causing the material's behaviour and micro-structure to change. The second case for creation of the residual stress is repeated change in temperature caused during the heating and cooling cycles. During the heating phase the metal is supposed to expand but it becomes restrained by the low temperature in surrounding area causing a partially restrained shrinkage of the material. These cases can cause defects such as porosity, cracks and inclusions giving undesired mechanical properties [41].

Figure 6 shows the heating and the cooling phase of the AM process. When the laser is applied to the surface, during the heating phase (a), the top layer increase its strain (elongation) and the tension stress. After the removal of the laser, the cooling phase (b) causes the material to exhibit compression stress at the welded spot resulting in generation in the residual stresses [41].

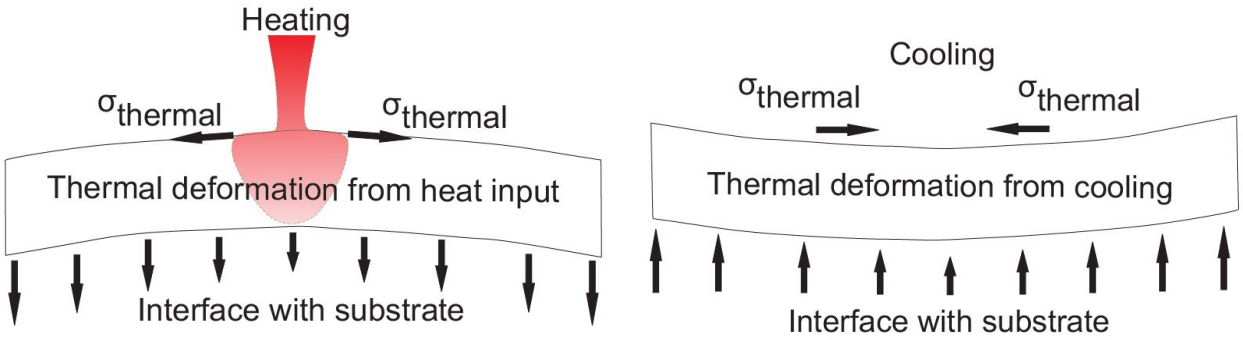

(a) heating phase. (b) cooling phase.

Figure 6: Thermal deformation at each cycle on a deposited layer, Thermal stress ($\sigma_{thermal}$) [41].

This RS results in problems like distortion, reduction in fatigue life and corrosion resistance etc [42]. The RS is a complicated problem to analyse and to solve. The RS can not be directly measured, several measurement techniques have been developed, which are based on measuring the strain value and applying the Young's modulus, Poisson's ratio and other engineering applications to calculate the residual stress value [43].

2.5.1 Measurement methods of residual stress

Measurements of residual stress can be implemented by three methods; destructive, non-destructive and semi-destructive [43]. There are several techniques that has been developed over the years but the most developed methods are the X-Ray Diffraction, Neutron Diffraction, Ultrasonic, Indentation and the Magnetic method [43]. Figure 7 presents the different categories of measuring methods used for residual stress measurements [43].

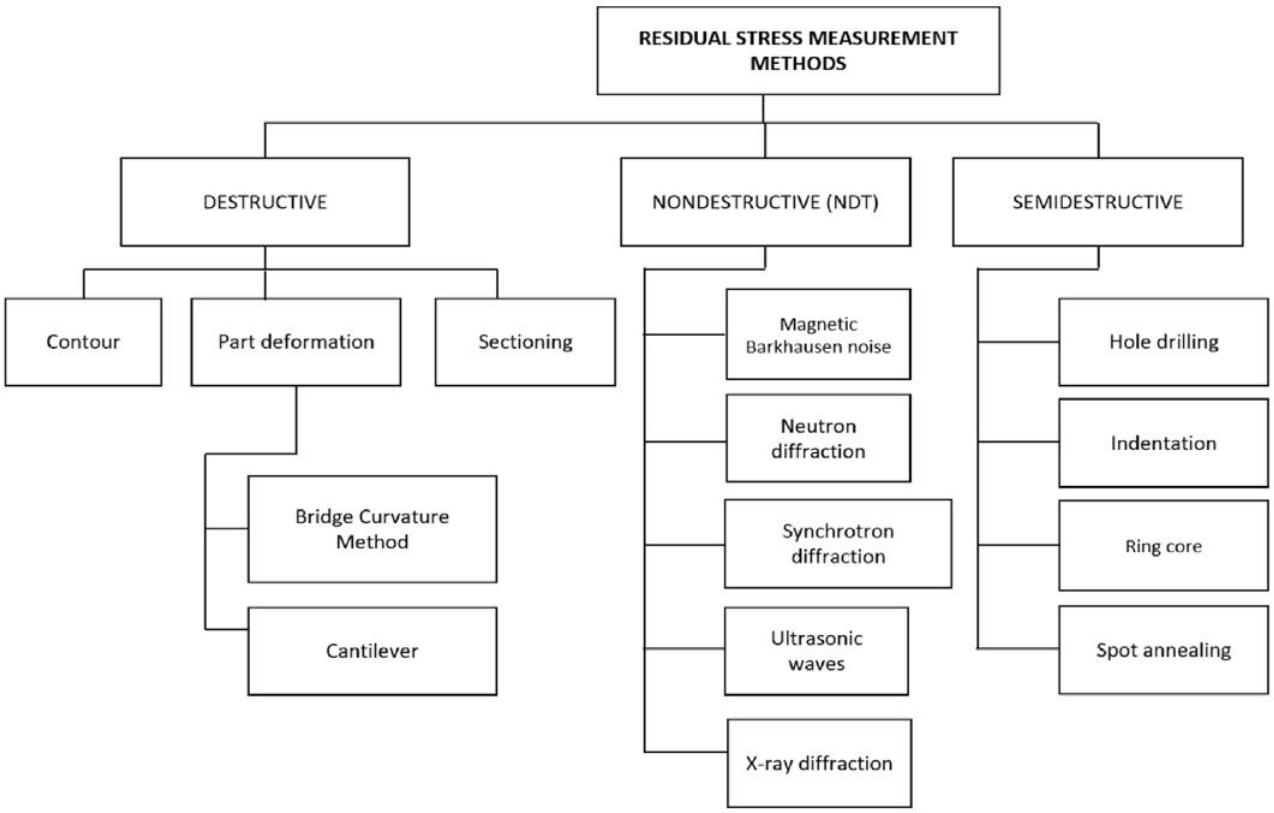

Figure 7: Residual stress measuring methods [43].

Certain measurement methods have advantages such as reliability, consistency, affordability and other methods have disadvantages such as high-cost, complexity, non-standardized, slow process and low accuracy [44]. The most common used measurement methods such as hole drilling, X-Ray diffraction, electron backscatter, ultrasonic, magnetic, neutron diffraction and synchrotron method will be briefly explained below [44].

2.5.2 X-Ray Diffraction Method

The X-ray diffraction method is a non-destructive testing method based on the Bragg's law principle. Currently there is no standard available for this testing method. The X-Ray beam hits the specimen at an angle that satisfies the Bragg's law, the beam interacts with the lattice planes and is reflected back to the detector. Measurements of the planes are taken at different angles, the strains are then calculated using certain equations. Depending on the material and the angle of incident, the X-ray interacts in a short distance below the surface of the specimen. In part 2.8.3 more details regarding XRD are presented [45].

2.5.3 Synchrotron Diffraction (SD)

Synchrotron diffraction (SD) have similar principle as XRD but uses a higher beam energy. SD method is a non-destructive test method (NDT) that is only applicable for poly-crystalline materials. This test method measures the change in the poly-crystalline lattice due to change in stress. SD can measure macro- and micro-stresses with high accuracy, thin specimens and shallow depths for up to 20 mm in steel and 100 mm in aluminum can also be measured. SD's good penetration capability make it possible to perform three residual measurements i.e. longitudinal, transverse and normal [46]–[48].

2.5.4 Neutron Diffraction (ND)

Neutron diffraction (ND) method is a non-destructive test method (NDT). The neutrons are generated by fission or spallation which interacts with the diffracting planes. These neutrons diffract only when the Bragg's law is satisfied, the diffraction pattern is then collected by the detector. Knowing the principle strain directions, three measurements can be taken along the longitudinal, transverse and normal. The changes in the lattice planes in the crystalline material are calculated using the elastic properties, where the RS is eventually obtained by applying the Hook's law [49].

2.5.5 High Angular Resolution Electron Backscatter Method (HR-EBSD)

HR-EBSD is considered as a robust and sufficient technique by the academics and the industry. The electron backscatter (EBSD) method is a non-destructive testing method that can be performed using scanning electron microscope (SEM). Details of EBSD are presented in part 2.9.2. The high angular resolution electron backscatter method (HR-EBSD) is used in wide range of studies for investigating within the field the deformation analysis. HR-EBSD differs from the conventional electron backscatter (EBSD) by the higher quality preparation of specimens and high quality sharp images. These patterned images of the Kikuchi lines are used to measure the change and comparing elastic strains obtained from a similar crystal structure with a known strain value, some details of Kikuchi lines are presented in part 2.8.1 [50]. Studies performed by Wilkinson, Angus J., and T. Ben Britton. suggests that using the change in inter-planar angles are the most successful methods used today for measure the strain values [50].

2.5.6 Ultrasonic Method (UT)

Ultrasonic testing (UT) method is a non-destructive test method (NDT) based on the similar principle as XRD but with more penetration depth. UT is performed by propagation of the ultrasonic waves into metals, the reflected waves is gathered by the detector and the acoustic signals are analyzed. Factors such as temperature, roughness and in-homogeneity can affect the results. UT is affordable, reliable and have high measuring accuracy. This method have disadvantages such as low spatial resolution. Measuring of the large volume of the specimen makes this test more suitable for macro-stresses. Depending on the acoustic theory, the propagation of the waves depends on the materials mechanical stress properties and the propagation speed. UT have several wave types, an ultrasound frequency between 20kHz and 5GHz is mostly preferred for RS measurements [43].

2.5.7 Magnetic Barkhausen Noise (MBN)

In both methods of XRD and ND, it is required to cut the specimen for preparation. The magnetic barkhausen noise (MBN) was developed as an NDT method for measuring the residual

stress without removing a part of a structure [51]. This measurement method is limited to ferromagnetic metals, the change on magnetisation's discontinuity between the domain walls and pinning sites causes the Barkhausen effect. The domain walls and pinning sites reacts according to the positive or negative magnetised barkhausen noise. The increase in tension stress shows a positive MBN and a decrease of a tension stress (compression) show a negative MBN value [52].

2.5.8 Hole Drilling Method

The hole drilling measurement method is standardized as ASTM E837. This method allows to accurately measure the residual stress in multiple directions for up to 2 mm depth, assuming the residual stress is homogeneous. This testing method is performed by drilling a hole in the metal with a special instruments, hole of a certain depth is drilled and the deformation near the hole is measured at different steps. This method is applied to assess the distribution of the residual stress versus depth [44].

2.5.9 Indentation Method

Indentation method is a semi-destructive method, instruments such as the Vickers or Rockwell B hardness test machine is applied for making indents on the surface of the material. The study of determining the RS using indentation methods has been conducted since 1932 by investigating the effects of strain on the hardness measurements [53]. Several methods have been suggested since the commercialization of instrumental indentation techniques. A reference specimen with no residual stress is usually used for comparison, but several measurement applications have been developed such that no reference specimens are needed. It is possible to measure RS based on observations of the indented surface, analyzing nano-indentations and simulation studies such as finite element simulation [54]. SEM with high imaging and measurement devices for examination of indentations on the surface have also proven to be an effective method for measuring RS [55].

For computational measurements and cross referencing of the experimentally obtained data, two sets of data are required, the material properties data and the Vickers hardness indentation data. Material properties data are studied by calculating Young's modulus (GPa), Poisson's ratio, yield strength (MPa) and effective elastic modulus (GPa). Vickers hardness indentation data include contact area, angle between opposite faces, indentation edge length, indentation height, diagonal length and the Vickers hardness value [55]. Equation (1) expresses the residual stress as a function of contact area and equation (2) expresses the contact area as a function of residual stress [55].

$$\sigma_R = \sigma_Y(0.7363 - 7.407\frac{P_{max}}{E_{eff^A}}) \tag{1}$$

Where, σ_R = Residual Stress (MPa), σ_Y= Yield Stress (MPa), P_{max}= max applied load (N), E_{eff^A} = Effective Elastic Modulus (GPa) [55].

$$A = \frac{P_{max}}{E_{eff(0.0994-0.135\frac{\sigma_R}{\sigma_Y})}} \tag{2}$$

where, A = Contact area across the surface, σ_R = Residual Stress (MPa), σ_Y= Yield Stress (MPa), P_{max}= max applied load (N), E_{eff^A} = effective elastic modulus (GPa) [55].

2.6 Microstructures of Inconel 625

2.6.1 Precipitates of Inconel 625 manufactured by casting

Nickel base supper alloys can be solid solution strengthened or precipitation strengthened. For application that require little strength, solid solution strengthening is applied. For application that require high strength (high temperature conditions), precipitation hardening strengthening method is applied. There are three major phases present in the as casted nickel-base supper alloy, gamma (γ) phase, gamma prime (γ') phase and carbides [12].

A small amount of aluminum can substitute any atom in a lattice, in supper alloys this phase is called Gamma (γ). By increasing the aluminum content the aluminum atoms will have the ability to arrange itself and occupy certain sites of the lattice creating a phase called gamma prime (γ') [12].

- Gamma (γ) phase: A continuous matrix of FCC (Face-Centered Cubic) austenite, that is solid solution strengthened by adding elements such as chromium, molybdenum, tungsten, cobalt, iron, titanium, and aluminum. A vacancy in a (γ) phase will allow any of the neighbouring atoms (nickel or aluminum) to occupy the vacant site. Having a Gamma prime phase inside a Gamma phase, the dislocation will be blocked and the diffusion at the boundary is slowed creating a high temperature material. The structure of a supper alloy is basically made of a gamma prime blocks within a gamma structure. The (γ') can be transformed into (γ) phase by evaporation of AL at high temperature [56] [12].

- Gamma prime (γ') phase: Nickel-base super alloy (γ') phase is $Ni_3(Al, Ti)$, and is strengthened by precipitation hardening heat treatments. The (γ') phase is an inter-metallic structure because it's structure wants to maintain it's ordered arrangement dislocation and atomic diffusion is restrained. A vacancy in a (γ') will only be occupied by an atom according to it's ordered arrangement i.e. a vacancy in an aluminum site will only prefer to be occupied by aluminum even though a nickel atom is closest to the vacant site. Dislocation movement makes the material ductile at lower temperature, in (γ') the dislocation is restrained giving a brittle material at room temperature. In common metals a high

amount of elements will cause inter-metallic phases causing brittle dislocation i.e. too high amount carbon in steel will make it brittle [56] [12].

- Carbide Phase: In nickel base super alloys, carbides have FCC crystal structure with carbon content 0.02 - 0.2 % for wrought alloys and 0.02 - 0.6 % carbon for cast alloys. Carbides in grain boundaries can effect the strength, ductility and creep properties. They can be advantageous by restraining grain boundary sliding. However, at continuous chain of carbides a fracture path is formed. The three common types of carbides formed in nickel base supper alloy are MC, $M_{23}C_6$ and M_6C [12].

- Topologically Close-Packed (TCP) phases: In nickel base super alloys, the TCP phases are formed either during heat treatment or service. These phases usually form thin plates and are undesirable because they can reduce rupture strength and rupture ductility. TCP phases, can also change the chemical composition by removing elements such as Cr, Mo and W reducing the solid solution strengthening. These phases are avoided by using an alloy design technique called phase composition (Phacomp) [12].

2.6.2 Precipitates of Reverse Engineered Inconel 625 Manufactured by using DED

The precipitates of the additive manufactured Inconel 625 are susceptable to carbides and intermetallic phases [57]. Publised data about microstructural study of Inconel 625 by the process of DED are very limited, which makes it difficult to assume whether there are any precipitates or which types of precipitates that are present.

A study of characterization of the Dendritic structure of a DED manufactured Inconel 625 was performed by Guru Prasad Dinda, using microhardness test. The difference between the as-build and annealed condition at the range of 700 - 1200°C, it was concluded that there was a suspicion of the existance of the precipitates and the partitioning of either γ'' or δ phases [58]. Another study performed by Giulio Marchese, using SEM and EDS, the Laves phases, Nb-rich carbides and γ'' phase were detected [3]. The common methods used to identify the phases are the chemical composition analysis and observing the shape of the phases. Due to the chemical composition similarities, lattice parameters and the limited data available makes it difficult to identify the available phases [57].

2.7 Heat Treatment

Inconel 625 are heat resistant alloys with good mechanical strength and resistance with surface degradation. It is high temperature tolerant due to presence of combination of the FCC structure and precipitation strengthening or solid-solution hardening [59].

the process of heat treatment of a casted Inconel 625 has been significantly improved since the mid 1960's. Common types heat treatments applied to Inconel 625 are solution treatment, and Stress-relief treatment. Heat treatment of performed to release the buildup stress due to residual casting, welding and machining. Annealing of metals can cause several affect of the mechanical and micro-structural properties [59]. Figure 8 show three processes that occur during annealing at different temperatures that are recovery, re-crystallization and grain growth. The behaviour of tensile strength, hardness, ductility and residuals stresses are also presented in Figure 8.

In the recovery process the crystals recover their basic structure, resulting in a small reduction in strength and small increase in ductility and a partial relief of residual stresses. The required recrystallization temperature and time depends on the material. In the recrystallization process the crystal structures change, increase in ductility is observed. Reduction in tensile strength, hardness and residual stress also occur. After the grain growth process there is no change in the mechanical and microstructural properties [60].

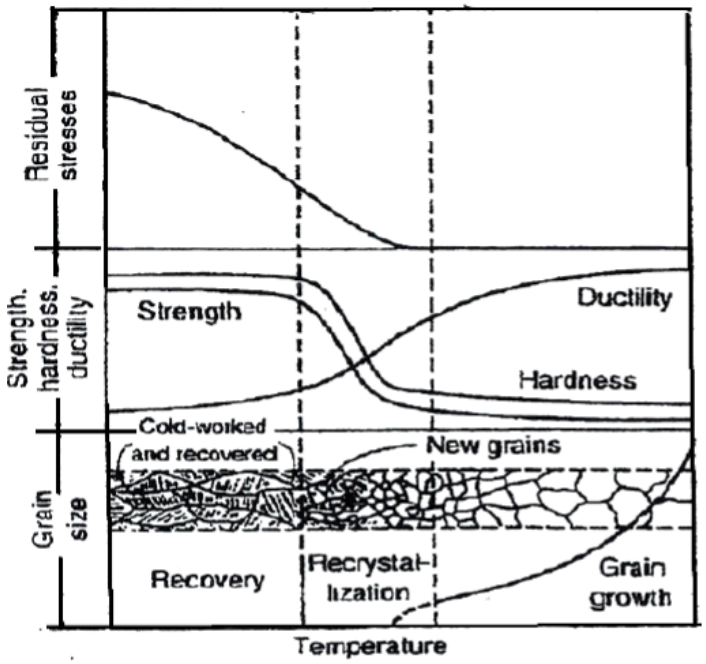

Figure 8: Effect of annealing on mechanical and micro-structural properties [60].

Solution treatment is applied to dissolve precipitates, the treatment is performed below melting point for a range of time followed by rapid cooling. Due to welding and machining processes the unwanted material properties can be removed by applying solution heat treatment [59].

Hot isostatic pressing (HIP) is mechanical property enhancement technique, where a high hydrostatic pressure and high temperature is uniformly applied to the metal. Inert gas Argon is used as a pressuring medium. HIP is used to improve the mechanical properties for supper alloys by eliminating internal porosity, increasing the density and helping to improve the resistance against corrosion. A study performed on AM of a Nickel based supper alloy 718 concluded that there is a significant reduction in pores and an increase of hardness by combining HIP and heat treatment (HIP+HT) [61].

The melting point for Inconel 625 produced by selective laser melting (SLM) is 1290-1350°C. Recrystallization occurs below the melting point, it reduces strength and hardness while increase ductility, giving undesirable properties in products for high temperature environment use [61].

In this thesis to observe the possibility for existence of any recrystallization the temperature of 1175°C is also observed.

2.7.1 Porpuse of Use

Stress relief heat treatment is applied to remove the buildup stress within the material without causing any phase transformation. The stress relief heat treatment are performed at temperatures high enough to cause recrystallization. By not performing a stress relief treatment, the dimensions of finished product might experience a change in with time [59].

2.7.2 Technical Specification

The Oven used in this thesis work is a Nabertherm LH 30-12 model with a P 300 controller. The oven is a 400V, 3 Phase and have a 7kW heating power. The oven provides heat on four sides and a heating capacity up to 1200°C.

2.8 Electron Microscope

The electron microscope is used to visualize and analyze specimens in a sub-atomic levels. An electron is a negatively charged particle of an atom, with a wavelength of 400 - 700 nanometer (nm). Electrons are 2000 times lighter than the smallest atom and can easily be stopped when hitting a material. Vacuum inside the electron microscope helps prevent the electrons hitting other particles in the air causing the loss in the retrieved data. Accelerated electron in a vacuum acts as light, while their wavelength is 100 000 times smaller than the light's wavelength [62].

The electron microscope consists of parts that are placed inside a column such as an electron gun, condenser lens, objective lens, scan coils and aperture. The electron beams are produced by heating the tungsten filament. At high acceleration voltage stable electromagnetic lenses are required in order to provide a high resolution image. According to where the electron beam hits the specimen, there are two types of electron microscopes, scanning electron microscope (SEM) and transmission electron microscope (TEM). Table 6 shows the properties of optical and scanning electron microscope [62].

Table 6: Optical microscope versus Scanning Electron Microscope [62].

Microscope	Magnification	Depth of Field	Resolution
Optical Microscope (OM)	4x - 1000x	15.5mm - 0.19 mm	0.2mm
Scanning Electron Microscope (SEM)	10x - 3000000x	4mm - 0.4mm	1 - 10nm

2.8.1 Scanning electron microscope (SEM)

SEM is used to obtain high resolution images of specimens. SEM's main applications are topography, morphology, composition, and crystallographic information (grain boundaries, grain arrangements) [62].

The focused beams of electrons generated by the electron gun scans the surface of the specimen. Reflected electrons are detected by electron detectors and used to generate images. The electrons are accelerated to an energy of 1 kilo electron-volt (keV) and 30keV. The acceleration voltage influences the penetrating strength of the electron beam into the specimen surface. Electron generated from the electron gun hits the surface of the specimen and kicks out an electron from an atom of the specimen and produce a number of signals such as secondary electron (SE) and the backscatter electron (BSE), X-ray and auger electrons. The signals are collected by the detector from each point of the surface, amplified and displayed on the screen. Figure 9 shows a schematic illustration of the different parts used in SEM [62].

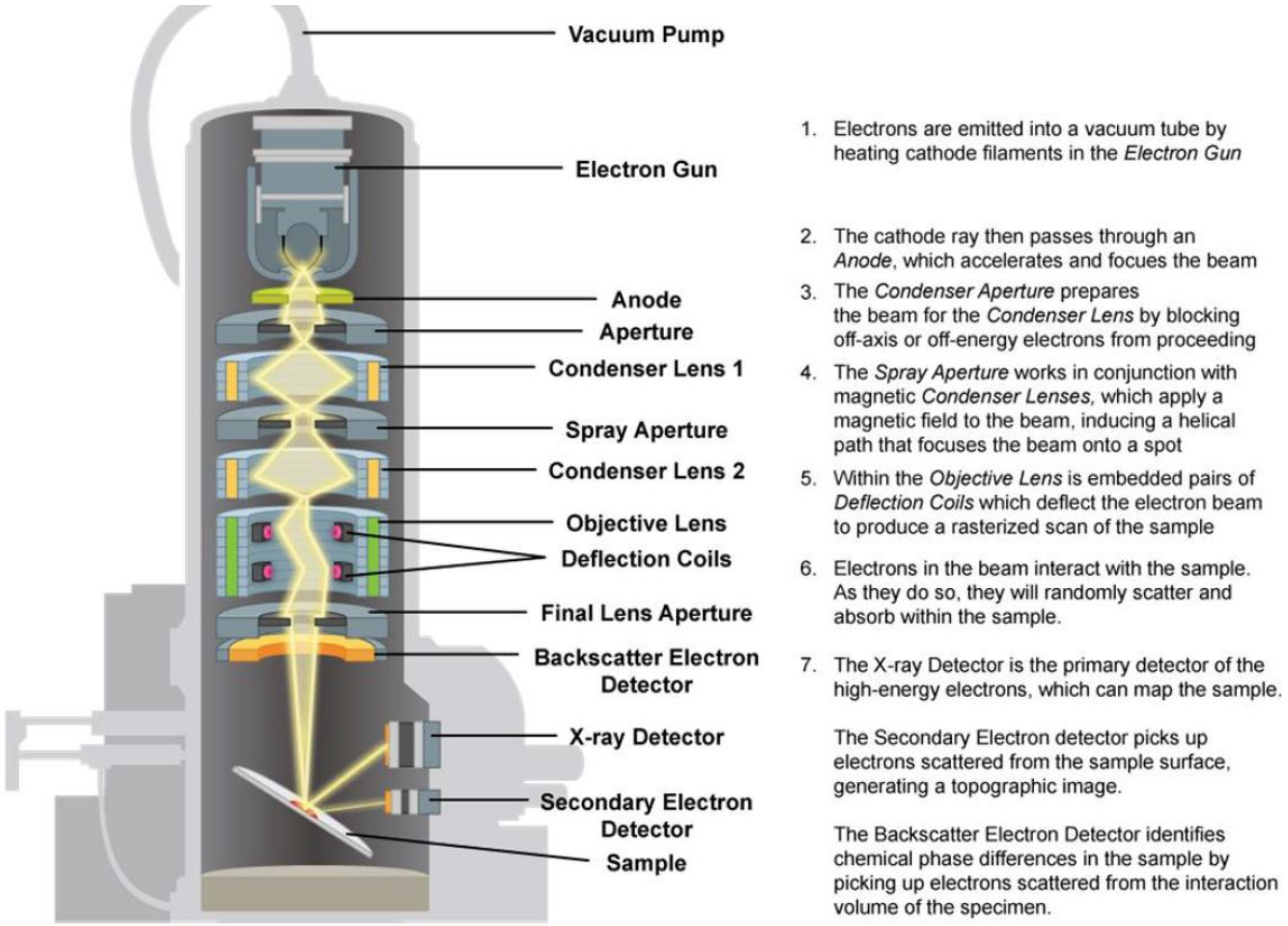

Figure 9: Schematic illustration of SEM [63].

When the incident beam interacts with the specimen, different detectors are used to collect the reflected electrons from the specimen. These detectors are placed in a range of solid angle where the different signals can be accepted and received. The detectors should be efficient by allowing an increased amount of signal percentage to be detected. The electrons that are gathered by the detectors are the Secondary electrons (3eV - 5 eV) and the back scattered beam electrons. Detectors listed in Table 7 are used in SEM to detect SE, BSE and X-rays signals [62].

Table 7: Signals and Detectors in SEM [62].

Detector	Signal	Recommended Current	Information Detected
Everhart Thornley Detector (ETD)	SE	1 - 200pA	Surface Topography
Through the Lens Detector (TLD)	SE	1 - 200pA	Surface Topography
Backscatter Electron Detector (BSED)	BSE	50pA - 2nA	Atomic (Z) contrast
Energy Dispersive Spectroscopy (EDS)	X-ray	100pA - 10nA	Elemental Composition
Wavelength Despersive Spectroscopy (WDS)	X-ray	100pA - 10nA	Elemental Composition

When the incident beam hits the surface and penetrates the specimen, the electrons get absorbed and are scattered randomly in a balloon shaped volume shown in Figure 11, this region is called the interaction volume. The interaction volume increases with the increase of the beam energy. SE, BSE and X-ray signals are released from different parts of the interaction volume. The signals that manage to reflect and escape to the surface are detected and the rest remain inside or get lost [62].

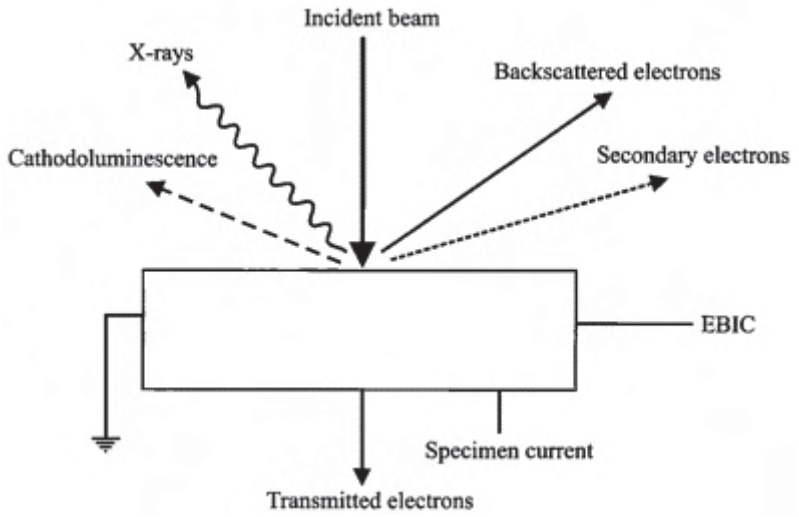

Figure 10: Signals that can collect from SEM [62].

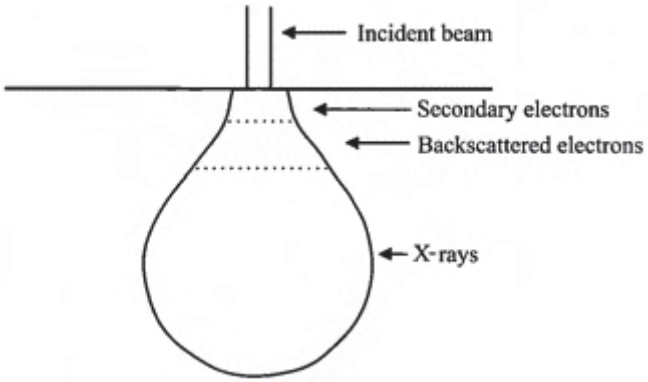

Figure 11: Interaction volume of the electron beam within the specimen [62].

When the incident beam penetrates the specimen and interacts with an atom it knocks out an electron out of it's place from the K, L or M shell called as secondary electron. The knocked electron emits signal that is detected by the detector (ETD). Information collected is used to form a topology image [62].

When the incident beam strikes the specimen and scatters elastically is called as back-scattered electron. Few electrons from the incident beam travel around the positively charged nucleus of the atom and are reflected back again with out slowing down. Different elements have different nucleus sizes. Larger nuclei size (with larger atomic number, Z) will increase the probability of the BSE reaching the detector. The information collected from the detector is used to create a gray-scale image of the surface with the different phases and elements presented on the specimen [62].

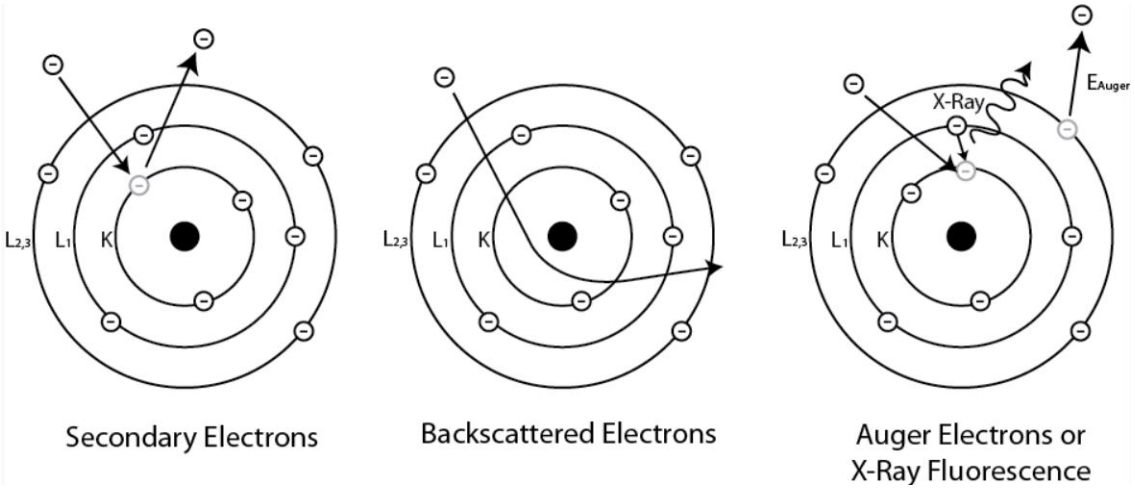

Figure 12: Emission of secondary-, backsatter- and Auger electrons [62].

When the incident beam interacts with an atom and kicks out an electron from the lower energy or inner shell is called as auger electron or X-ray. In order to fulfill the atomic equilibrium and occupy the vacancy an electron from the higher energy shell is transferred to the vacancy to the lower energy shell. The difference between the energy will cause the ejection of the auger electron. The Auger Electron Spectroscopy (AES) is used for surface elemental analysis [62].

Energy Dispersive Spectroscopy (EDS) or Wavelength Dispersive Spectroscopy (WDS) detectors are used for obtaining the the elemental composition mapping. EDS uses all the collected x-ray signals at the same time, while WDS collects a single x-ray signal at given time only when the Bragg's law is satisfied [62].

Bragg's Law:

$$n\lambda = 2d \sin \Theta \tag{3}$$

where, λ = wavelength, n= order of diffraction, d= lattice plane distance, θ = angle of the x-ray incident.

Electron backscattered difraction (EBSD) is the technique use in SEM and TEM to obtain the diffraction pattern data. In SEM the specimen is tilted 70° to help more electrons escape from surface of specimen. The image is transmitted into a phosphorous screen and is recorded using a sensitive camera. The image is analyzed by a software and the pattern which is known as the Kikuchi lines. The software measure the pattern and the angles between the lines and compares the image to the predicted stored pattern [62].

2.8.2 Transmission electron microscopy (TEM)

Transmission electron microscopy is a microscopy technique in which a beam of electrons is transmitted through a specimen to form an image. The specimen is cut as an ultra thin section usually less than 100 nm thick or as a suspension on a grid. A magnified image is then formed and focused onto an imaging device such as a fluorescent screen, a layer of photographic film or a sensor such as a scintillator attached to a charge coupled device [64].

The image is formed from the interaction of the electrons with the specimen as the beam is transmitted through the specimen. The transmission electron microscope combines several measurement techniques, as such imaging, diffraction and several other forms of spectroscopy, this can be done simultaneously at the same area of the specimen. This means that TEM has the capability of returning an extraordinary variety of measurement information [64].

Unlike the SEM that operate at normally low acceleration voltages (less than 30KV), TEM operate at accelerating voltage values between 100 KV and 300 KV. The higher the accelerating voltage is, the thicker the crystals the electrons may penetrate. For example, at 100 KV, the maximum thickness is in the order of 200 nm and at 200 KV it is at 1000 nm. High acceleration voltage results in the wavelength of the electrons being very small which in turn helps in achieving a high resolution in the images formed [64].

Diffraction patterns are generated by adjusting the magnetic lenses such that they face focal plane of the lens rather than the imaging plane. For crystalline specimens, this produces an image consisting of a pattern of dots in the case of a single crystal. The reflected electrons are scattered from the incident beam by both elastic and inelastic processes. Elastic scattering (Bragg scattering) changes only the direction of electrons, where as the inelastic scattering changes both direction and speed (energy). The diffraction pattern from cubic crystals are analyzed by indexing. Crystallographic direction and dislocations are determined by Burger's vector [65]. Figure 13 illustrates schematic drawing of TEM.

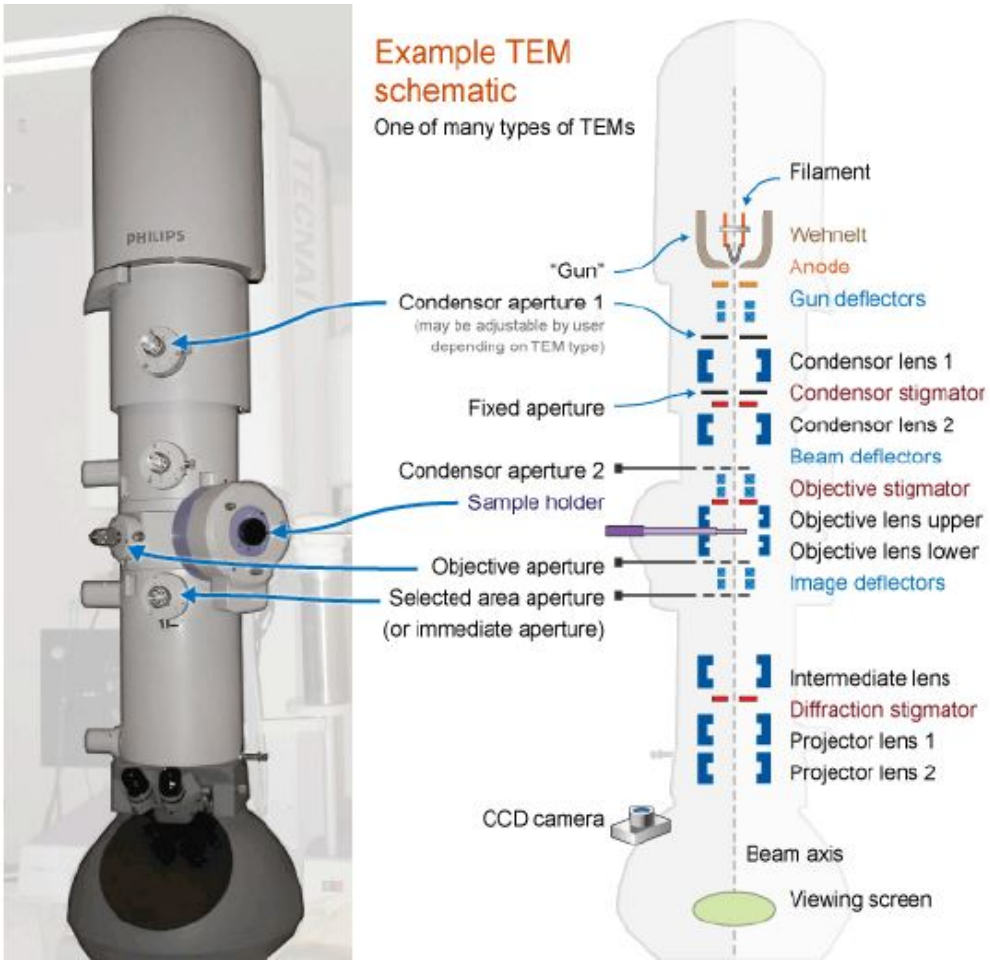

Figure 13: Schematic drawing of TEM [63].

2.8.3 X-ray Diffraction (XRD)

XRD is used to accurately measure the average spacing between latices, to find and determine the orientation of crystal structures and measure the stresses in a crystals. The change in the micro-structural details is used to detect and identify the presence or dissolution of the precipitates. This method is effective for polished specimens with flat surface [66].

The detector moves around the stationary specimen at each angle of 2θ, collects and records the X-ray diffraction data. The diffraction patterns are used to identify the phases and the diffraction peak positions can be used to calculate the unit cell dimensions. The unit cell lattice parameters can be calculated by converting the peak positions 2θ into d_{hkl} values using bragg's law [67]. Williamson-Hall approach (Equation 5) is used in this project to calculate the strains.

$$d_{hkl} = \frac{\lambda}{2\sin\theta} \tag{4}$$

$$\beta(\theta) = \frac{\kappa \cdot \lambda}{d \cdot cos\theta} + \frac{4 \cdot \epsilon \cdot sin\theta}{cos\theta} \tag{5}$$

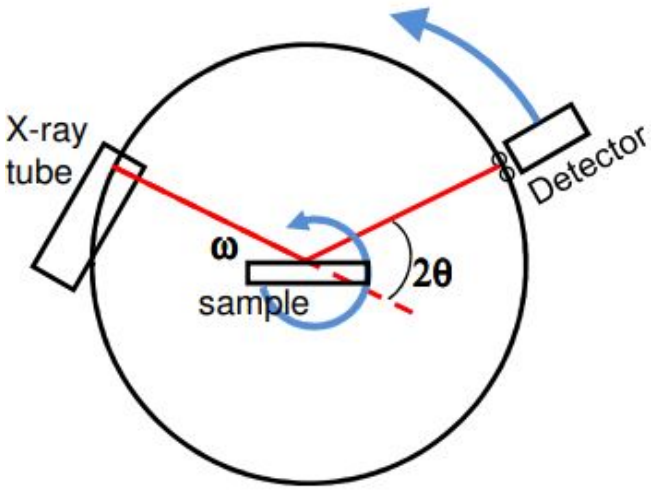

Figure 14: Schematic drawing of XRD [67].

2.9 Mechanical properties of Inconel 625

2.9.1 Tensile test

Tensile test is fundamental test that is universally applied to find the mechanical properties of a material. Properties such as Young's modulus, yield strength, elongation (%), area of reduction (%). The test data gathered from the tensile test can also be used for better material selection [68].

A uni-axial tensile test is performed by applying external load on the specimen until failure. The test procedure is performed following the specifications of ISO (the International Organisation for standardization). ISO 6892-1:2019 standard is an international guideline used for designing standardized tensile test specimens at room temperature. Iso 6892-1 is a test performed at room temperature 10°C to 35°C. The relationship between the original guage length (L_o) and the original cross section area (S_o) is defined by the following equation [68].

$$L_o = k\sqrt{S_o} \tag{6}$$

2.9.2 Hardness

Vickers hardness test is the most frequently used test to investigate the mechanical properties because of it's inexpensive, simple and other properties such as the tensile strength can also be estimated. The size of the indentation is measured and calculated. The result describes the surface's resistance against deformation. A soft material will have a large indent size giving low hardness value. While, hard material will resist surface deformation giving a higher hardness value [68]. A diamond with a pyramid shape tip is used to indent the surface of the specimen with a load ranging from 1 to 120 kg. If larger load is applied (i.e. HV10) a larger area of the indent surface is covered, but if the applied loads HV5 and HV10 gives the same values, HV5 can be selected to perform several indents. In this thesis, EN ISO 6507-1:2018 standard is followed.

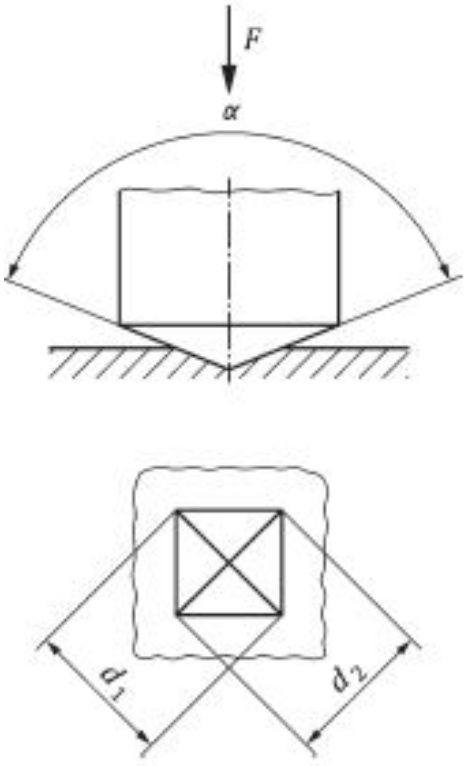

Figure 15: Schematic drawing of Vickers hardness test Indent [69].

$$HV = 1.854\frac{F}{d^2} \tag{7}$$

where, HV = Vickers hardness, F= load in kgf, d= mean value of d1 and d2 in mm.

3 Methodology

In order to investigate and gain more understanding of the microstructural and mechanical properties of the additive manufactured Inconel 625 produced by DED, several experiments have been performed to collect the necessary data for this thesis. The experiments and analysis is performed at the University of Stavanger's laboratory machines and electron microscopy labs. The data collected is used for quantitative and qualitative analysis e.g Vickers hardness, ultimate tensile strength and yield strength. For HMS purposes, experiments that included use of chemicals were performed under the supervision of lab assistants. In addition, the SEM, TEM and XRD experiments were performed by the lab assistants. A full detail of the experimental methods used are explained in this part.

3.1 Introduction

The laboratory experiments were performed using certified machines, following the standards and HMS regulations at UiS labs. A robotized DED additive manufacturing machine was used to print Inconel 625. A flat bar and tensile testing specimens were printed, machined and delivered by the Westad Industri AS.

The flat bar and tensile specimens are solution heat treated at 1175°C for 30-, 60-,120- and 300 minutes. Images from the optical microscope (OM) will be used for observation of pores, cracks, grain structures. Comparison of as-build and heat treated specimen is performed. The images from SEM will also be used to observe the precipitates and other segregated elements. The hardness test values will be compared with each other, and also to examine the relaxation of the residual stress in the specimens.

A 3D printed flat bar was cut, heat treated, mounted, grinded, polished and etched. Specimens were observed using optical and electron microscope. Finally the hardness was tested. The testing procedures were performed according to ISO standards and using certified instruments. In this experiment, the flat bar is oriented in the X, Y and Z axes. The flat bar was cut into smaller pieces for specimen preparation. The surface sections that were used for investigation were the XZ-section and the YZ- section. Figure 16 includes the schematic drawings that shows the labeling of the surface sections. Figure 17 shows a schematic diagram of the top, middle and bottom surfaces that were investigated for the X-ray diffraction analysis.

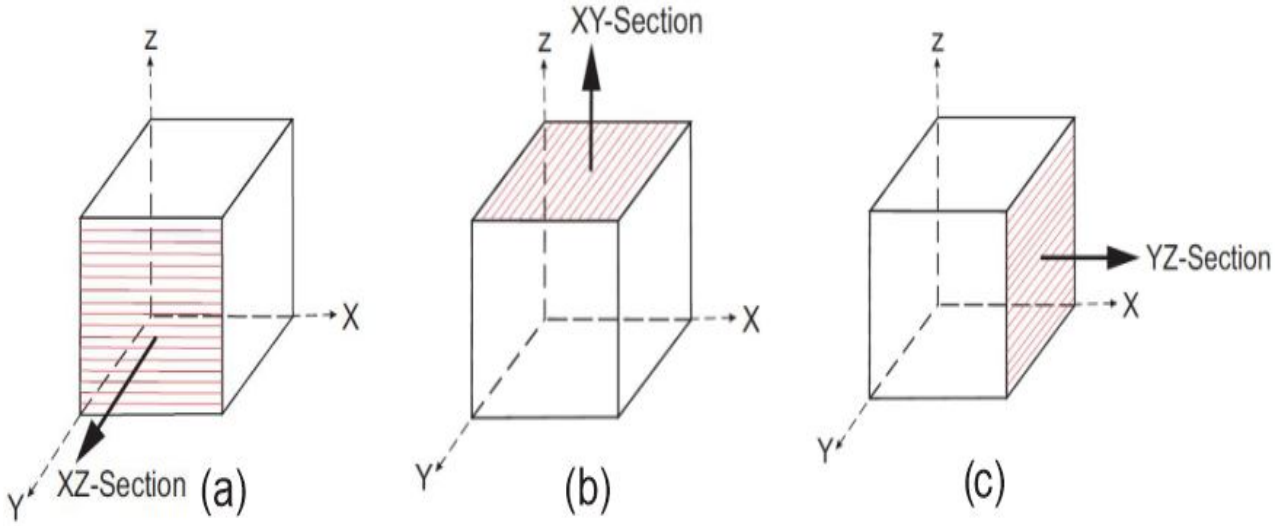

Figure 16: Schematic drawing of the sections= a. XZ-Section, b. XY-Section, c. YZ-Section.

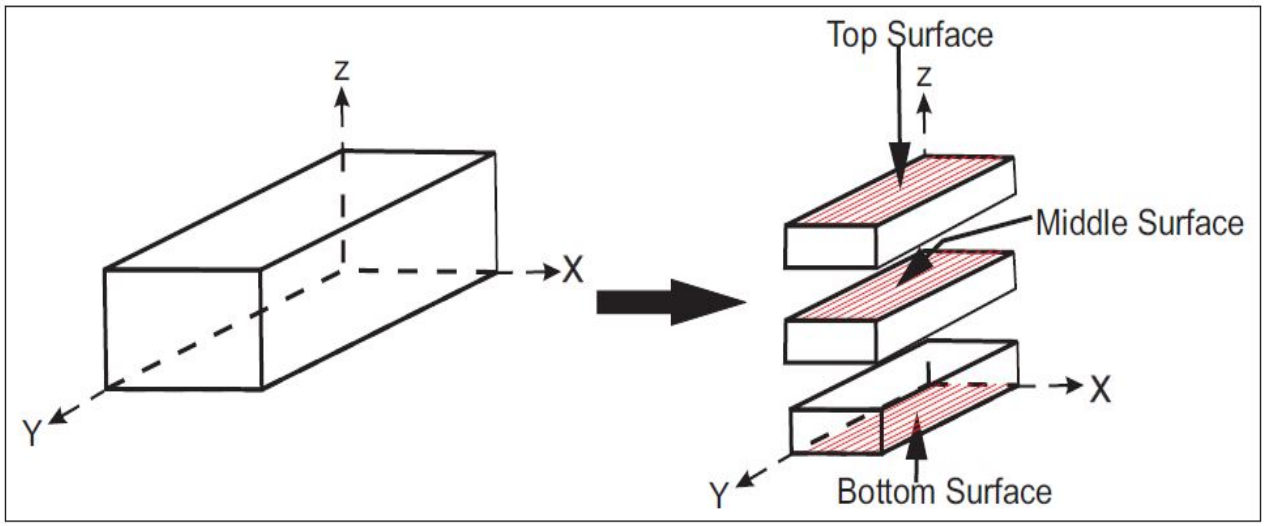

Figure 17: Schematic diagrams of surfaces examined in XRD

3.2 Direct Energy Deposition (DED)

The 3D printed specimens were manufactured and delivered by Westad Industry AS, the DED-powder certification is attached in the appendix. A Stellite-6 coated AISI 316L stainless steel was used as the base metal. The stellite-6 coating prevents the base metal for corrosion and preserve the properties at elevated temperatures [70]. The flat specimen was printed along the x and y directions, the layers were stacked along the z directions. The y-axis is called LD (longitudal direction), x-axis is called as TD (transverse direction) and the z-axis is called as BD (building direction). Table 8 describes labeling of the printing direction according to the axis. Figure 18 shows how the deposition pattern of the layers that were built along the BD.

Table 8: Description of the axis and their printing directions.

Axis	Discription
X-axis	Transversal direction (TD)
Y-axis	Longitudinal direction (LD)
Z-axis	Building direction (BD)

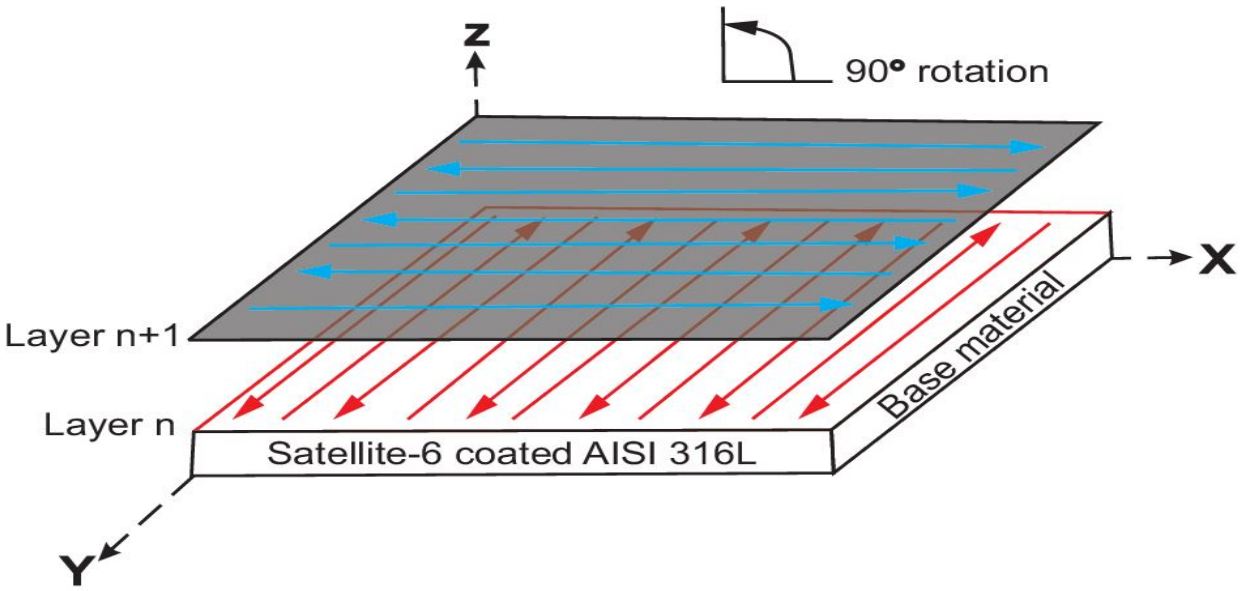

Figure 18: Longitudinal and transversal deposition layers, satellite-6 coated AISI 316L base metal.

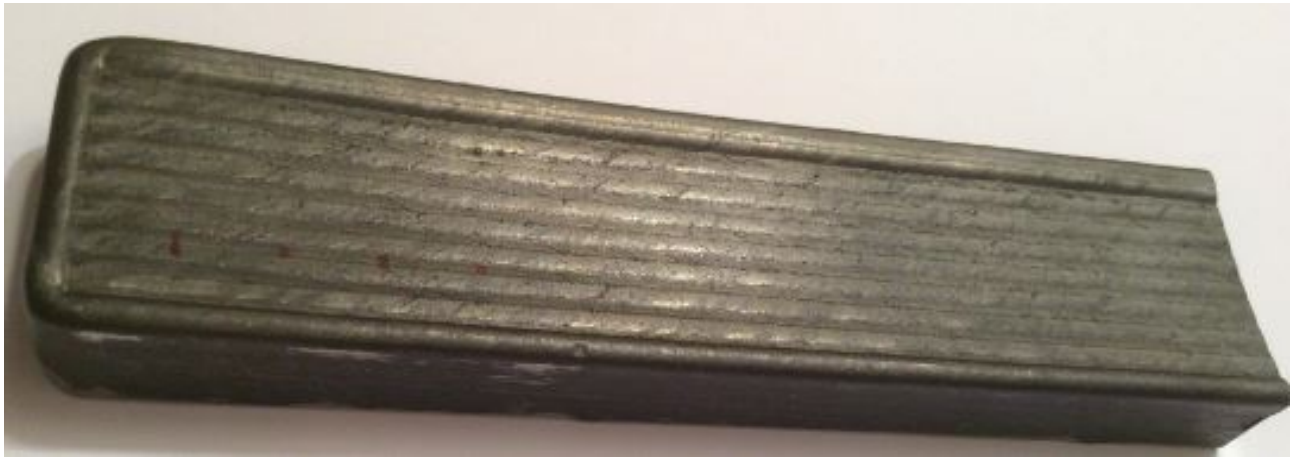

Figure 19: Additive manufactured flat bar specimen 200x30x14 mm.

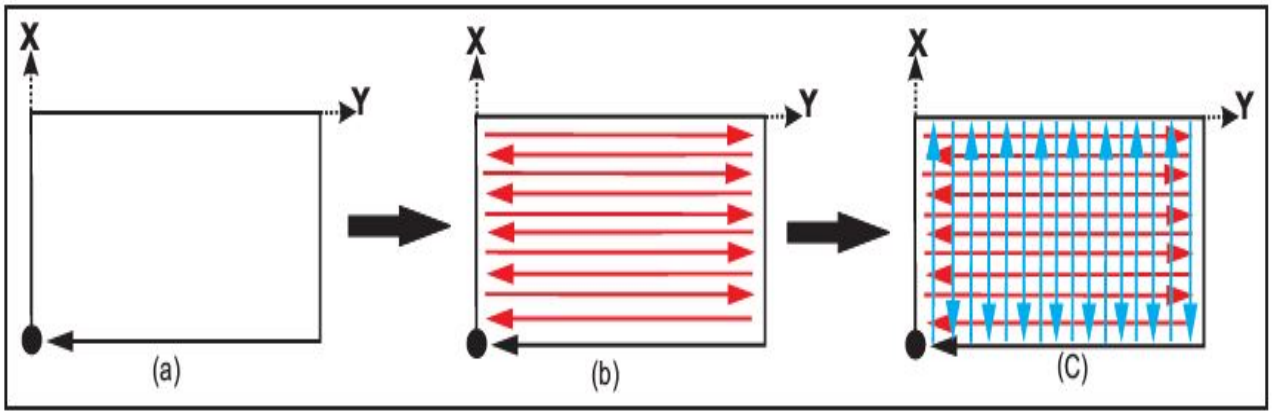

Figure 20: Schematic drawing of printing steps of the flat bar.

The flat bar's dimension of 200x30x14 mm was approximately determined in order to prepare enough specimens for SEM, TEM and XRD anaylsis. Figure 20 show the steps that were used in the printing process. In figure 20 (a) is the initial printing path, (b) the longitudinal path. The supper alloy is printed within the boundaries of (a) along the y-direction forming the first layer. For the second layer (a) is printed to create a boundary and a transverse path with a 90° rotation is printed along the x-direction within this boundary. This pattern is repeat until the final part was produced as shown in Figure 19. Figure 21 shows DED set-up for the tensile test specimens.

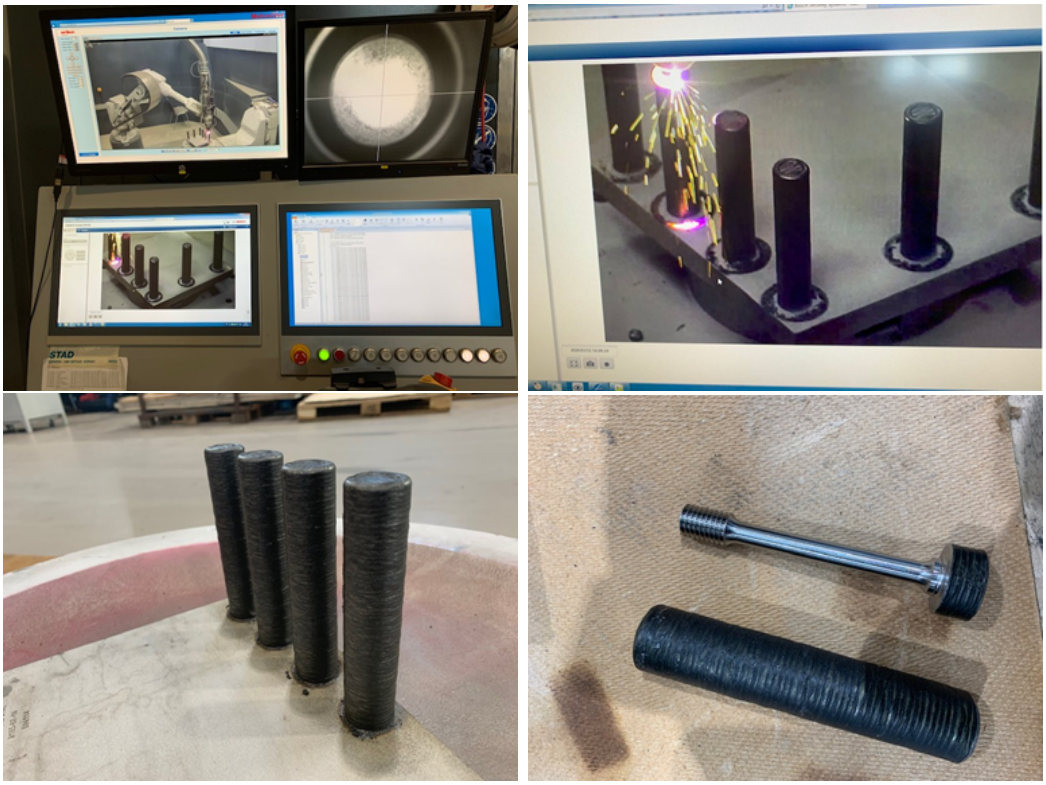

Figure 21: DED process set-up of specimens for tensile testing

The tensile test specimens were additive manufactured vertically and were initially printed as rods are with two outside parameters. The infill was done with 90 degree rotation between each layer, approximately similar to the process shown on Figure 20. The rods were later machined to form the tensile test specimens with threaded M12 (12 mm diameter) grip sections. Grip screws were manufactured at UiS labs and connected with the threaded ends of the tensile bar for extending the grip section to avoid slipping of the bar during tensile testing. Figure 22 shows the tensile bar drawing and table 8 describes the tensile test bar dimensions.

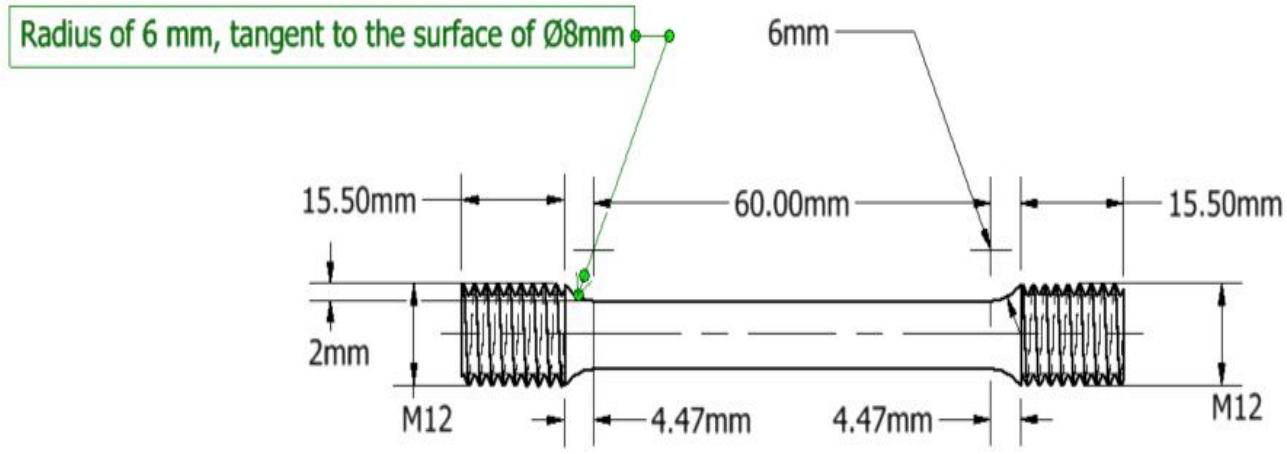

Figure 22: Auto-cad Inventor drawing of the tensile specimen bar.

Table 9: Description of the tensile test bar dimension.

Dimension	mm
Overall length	99.94
Reduced section	60
Diameter of reduced section	8
Distance between shoulders	68.94
Grip section	15.50
Diameter of grip section	12
Tangent to the reduced section	6

3.3 Heat Treatment

A High temperature furnace Nabertherm HTCT 01-14 with a P310 controller (display) was used for heat treatment of the specimens for different time intervals. Parts of flat specimen were cut to 15x10x14(length x bredth x hight) mm to examine the YZ-section and 15x3x14 mm to examine the XZ-section for each time interval. The flat bar specimens were heat treated at 1175°C for 30-,60-, 120- and 300 minutes and rapidly quenched in water. The tensile test specimens were heat treated at 1175°C for 30- and 300 minutes and rapidly quenched in water. To obtain a nearly precise heat treating temperature, the oven was set to 1125°C in order to obtain a temperature of 1175°C within the oven. Equation (8) is used to calculated the in-put temperature.

$$T(Oven) = (0.0001 * TC^2) + (0.84 * TC) + 0.38 \tag{8}$$

where, TC = Desired temperature or output temperature, T(Oven) = Input temperature.

3.4 Sample Preparation

In order to investigate the material's micro-structure under the OM and electron microscopes the specimens are prepared in following steps.

- Flat bar specimens with 10x13x14 mm and 3x13x14 mm were cut and prepare to investigate the YZ-, and XZ-sections respectively.
- Flat bar specimens with 20x20x4 mm were cut and prepared to examine the top, middle and the bottom surfaces.
- Several try and error procedures were used to successfully etch the surfaces in order to examine the grain structure by obtaining good images for OM and SEM microscopes.

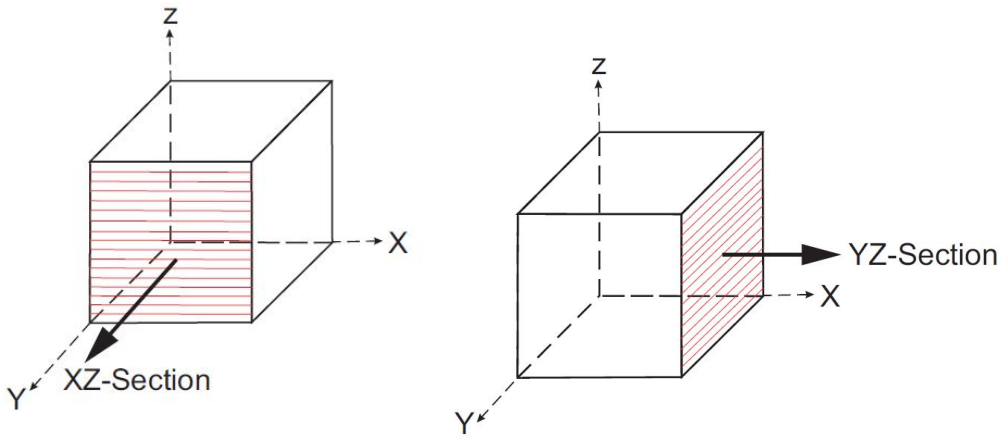

(a) XZ-section (b) YZ-section

Figure 23: Specimen preparation of the sections

3.4.1 Cutting

The specimens were cut using Struers Discotom-10 and Accutom-2 machines. Discotom-10 have fast process with a 2mm thick cut-off wheel and is suitable for cutting large parts. Accutom-2 is a very slow process with a 1 mm thick cut-off wheel which suitable for cutting thin specimens with less material waste, this method was used for preparation of XRD specimens. The dimensions for the specimen preparation were chosen in order to have a good representation of the selected surface. The heat treatment of the flat bar specimen initiated after the cutting process.

3.4.2 Hot Mounting

Hot mounting process is applied in order to easily handle the specimens while performing several procedures such as grinding, polishing, OM analysis, SEM analysis and hardness testing for metallurgical study. For high preparation quality, CitoPress-30 machine was used to mount the specimens. In this experiment, the Clarofast and Condofast hot mounting resins (powder) were used. Condofast is an expensive resin that enables the mount to be electrical conductive, which can be useful for SEM applications. Obtaining similar mount dimension with good thickness helps handling the specimens better. For the XZ-section (thin specimens), a messing cylinder was used as a support and was mounted together to improve conductivity. After all the specimens are hot mounted, the specimens are placed and screwed tight to the mount holders that are used by the Sturers Pedamax-2 and TegraForce-5 machines. Table 10 and Table 11 describes the amount of resin used for each section in ml.

Table 10: Amount of XZ-section's mounting resins applied.

XZ-Section's mounting resins	Volume (ml)
Clarofast	7.39
Condofast	7.85
Total	15.24

Table 11: Amount of YZ-section's mounting resins applied.

YZ-Section's mounting resin	Volume (ml)
Clarofast	12.5
Condofast	2.85
Total	15.35

3.4.3 Grinding and Polishing

Grinding and polishing processes are essential for surface preparation of the specimen for microscopic examination. This process is carefully performed because a single contamination of tiny particle on the grinding process could create scratches on the surface of the specimen which is undesirable. The goal is to have a scratch free, clear and reflective surface.

SiC papers with grit sizes P120, P220, P500, P1000, P1200, P2000 P2400 and P4000 were used respectively for 5 - 15 minutes at each step. After each step the specimen holder was cleaned with water. After the grinding process was finished the specimens were polished using polishing pads with 9-, 3-, 1μm diamond suspensions for 3-5 minutes respectively. After each step, distilled water was used to clean the specimens because the impurities and minerals could contaminate the specimen's surface. A 0.04 μm OP-S suspension was applied for 10 minutes as the final polishing step. These specimens were suitable for SEM but not for OM. In order to visualize the grain structures in OM the specimens were grinded and polished again using the similar procedure but instead of OP-S, electro-polishing and etching were used as the final step.

3.4.4 Electrolytic polishing and Etching

To expose the micro-structure of the specimens electrolytic polishing and etching were applied. The as-built specimens with high residual stresses were electrolytic polished with A2 electrolyte applying 30V for 10s and revealing the micro-structure of the surface. The chemical reaction of A2 solution was very strong on the heat treated specimens and nothing could be seen on the optical microscope. The heat treated specimens were re-polished and etched with a 35% HCL solution for three minutes. A small amount of hydrogen peroxide (H_2O_2) were added to the 35% HCL solution in order to increase the concentration and to obtain the desired reaction. The specimens are further examined under the OM for structural examination using Olympus GX53 inverted microscope.

3.5 Sample preparation for SEM

The conductive mount on the specimen made it possible to directly use the specimen for SEM. The specimen was cleaned with distilled water and an ultrasonic bath to remove any contaminations. A conductive double-sided carbon tape was used to attach the specimen to the pin stub specimen mounts. The pin is then mounted to the platform and inserted to the SEM machine. The working distance (WD) used was between 10 - 12 mm, the accelerating voltage applied was 20kV and an aperture size of 60 µm for the QBSD signal. Figure 24 shows the the specimen with the SEM machine.

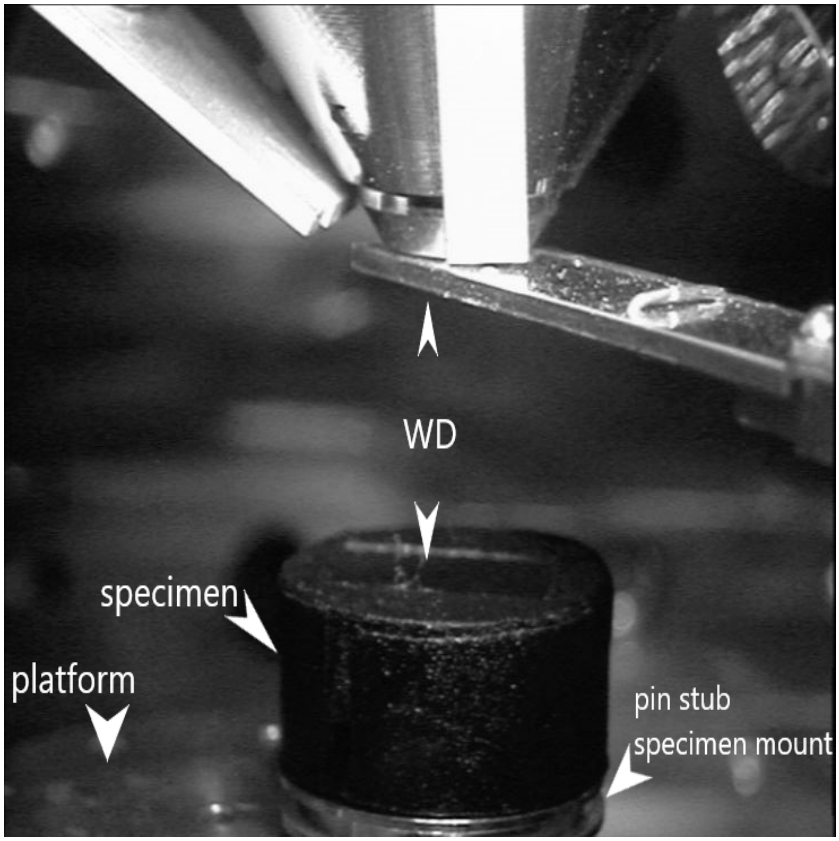

Figure 24: A mounted specimen inside a SEM machine.

3.6 Sample preparation for TEM

TEM was used to observe the dislocations and precipitated phases. Specimen preparation for TEM is a complicated and time consuming process, several steps involve in specimen preparation. There are several techniques that are generally applied to polish TEM specimen, in this experiment the Jet polishing technique was applied.

Initially a 1 mm thick specimen was cut using Accutom-2, several grinding grit size steps of 80P, 120P, 320P, 500P and 1000P were applied on both sides of the specimen. The TEM specimen is preferred to be 0.1mm thick before applying the jet polishing process. The Jet polishing process created a cicle in the middle of the specimen with a nanometer (nm) thickness on the edge of the circle, this nm thick section is used for TEM analysis.

3.7 Sample preparation for XRD

Specimens for XRD were cut using Accutom-2 machine into a rectangular shapes with 2 cm on each side and a 4mm thickness. The specimens were labeled and mounted for grinding and polishing. The specimens were finished using UP-S giving a clear reflecting surface with no scratches. The specimens were initially used for SEM, the mounts were then removed for XRD. Figure 25 shows the image of the machine (D8 Advance Eco) used for XRD measurements.

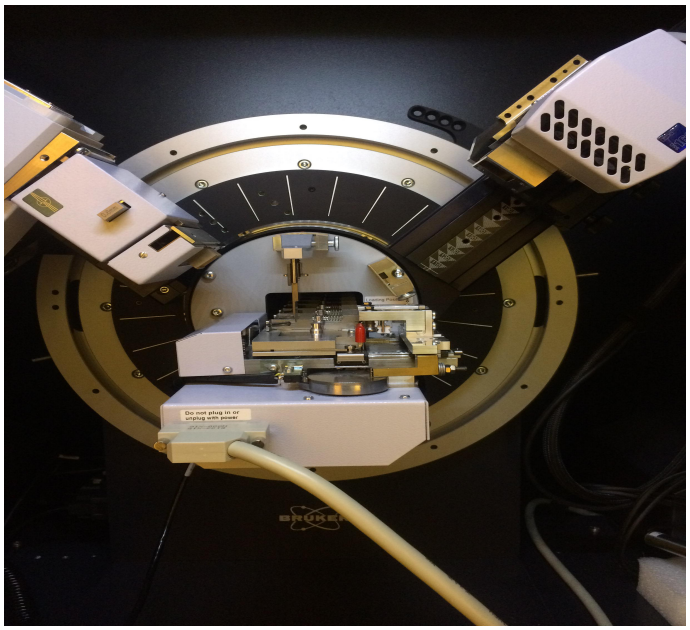

Figure 25: A mounted specimen inside a XRD machine.

3.8 Hardness test

The Vickers hardness method was used to examine the difference in hardness due to stress relief heat treatment. During a materials service life, there is a possibility of a physical impact that can cause deformation. Hardness test is a good method to evaluate how the material can resist this plastic deformation. In order to have a valid measurements, the specimen surface was made even and free from factors than can influence the test results. Struers DuraScan machine was used to perform the indents at room temperature. A 5 kg kilogram indention load (HV5) was applied on the specimen surface. A distance of 1 mm from the edge and 1-2 mm between the indent centers was applied. Figure 26 shows the indentation patterns perfomed on the XZ- and YZ-Sections. Figure 27 shows the indentation patterns performed on XRD specimens.

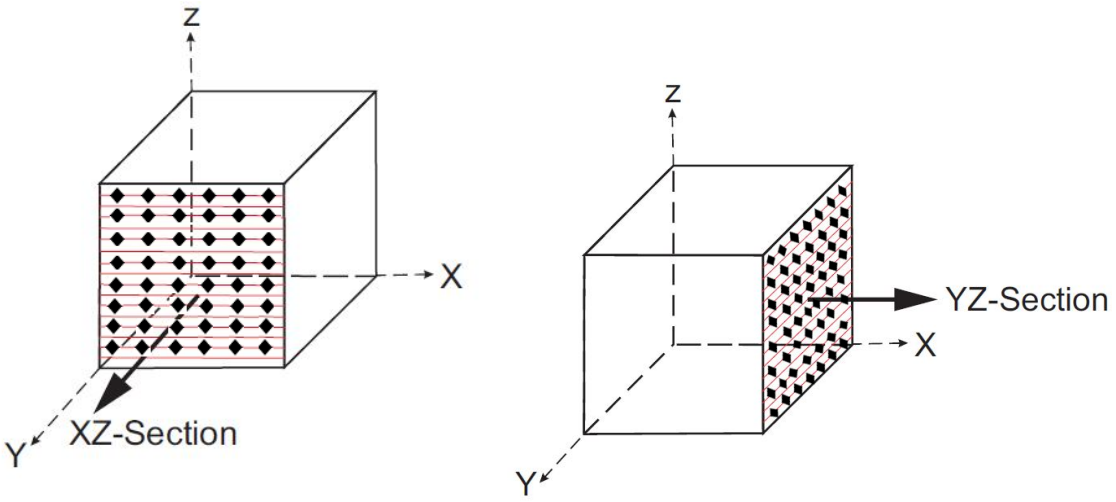

(a) Indents on XZ-Section (b) Indents on YZ-Section

Figure 26: Indentation pattern of the sections

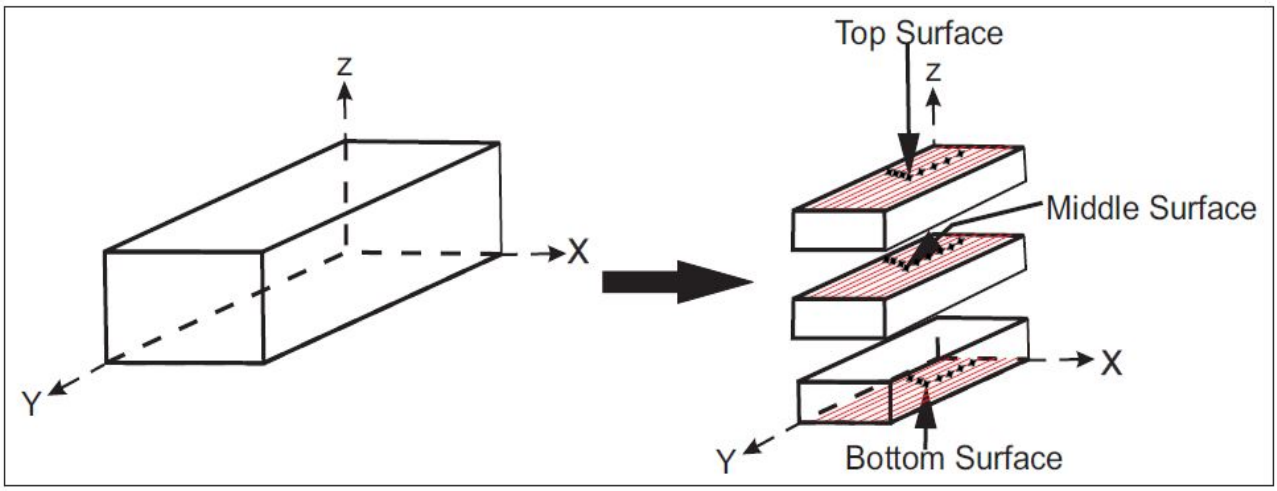

Figure 27: Auto-cad Inventor drawing of the tensile specimen bar.

3.9 Tensile test

The tensile test was applied to examine the mechanical behaviour of the material under uniaxial load. During the materials service life, the material can be exposed to several loads, this tests will investigate the effect of the applied load on the material. Two pairs of tensile test specimens were used to validate the test results. Instron tensile machine was used according to ISO 6892-1:2009 standards to perform this test. Two strain rates has been applied, strain rate 0.00025mm/s for the elastic region and a strain rate of 0.00670 mm/s for the plastic region. All tensile tests have been conducted up to point of fracture or failure.

4 Results

The results from experiments performed with the AM Inconel 625 manufactured by DED are presented in this chapter. Results such as hardness measurements, tensile strength, EDS analysis, XRD analysis, SEM and TEM are included. Hardness results of specimens with different heat treatment time that obtained approximately similar values were excluded. For example hardness values for the specimen heat treated for 60 and 120 minutes are not included, since there was small change in hardness after 30 minutes. Only the results that showed significant change in mechanical and micro-structural properties are presented and compared. Relevant images, graphs and tables that were not included in this part are presented in the Appendix. Results of the experiments performed are given below:

4.1 Mechanical properties

4.1.1 Hardness results

Hardness was tested both before and after heat treatment at 1175°C for different time periods. Readings of average hardness (HV5) values for the YZ-section are taken from top to bottom and left to right as shown in Figure 28.

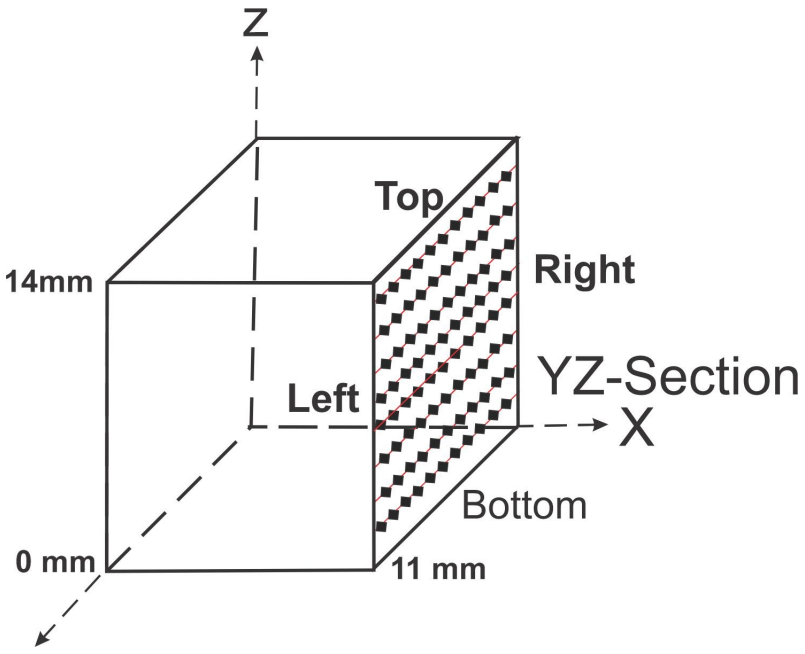

Figure 28: Average values taken from left to right and top to bottom.

Figure 29 shows the HV5 indentations on the YZ-section and measured hardness values. Red numbers are the average HV5 values of vertical columns while blue numbers are the average HV5 values of the horizontal rows. The build direction (BD) is along the Z-axis as shown in Figure 29(a).

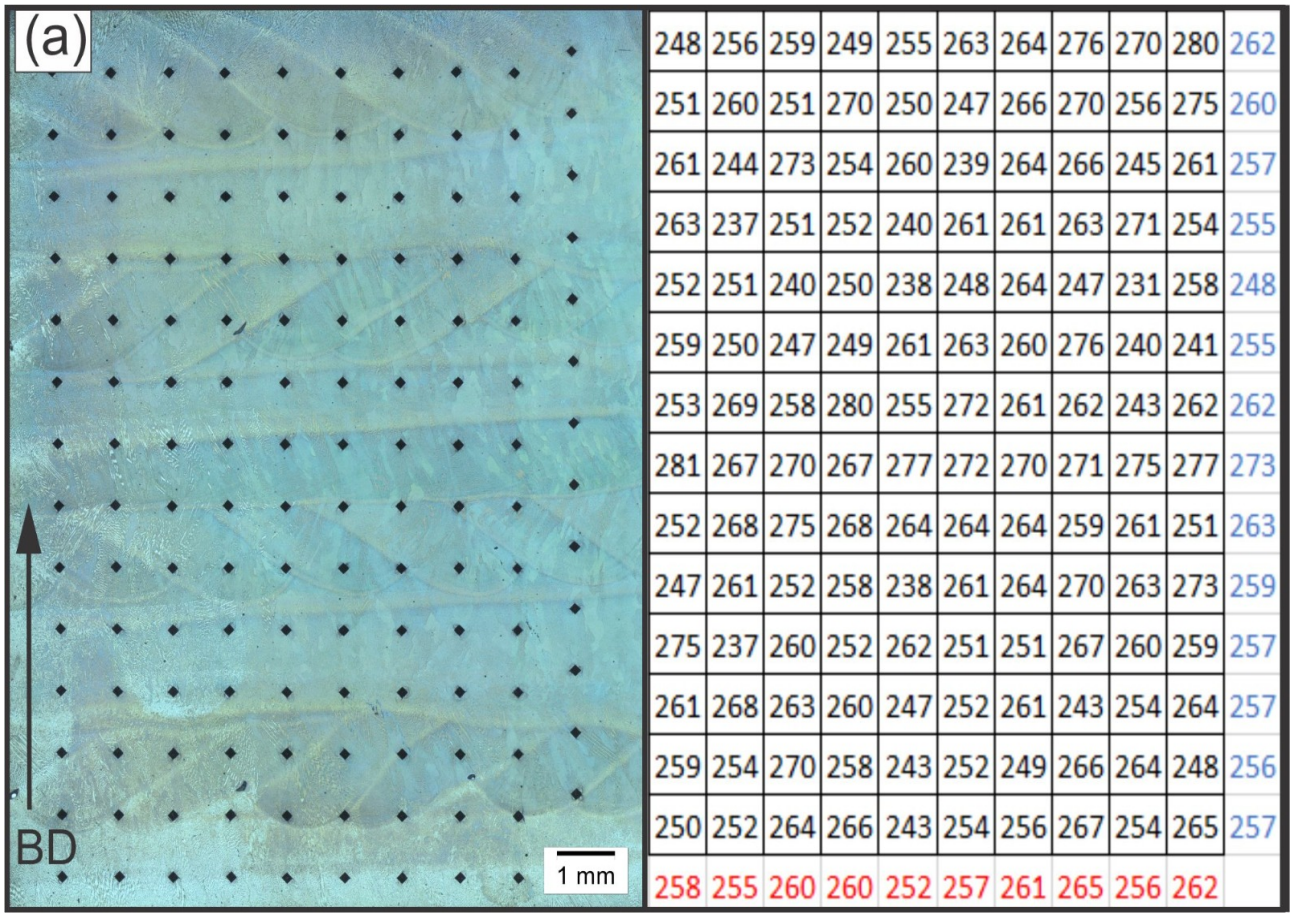

248	256	259	249	255	263	264	276	270	280	262
251	260	251	270	250	247	266	270	256	275	260
261	244	273	254	260	239	264	266	245	261	257
263	237	251	252	240	261	261	263	271	254	255
252	251	240	250	238	248	264	247	231	258	248
259	250	247	249	261	263	260	276	240	241	255
253	269	258	280	255	272	261	262	243	262	262
281	267	270	267	277	272	270	271	275	277	273
252	268	275	268	264	264	264	259	261	251	263
247	261	252	258	238	261	264	270	263	273	259
275	237	260	252	262	251	251	267	260	259	257
261	268	263	260	247	252	261	243	254	264	257
259	254	270	258	243	252	249	266	264	248	256
250	252	264	266	243	254	256	267	254	265	257
258	255	260	260	252	257	261	265	256	262	

Figure 29: Image illustrating the HV5 indentations of the as-build specimen (YZ-section) and it's values: a. YZ-section, the black spots are hardness HV5 indents taken. Right image: Hardness measurement values from each indent of the YZ-section.

Table 11 shows the average hardness measurements, standard deviation and the confidence interval values of all (HV5) indents taken in the YZ-section after different heat treatment time periods. The confidence interval is 95%, which is a reliable number. Average hardness value decreases on heat treatment, which can be observed from the values in Table 11.

Table 12: Average, standard deviation and confidence interval of hardness measurements, YZ-section.

Heat treatment time (min)	0	30	300
Average ± SD	257.70 ± 10.23	219.40 ± 11.06	218.60 ± 10.15
Confidence Interval (95%)	[255.99, 259.41]	[217.55, 221.25]	[217.70, 221.01]

Figure 30 illustrates the trend of the average values of all hardness (HV5) measurements taken at different heat treatment time periods. The AM Inconel 625 showed reduction in the average hardness value by approximately 40HV on heat treatment for 300 minutes at 1175°C (Figure 30). Average hardness value decreased from 257.70HV to 219.40HV in first 30 minutes of heat treatment, which can be observed by a sharp drop in hardness in Figure 30. The specimen heat treated for 300 minutes showed very less decrease in average hardness compared to decrease after 30 minutes i.e. hardly 3- to 4HV decrease from 30 minutes to 300 minutes of heat treatment.

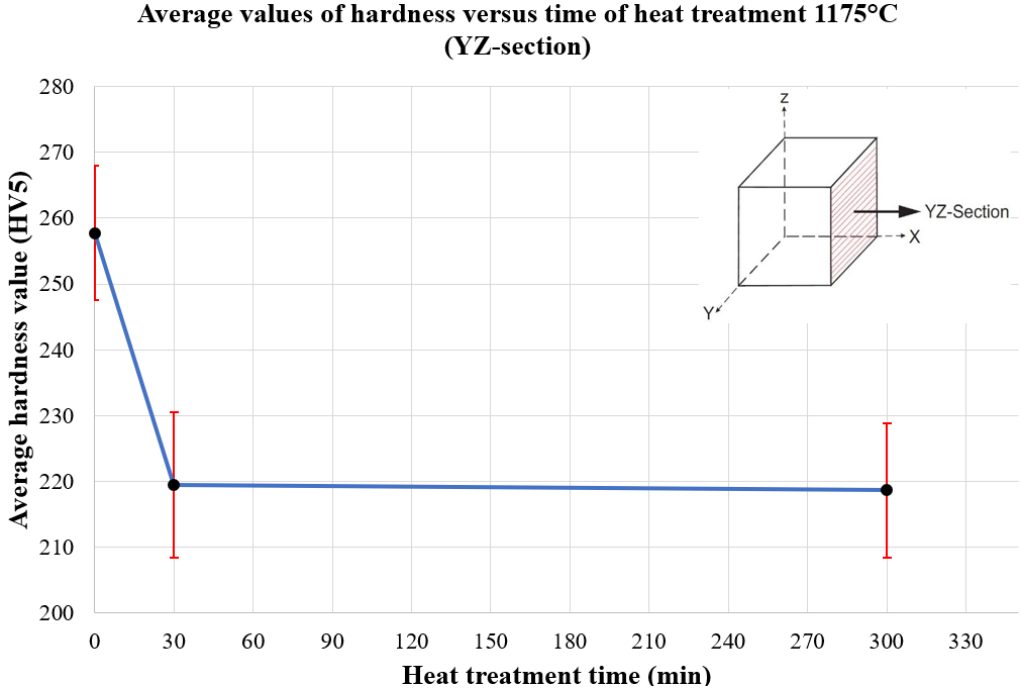

Figure 30: Average hardness values versus heat treatment time periods.

Figure 31 (b) shows average hardness values measured from top to bottom, average values of hardness fall between 256HV to 273HV. Hardness differ from top to bottom, it decrease than increase and than decreases again. High values of the hardness are recorded in the middle of the specimen (marked by red arrow in Figure 31(a)). Layer with the lowest readings of hardness is marked with blue arrow.

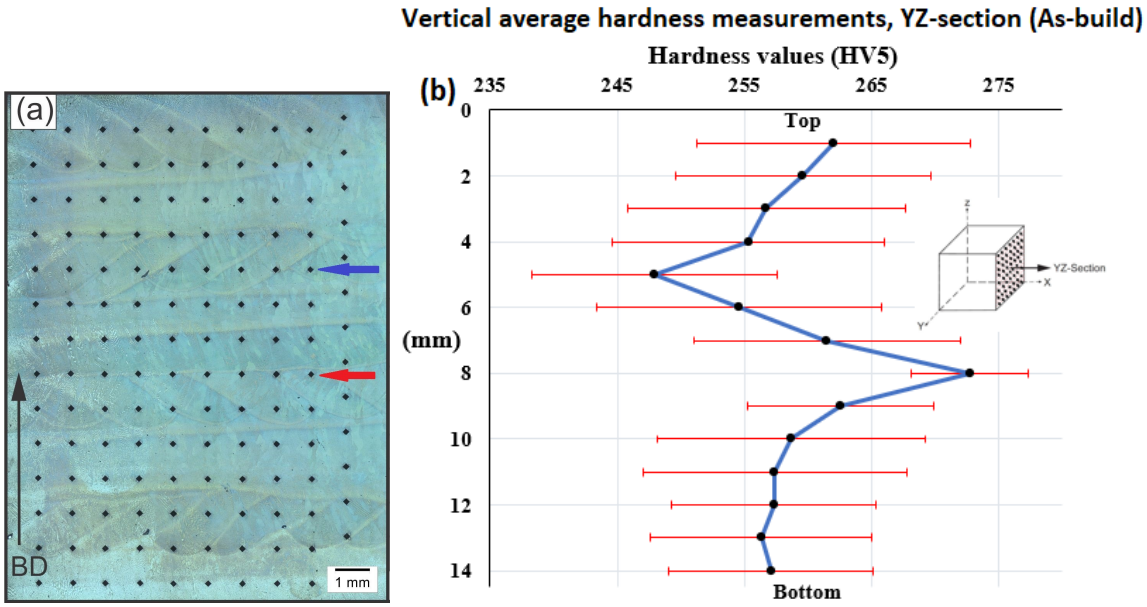

Figure 31: (a). Optical microscope image of YZ-section showing indentation points on YZ-section, red arrow marks the layer with highest hardness values. blue arrow marks the layer with lowest hardness values. (b). Distribution of hardness values with standard deviation from top to bottom. Y-axis shows the measurement distance from the top edge. X-axis show average hardness value of each row.

Similarly, Figure 32 shows average hardness values measured from left to right at YZ-section of as-built specimen. It can be observed that most of the indented average hardness (HV5) values fall between 252HV and 265HV. Values of hardness show a trend of increase and decrease along the specimen. Blue lines in the figures show hardness value distribution. Red lines in the figure show the standard deviation.

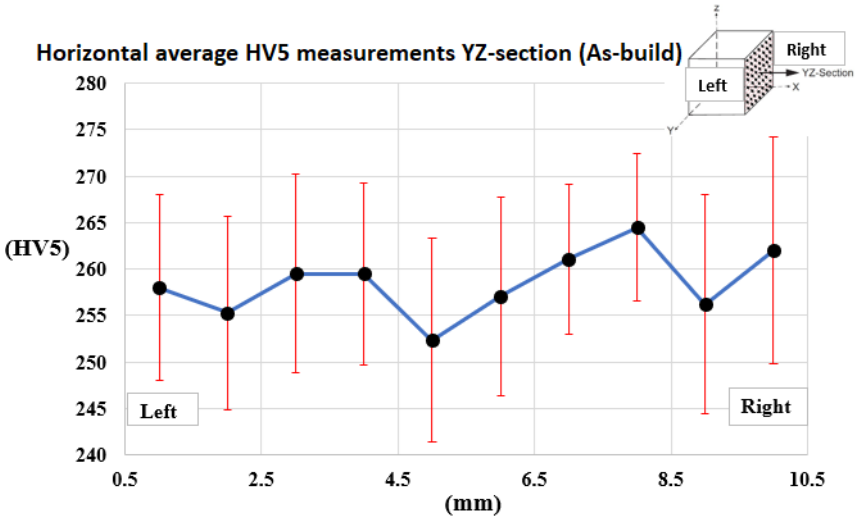

Figure 32: Distribution of average hardness values with standard deviation from left to right. X-axis shows the distance from the left side of the specimen. Y-axis show average of hardness (HV5) for each column.

Hardness values for YZ-section of a 30 minute heat treated (HT-30min) specimen show a trend of increase in hardness from top to bottom that can be seen in figure 33. It can be observed that hardness of overall specimen is decreased compared to as-build specimen.

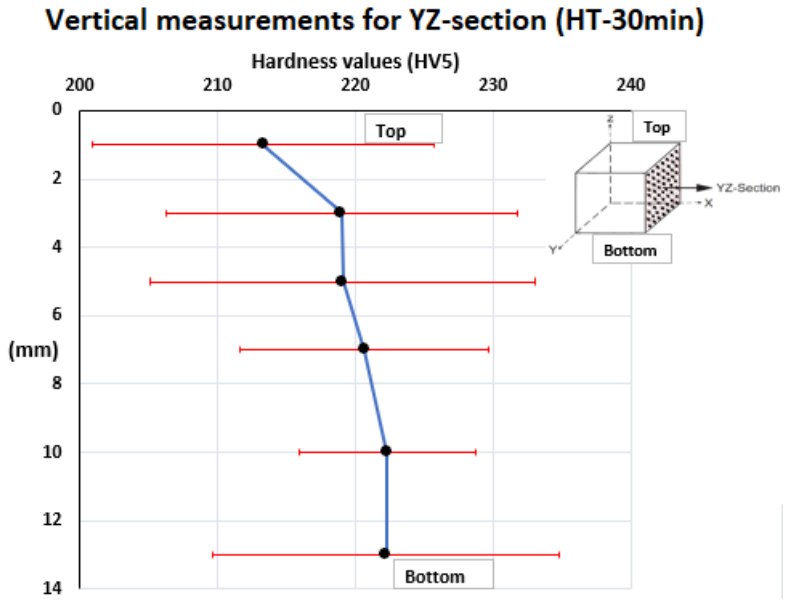

Figure 33: Distribution of average hardness values with standard deviation from top to bottom. X-axis shows the average hardness measurement from top to bottom. Y-axis show distance from the top edge of the specimen.

Average hardness value of the heat treated (HT-30 min) specimen from left to right is illustrated in Figure 34. The trend line shows that the average hardness readings are in an increasing and decreasing pattern but most of the reading are lying within the standard deviation. Low hardness values on the right side of the specimen is due to cracks on the right side that are shown in section 4.3.

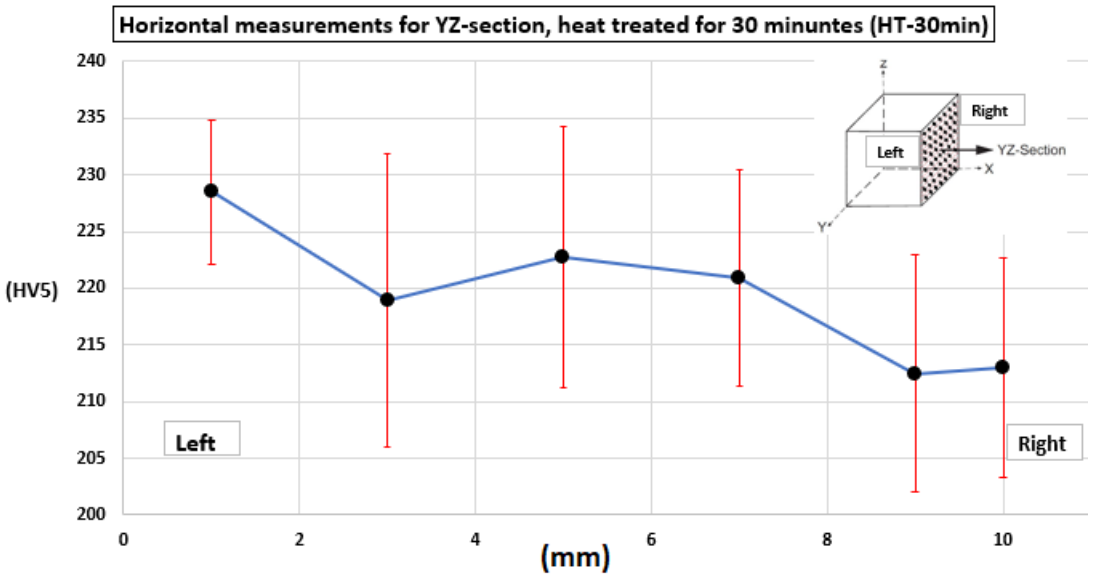

Figure 34: Distribution of hardness values with standard deviation from left to right. X-axis shows the measurement points from left to right. Y-axis show the average hardness values.

Average hardness readings measured of the XY-section at different surfaces (top-, middle- and bottom surface) are shown in Table 12. It can be observed that average hardness decrease in the build direction (BD) i.e. from bottom to top. Figure 35 shows the trend of decrease in hardness from bottom to top. There is more decrease in hardness from bottom to middle surface as compare to middle to top surface.

Table 13: Average hardness measurements top, middel and bottom surface.

As-build	HV5	Confidence Interval (95%)
Top surface	257.65 ± 9.69	[253.12, 262.19]
Middle surface	262.67 ± 10.15	[260.38, 264.96]
Bottom surface	281.00 ± 9.20	[278.93, 283.07]

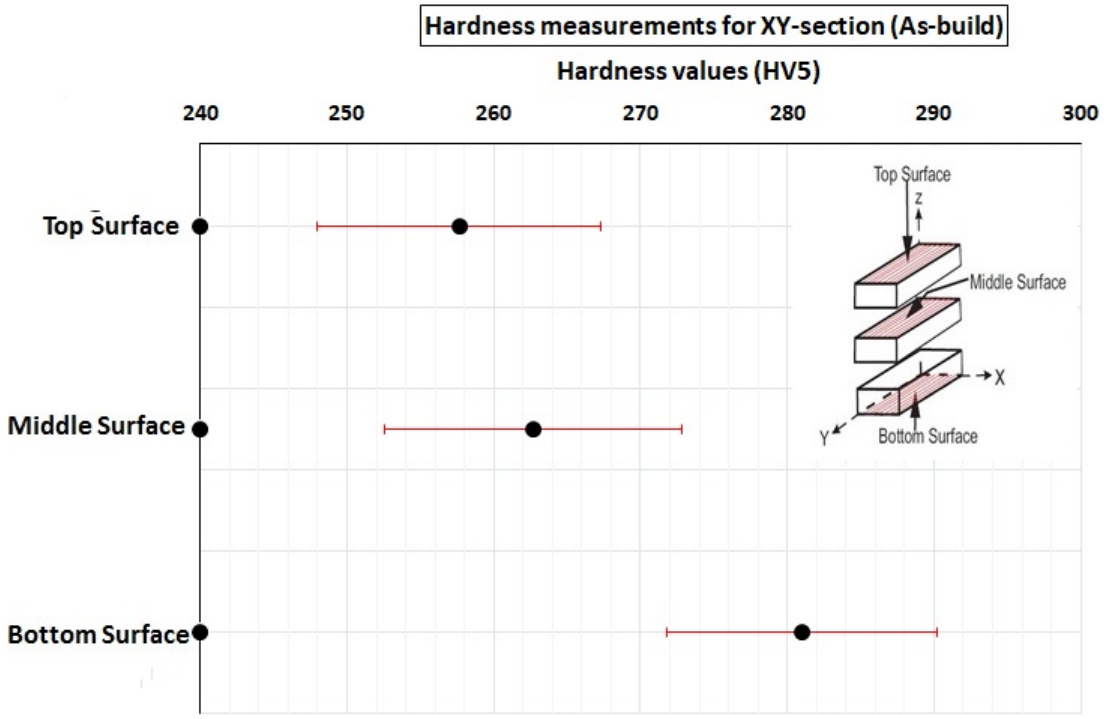

Figure 35: Average hardness readings measured at top, middle and bottom surface. Red lines show standard deviation. Schematic diagram of surfaces used for measurement of readings is shown in the top right corner.

4.1.2 Tensile test

Tensile tests are carried out on both as-build and heat treated specimens. All the tensile tests specimens were strained until fracture. The fractures occurred within the gauge length section for all the tests. Strain curves from the tests of six specimens are shown in Figure 35.

The tensile test results of each pair of as-build and heat treated specimens seems to be inconsistent (see table 13).Tensile strain curve followed the same path for both as-build specimen pairs until fracture. The ultimate tensile strength's (UTS) difference between the two as-build specimen pairs is approximately 42 MPa. However, as-build specimen-2 shows a similar yield strength value but a significantly lower tensile strain (15% difference) as compared to as-build specimen-1. For all heat treated specimens, tensile strain curve also followed the same path until fracture. UTS values of all the heat treated specimen pairs are also compared with each other and with the as-build specimens. The average UTS values for 30- and 300 minute heat treated specimens were approximately similar (see Figure 36) but the difference of the average E-modulus, yield strength and percentage of elongation values are 3.8GPa, 11MPa and 5.25% respectively (see table 13). The difference between the average UTS values of the as-built

and heat treated specimens is approximately 20MPa. Increase in heat treatment time resulted in increase of percentage of elongation and a reduction in tensile strength. Table 13 shows the tensile test results of as-build and heat treated specimens obtained from the experimental procedure.

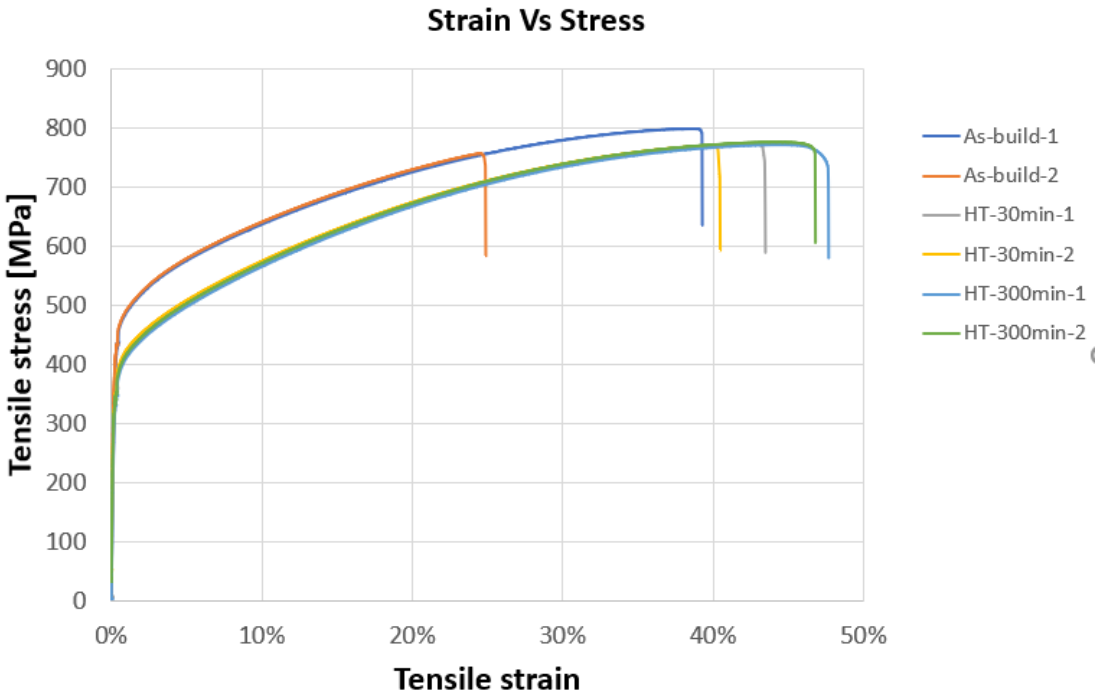

Figure 36: Strain curves description: As-build-1= As-build specimen, number 1, As-build-2= As-build specimen, number 2, HT-30min-1= heat treated for 30 minutes specimen number 1, HT-30min-2= heat treated for 30 minutes specimen number 2, HT-300min-1= heat treated for 300 minutes specimen number 1, HT-300min-2= heat treated for 300 minutes specimen number 2.

Table 14: Tensile test results.

Specimen	E-modulus [GPa]	UTS [MPa]	Yield strength [MPa]	Elongation [%]
As-build-1	161.0	798	437	39.3
As-build-2	163.4	748	435	24.9
HT-30min-1	163.3	754	360	43.5
HT-30min-2	184.5	759	363	40.5
HT-300min-1	174.8	737	348	47.7
HT-300min-2	192.6	763	353	46.8

The pattern show that with increasing heat treatment the tensile strain also increase at constant rate. All heat treated specimen showed more elongation (tensile strain) compared to as-build specimens. The as-build specimens had approximately similar E-modulus, UTS and yield strength values but a difference of more than 10% in percentage of elongation. For 30 minute heat treated specimens E-modulus value had more than 20GPa difference. For 300 minute heat treated specimens the E-modulus and the UTS had a difference of more than 17GPa and 26MPa respectively.

No necking is observed in the specimen during the test, that confirms the behaviour of Inconel 625 super alloy mentioned in literature. There was a significant and sudden fracture in the specimen as shown in Figure 37.

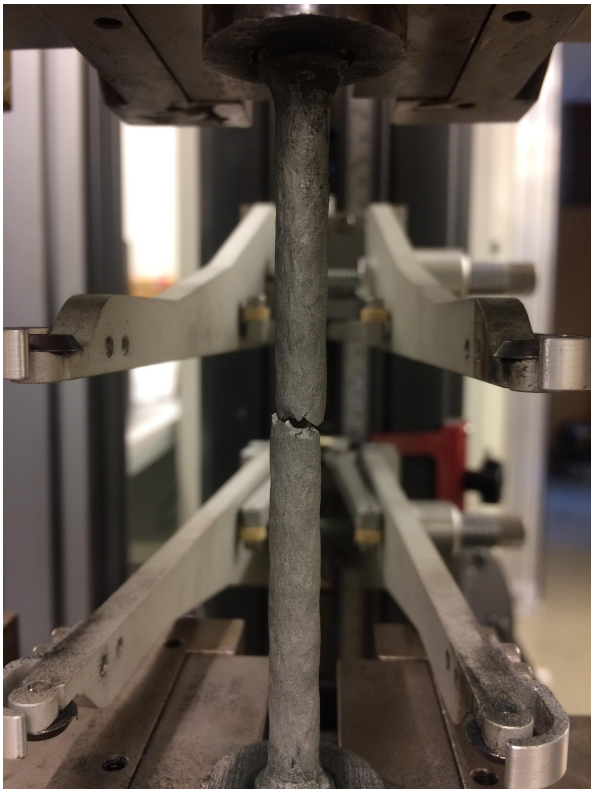

Figure 37: Fractured specimen due to tensile strain.

4.2 XRD

The micro-strain values and the grain size are calculated using the Williamson-Hall approach. The estimated grain size is 100μm. Figure 38 illustrates the XRD diffractogram, the intensity peaks versus 2-theta recorded.

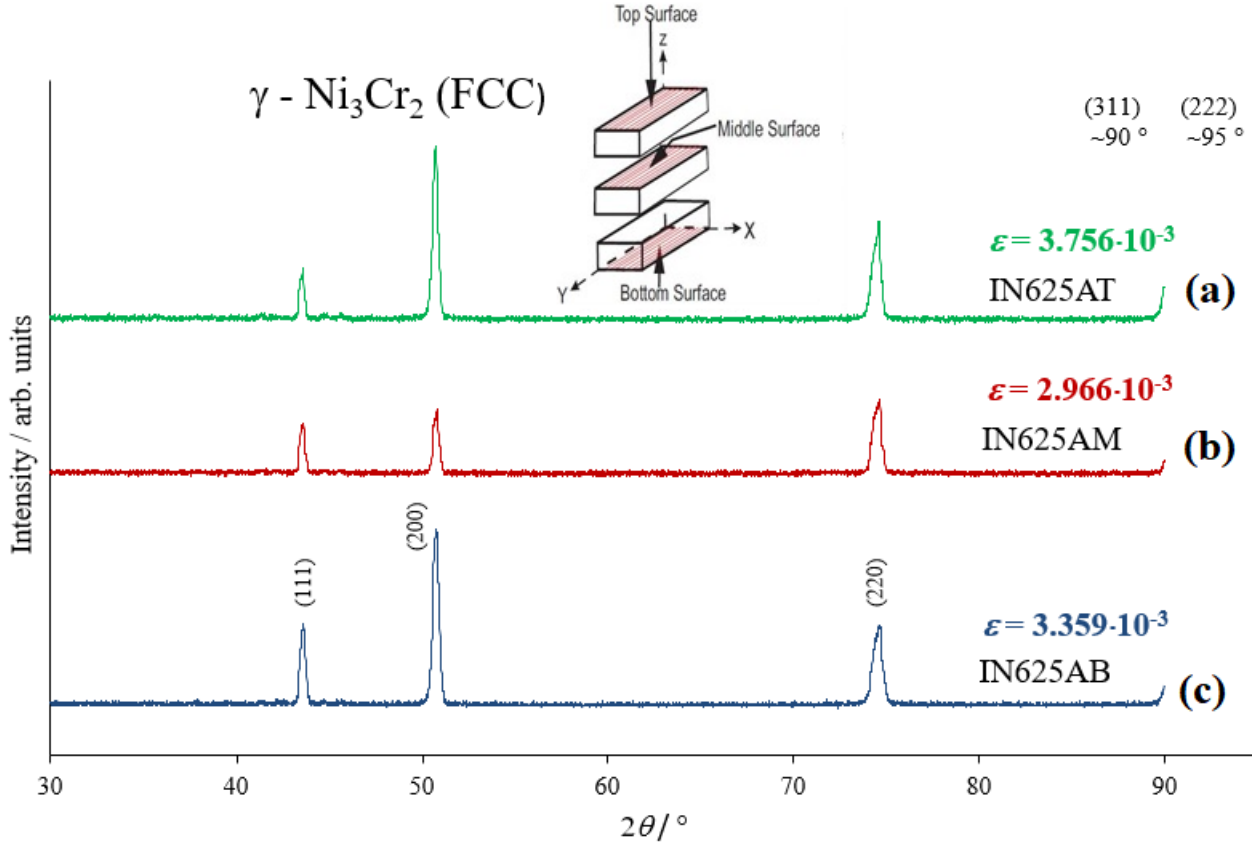

Figure 38: XRD diffractogram of AM Inconel 625, top-, middel- and bottom surface for as-build specimen: (a).As-build top surface. (b). As-build middle surface. (c).As-build bottom surface.

Figure 39 shows the β cosθ versus sinθ scatter plot, the three blue points are the calculated value (β cosθ and sinθ) from the XRD data. The linear fitting was done to find the slope and the intercept in order to calculate the strain value using the Williamson-Hall approach. The R-squared "R^2 = 0.989700" data data obtained from the as-build specimen shows how the reliability of the model (98%). Table 15 shows the micro-strain values, where the top and the bottom results have approximately similar value, but the middle surface have a smaller strain value.

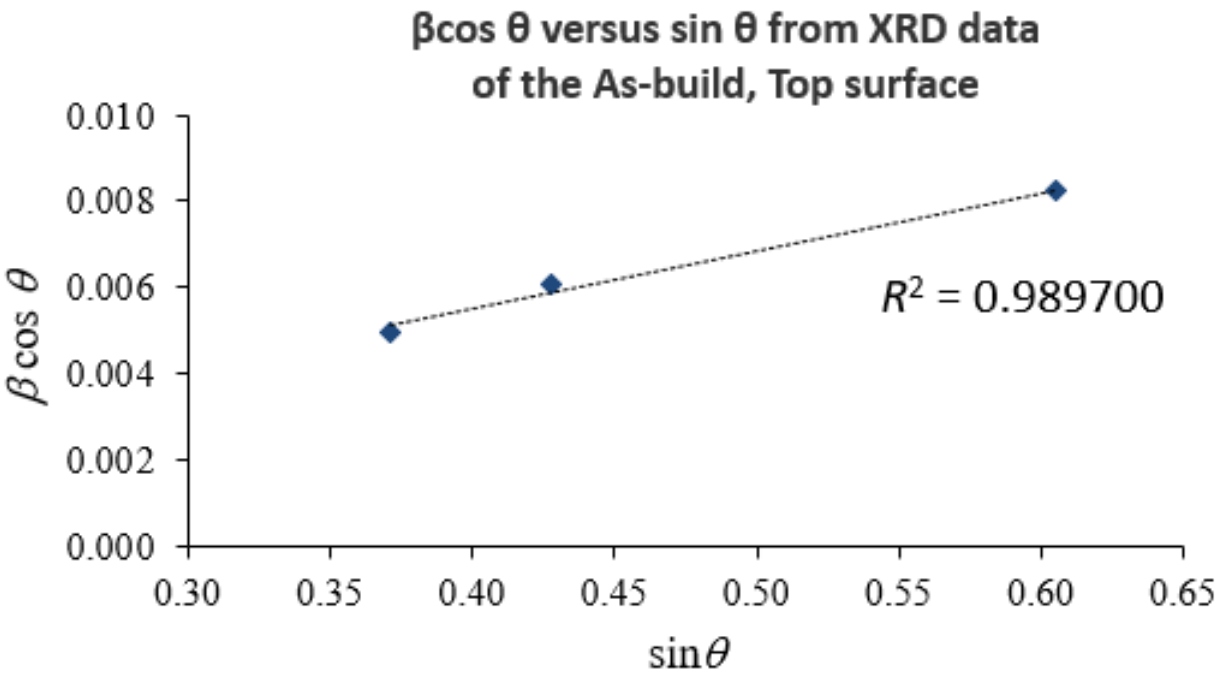

Figure 39: β cos θ versus sin θ.

Table 15: Micro-strain values of as-build specimen (XY-section); (a).top surface. (b).middle surface. (c).bottom surface.

Surface	Strain (ϵ) of As-build specimen
(a)	$3.359 \cdot 10^{-3}$
(b)	$2.966 \cdot 10^{-3}$
(c)	$3.756 \cdot 10^{-3}$

4.3 Optical and Electron Microscopy

4.3.1 Optical Microscope

Figure 40(a) shows an optical microscope image of the XZ-section for the as-build specimen, the deposited layers, HAZ, fusion-lines and the melt pool are clearly visible. There are 8 deposited layers with approximate thickness of 2mm (Figure 40(a)). A lot of randomly scattered pores and some weld defects were observed on the specimens. Figure 40(b) shows the 30 minute heat treated specimen. All heat treated specimens obtained similar micro-structures and showed recovery of the grain structure, segregation of heavy and light elements. The weld pool, heat affected zone (HAZ) and deposition layers have disappeared due to heat treatment.

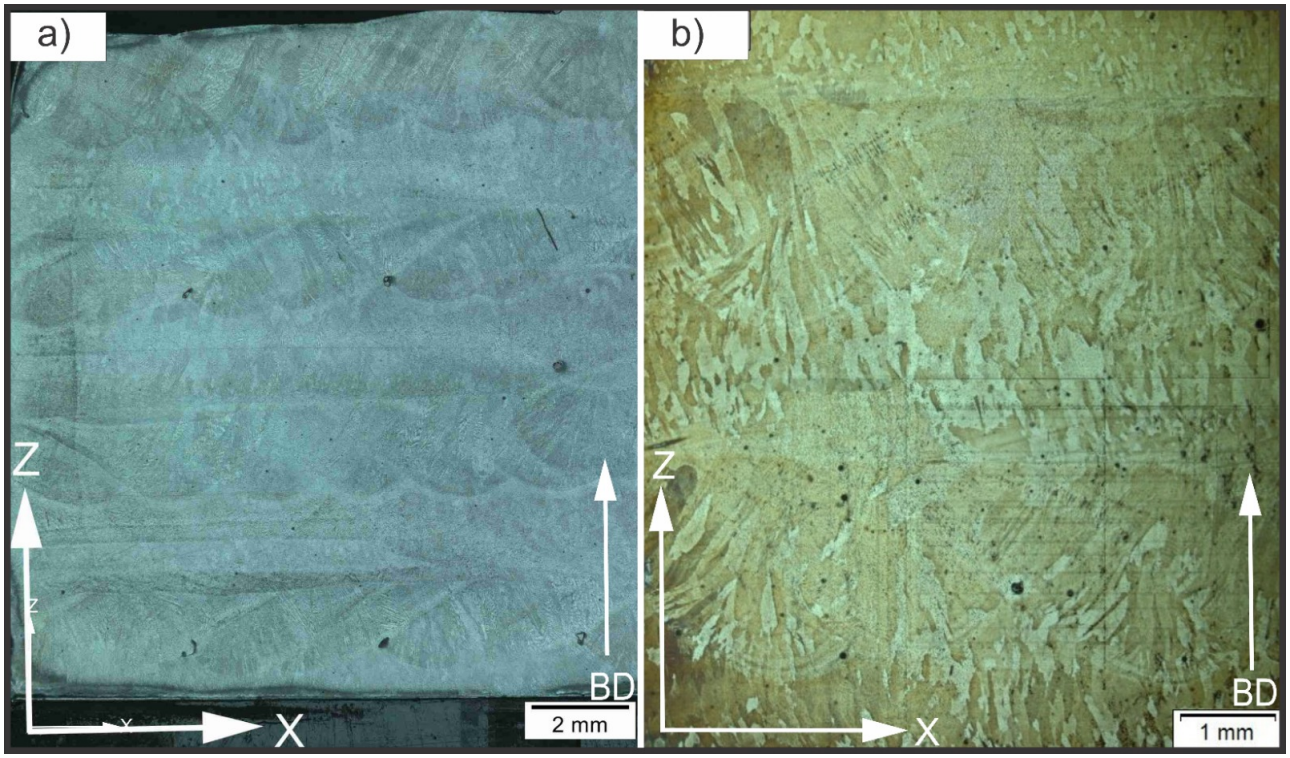

Figure 40: XZ-section panorama images: a. As-build, b. 30 minute heat treated specimen

In heat treated (30min) specimen, weld pools and HAZ can possibly exist in some parts which are observed under the microscope. These heat effected zones influence the integrity of the alloy. Heat effected zones and weld pools in heat treated specimen are shown in Figure 41. Residual stresses may also be formed in heat effected zones that may lead to high stress cracking. A layer of coarser grains is also observed (Figure 41), layers of coarser grains gives higher hardness value.

Figure 42 (a) shows the grain structures of the as-build specimen and Figure 42 (b) shows

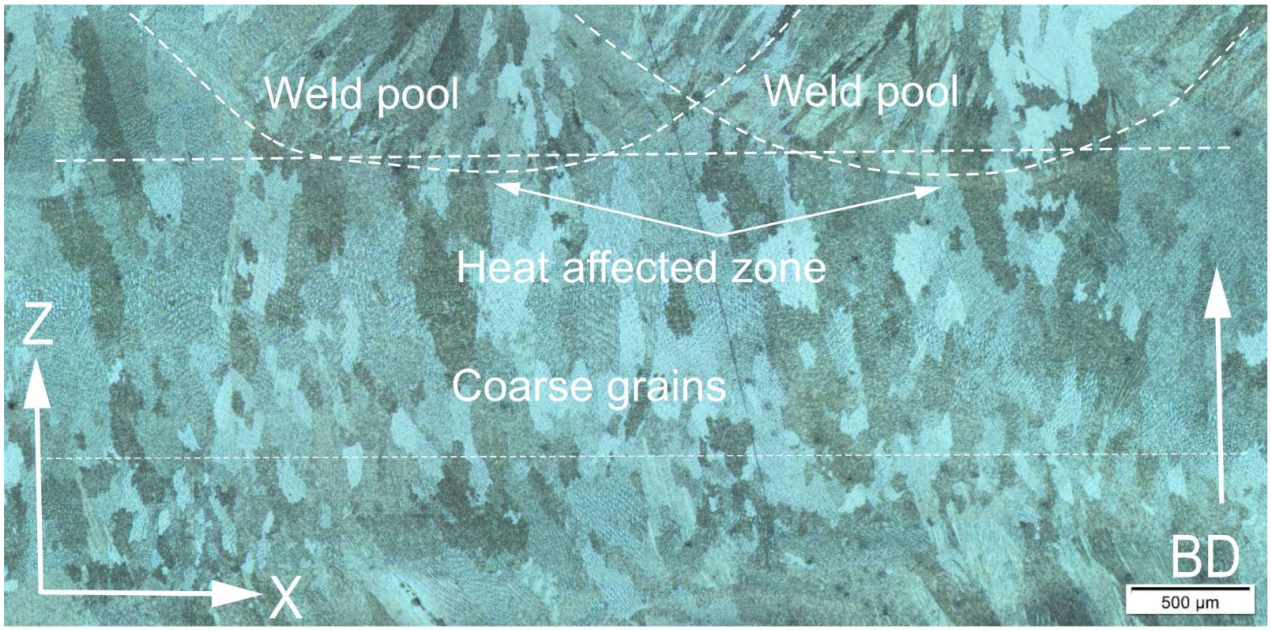

Figure 41: Micro-structure of as As-build specimen, XZ-section

grain structure of the heat treated (30 min) specimen. The heat treated (30 min) specimen undergo recovery process during heat treatment. During the recovery process the elements that were on the surface disappeared and the grain boundaries became clearly visible (see Figure 42(b)).

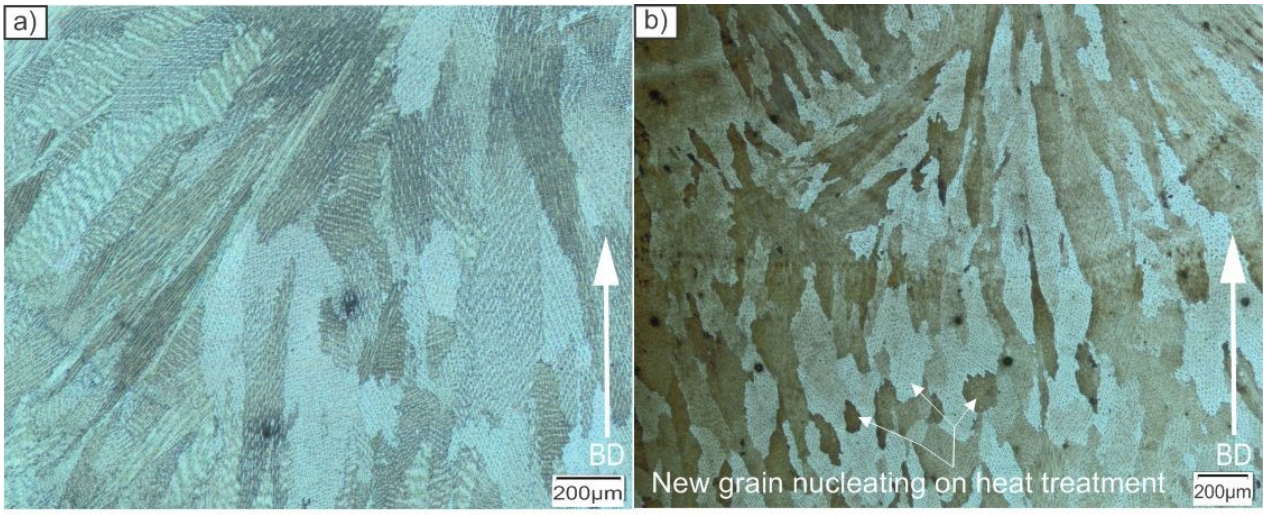

Figure 42: Micro-structure of; (a) s-build specimen (b) 30 minute heat treated specimen

Cracks and welding defects are also observed in the optical microscope. Welding defects observed are shown in figure 43. These defects and cracks also contribute to the reduction in the hardness and effect other mechanical properties of the material, such as elongation, tensile and yield strength.

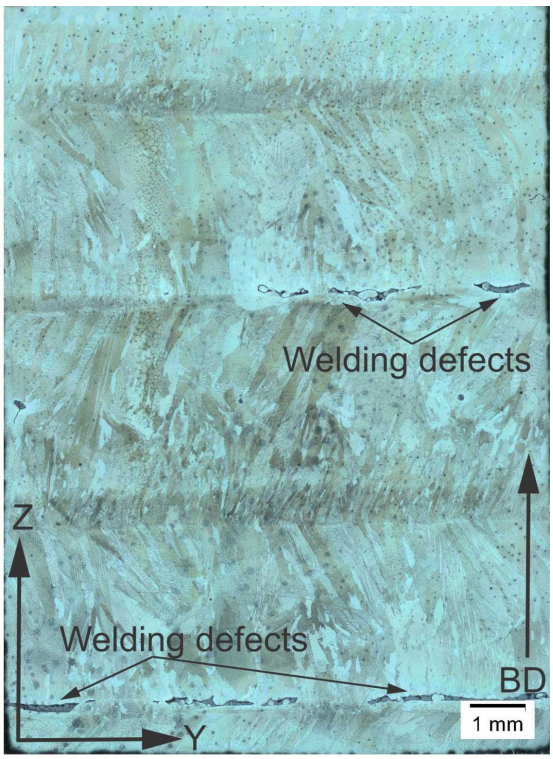

Figure 43: Welding defects of 30 min heat treated specimen, YZ-section

In Figure 44 heat effected zone can be observed at the bottom of the specimen. Micro-structures of the heat effected zone can also be seen. This is due to fast solidification of the material due to low temperature of the base material.

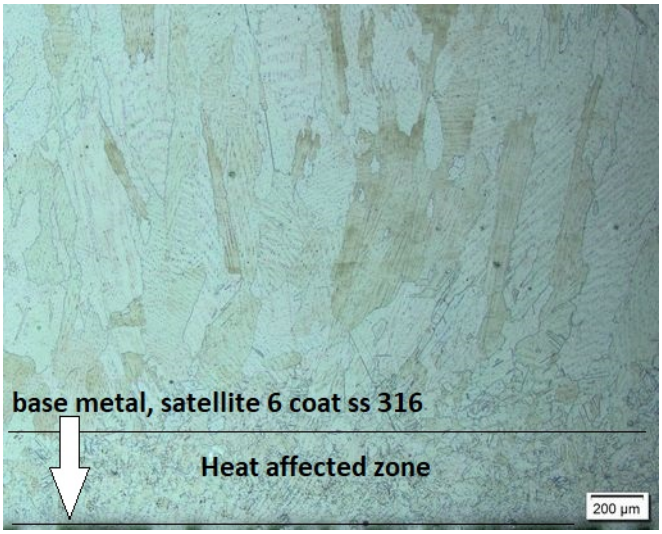

Figure 44: HAZ micro-structure and base metal of 30 min heat treated YZ-section

4.3.2 Scanning electron microscopy (SEM)

Cellular shaped structures surrounded by bright spots are observed in as-built specimen upon observation in SEM. In this section, all SEM images were taken using backscatter electron detector. A comparison of as-build and heat treated specimen is shown in Figure 45 and 46. Most of the surface area in the as-build specimen is dominated by cellular structure as shown in figure 45(a). Cellular bright structures are mostly heavy elements shown in Figure 45(a) and 46 (a). Grain boundaries became clearly visible upon heat treatment which can be seen in figure 45(b) and 46(b). After the heat treatment heavy elements (bright spots) develop circular to ellipsoidal shape with well developed boundaries Figure 46(b). Bright spots in Figure 45(b) and 46(b) are segregated heavy elements like Ni, Fe, Mo, and Nb. Table 14 shows the elemental chemical composition analysis using EDS was taken from an area of the as-build specimen.

Table 16: Elemental chemical composition analysis using EDS, taken from the as-build specimen.

Elements	C	Al	Si	Nb	Mb	Cr	Fe	Ni
Weight %	2.26	0.03	0.35	3.07	7.08	24.39	4.99	57.83

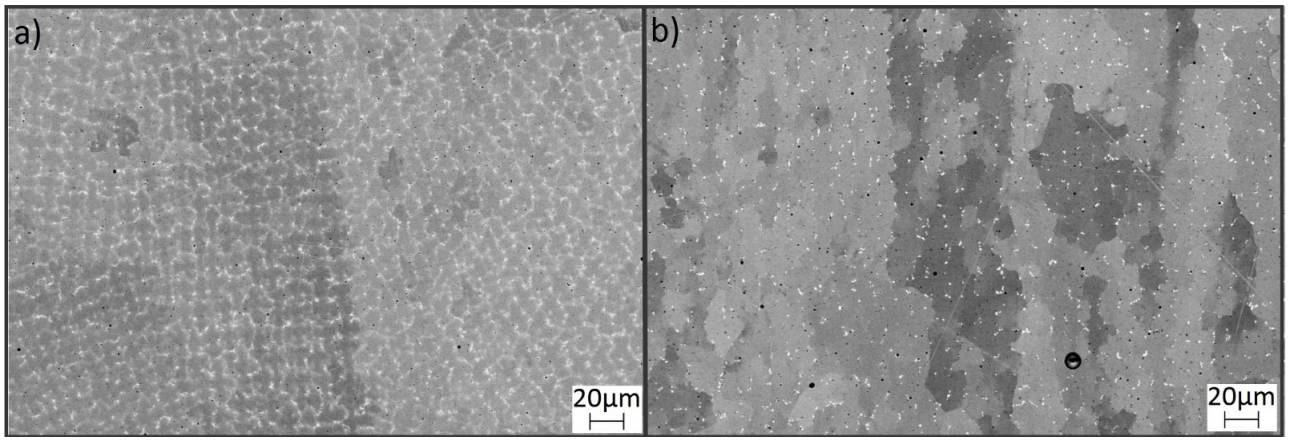

Figure 45: Micro-structures of Top surface; (a) As-build, (b) specimen heat treated for 30 min.

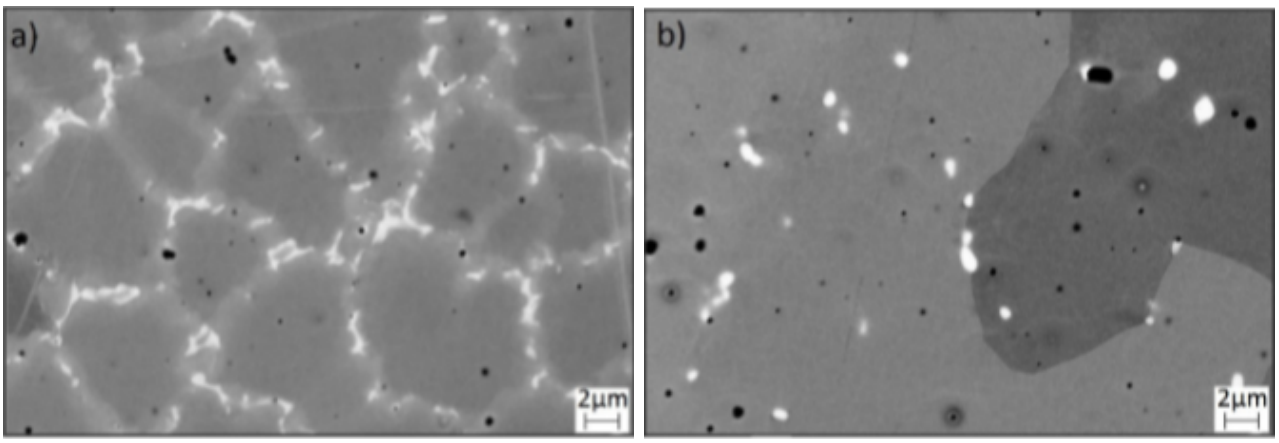

(a) As-build (b) 30 min heat treated

Figure 46: Micro-structures of top surface; (a) As-build, (b) specimen heat treated for 30 min (similar to Figure 45 but with higher magnification)

Cellular structures and melt pools are observed in as-built specimen that can be seen in Figure 47(a). It can also be observed that most of the area is occupied by the cellular grain. Columnar structures, cellular structures and pores of different sizes are also observed in the heat treated specimen that are shown in Figure 47(b).

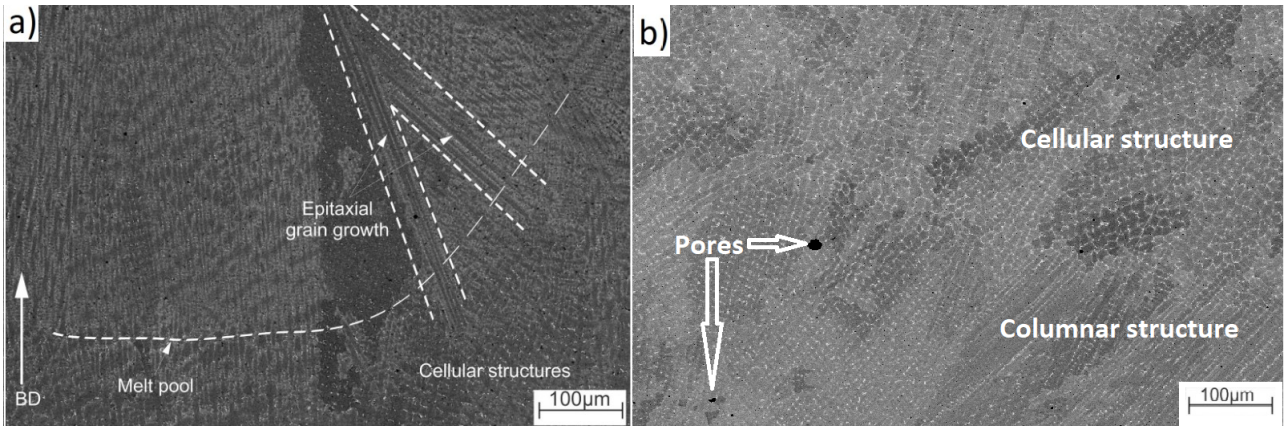

Figure 47: Micro-structures of Top surface; (a) As-build, (b) specimen heat treated for 30 min.

SEM images also showed cracks that are present in these specimens, observed cracks can be of different sizes, see Figure 48. The cracks can greatly influence the mechanical properties of the super alloy, such as reduction in tensile and yield strength and elongation.

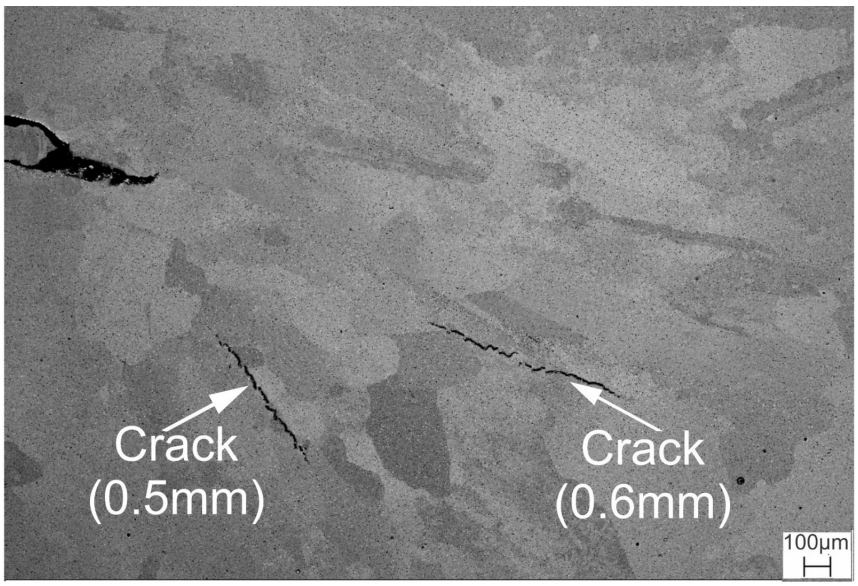

Figure 48: Micro-structure of heat treated specimen (30 min), micro cracks 0.5 mm and 0.6 mm

4.3.3 Electron back-scatter diffraction (EBSD)

Micro-structures, grain size, grain orientation and grain boundaries are observed using EBSD maps. Figure 49 shows EBSD map of as-build specimen (top surface, XY-section). Grain orientation with respect to [001] (Figure 49(c)) indices is shown with different colors and is also applied to all EBSD images in this chapter. It can be seen that grains are of different sizes and the orientation of the grains are random. Randomly oriented grains have different behaviour upon application of external force and are also inconsistent in response to the stress. Measured average grain size is 39 microns (μm) for as build (top surface, XY-section) specimen. Most of the grain show a low mis-orientation angle between 1° and 3.5°, an average mis-orientation angle value of 14.179° and average grain size of 38.8 $\pm$57.33 microns. It is expected to have an-isotropic behaviour in mechanical properties with random orientation of grain size and irregular grain boundaries. Random behaviour is observed in tensile test of as build specimens, see section 4.1.2.

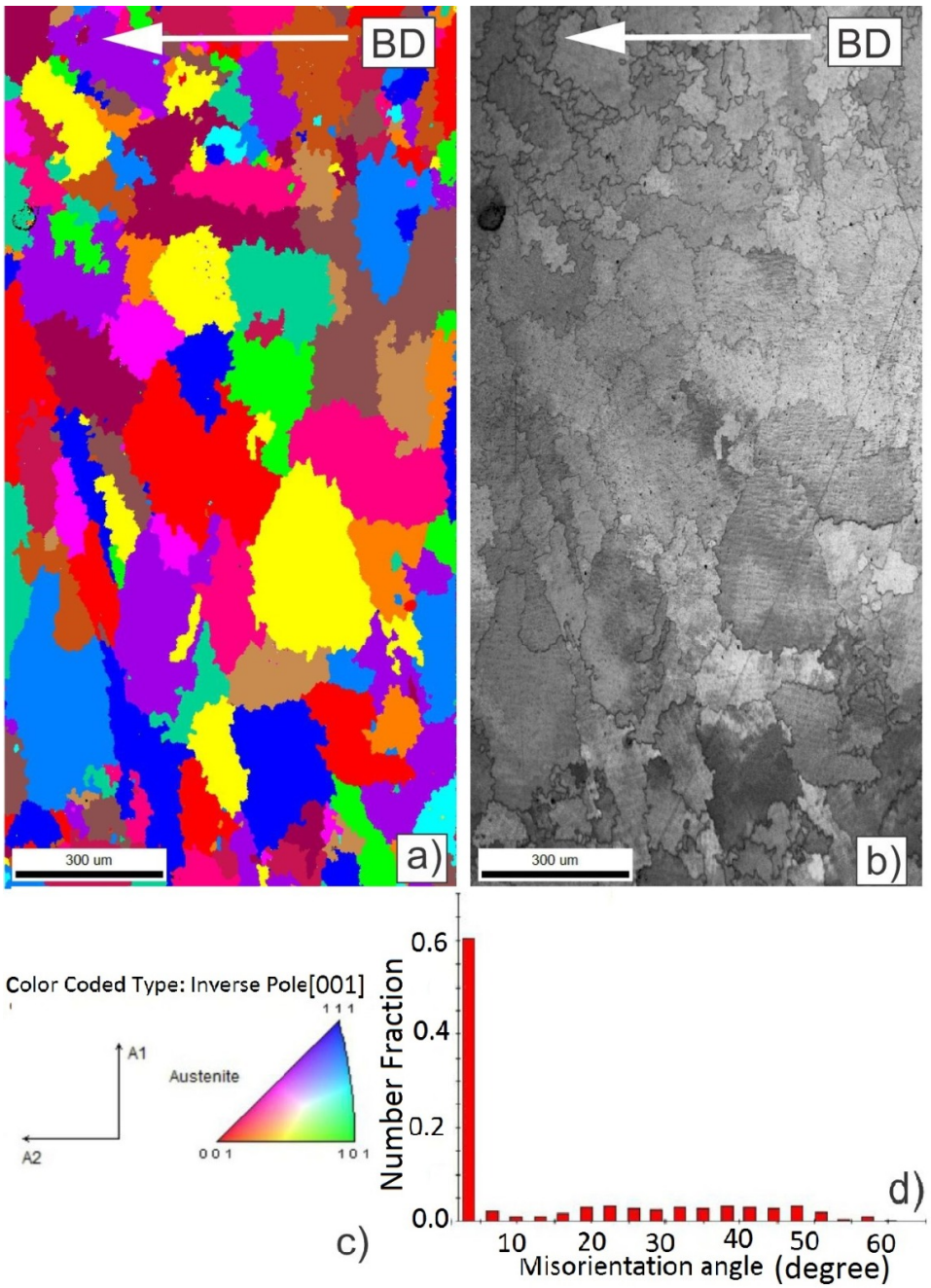

Figure 49: Micro structure of the DED formed Inconel 625 from EBSD analyses: a. EBSD mapping from the as-build specimen, XY-section (top surface), b. Image quality map showing the grain boundaries. c. color coded triangle of the grain orientation, d. misorientation angle distribution of as-build specimen.

EBSD map of heat treated (300 min) specimen (top surface, XY-section) is presented in Figure 50. Change in grain size, grain orientation and micro-structure can be observed on heat treatment. Columnar grains can be observed Figure 50(a). Significant increase in size of the grains can be observed on heat treatment. Grain boundaries are smoother than the boundaries of grains in as-build specimen. Most of the grains in some parts (Figure 50 (e)) show a low misorientation angle between 1° and 3.5° similar to as-build specimen. The results also show the average misorientation angle value of 29.19° and average grain size of 44.6 ±56.978 microns. However, misorientation angle in some place are distributed up to 60°. Comparing the results to the as-build specimen, it is assumed that the release of the residual stress have caused an increase in the average value of the grain size and in increase of misorientation angle. The trend shows that with the increase of heat treatment an increase of grain size and misorientation angle will be observed.

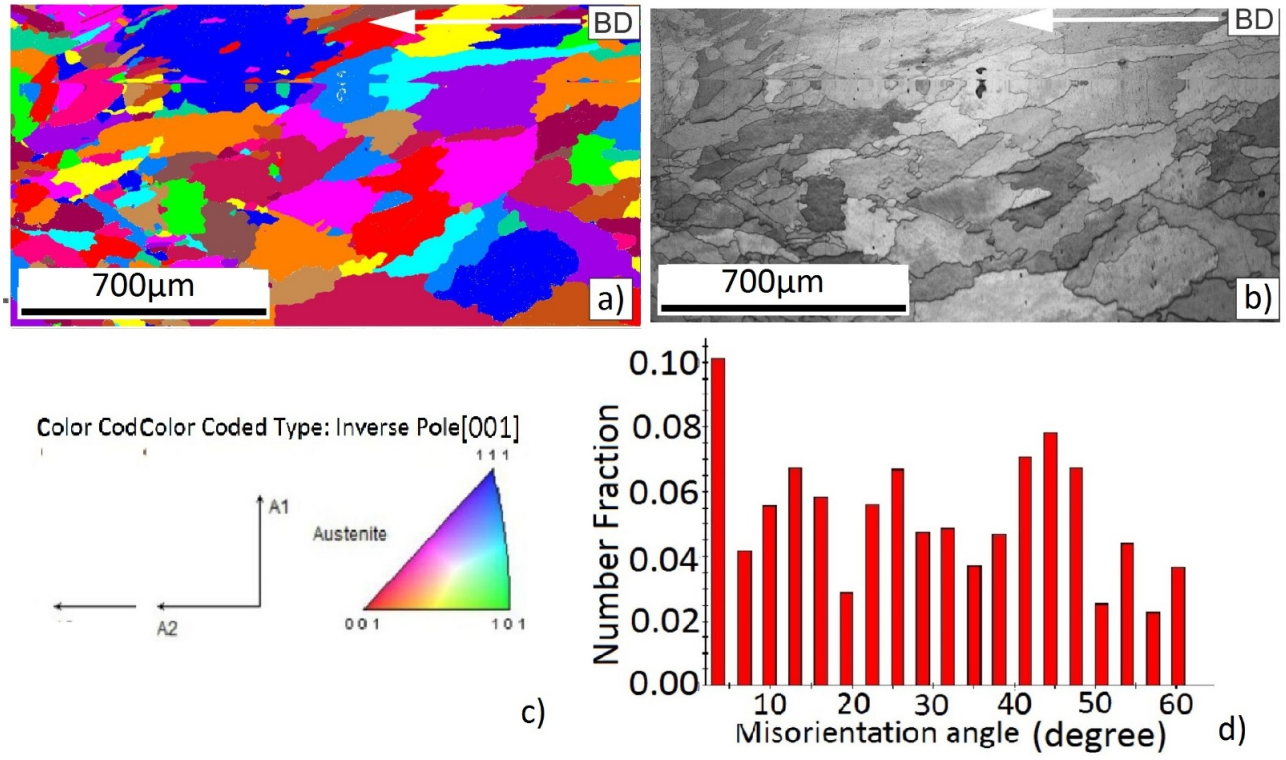

Figure 50: EBSD mapping from the heat treated (300 min) specimen, top surface

4.3.4 Transmission electron microscope (TEM)

The TEM analysis taken of the as-build top-surface (XY-section) shows the dislocations that are illustrated in dark field image (Figure 51). Figure 52 shows the bottom surface of XY-section, the coherent surface may be due to diffusion of elements from the base metal during welding or due to the fast cooling rate. Figure 53 shows a dark field image (with magnification) of the bottom surface (XY-section), dislocation are barely observed beneath the coherent surface.

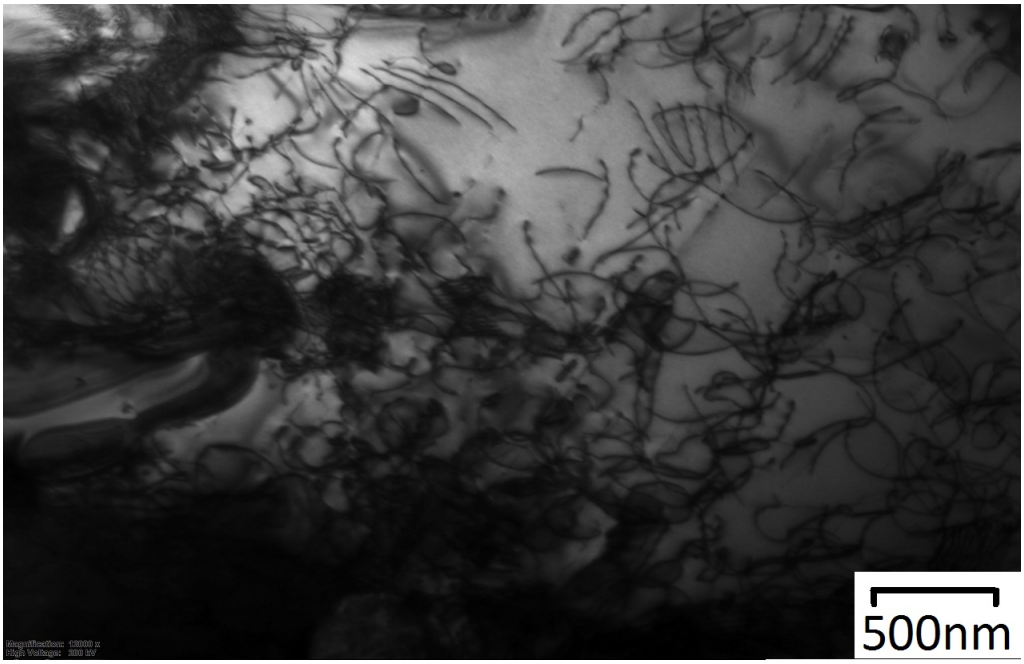

Figure 51: TEM, dark field image of as-build specimen top surface, XY-section

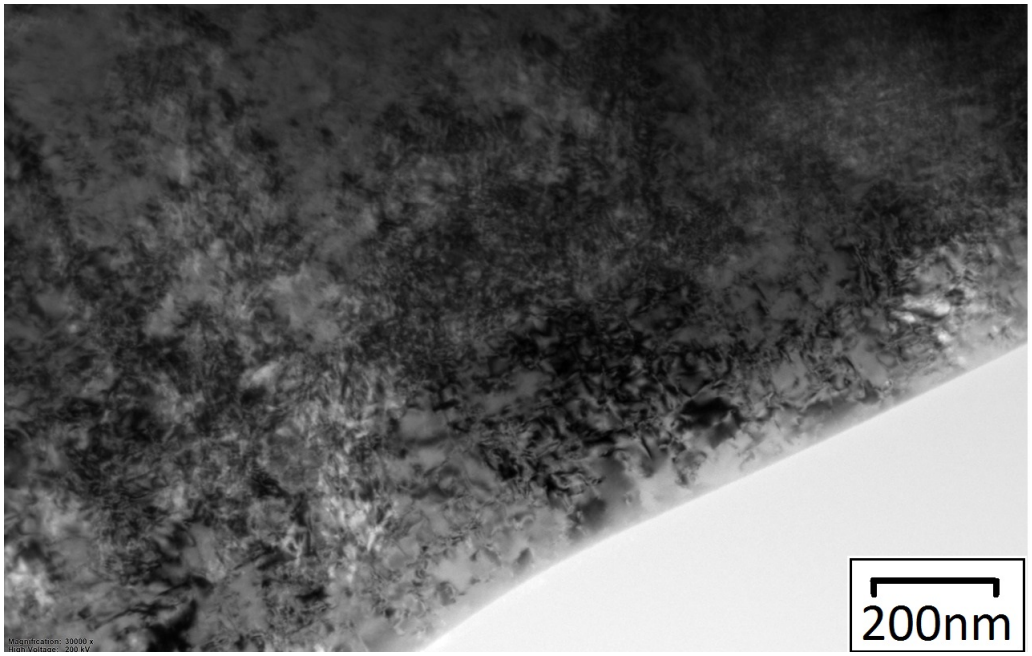

Figure 52: TEM, bright field image of as-build specimen bottom surface, XY-section

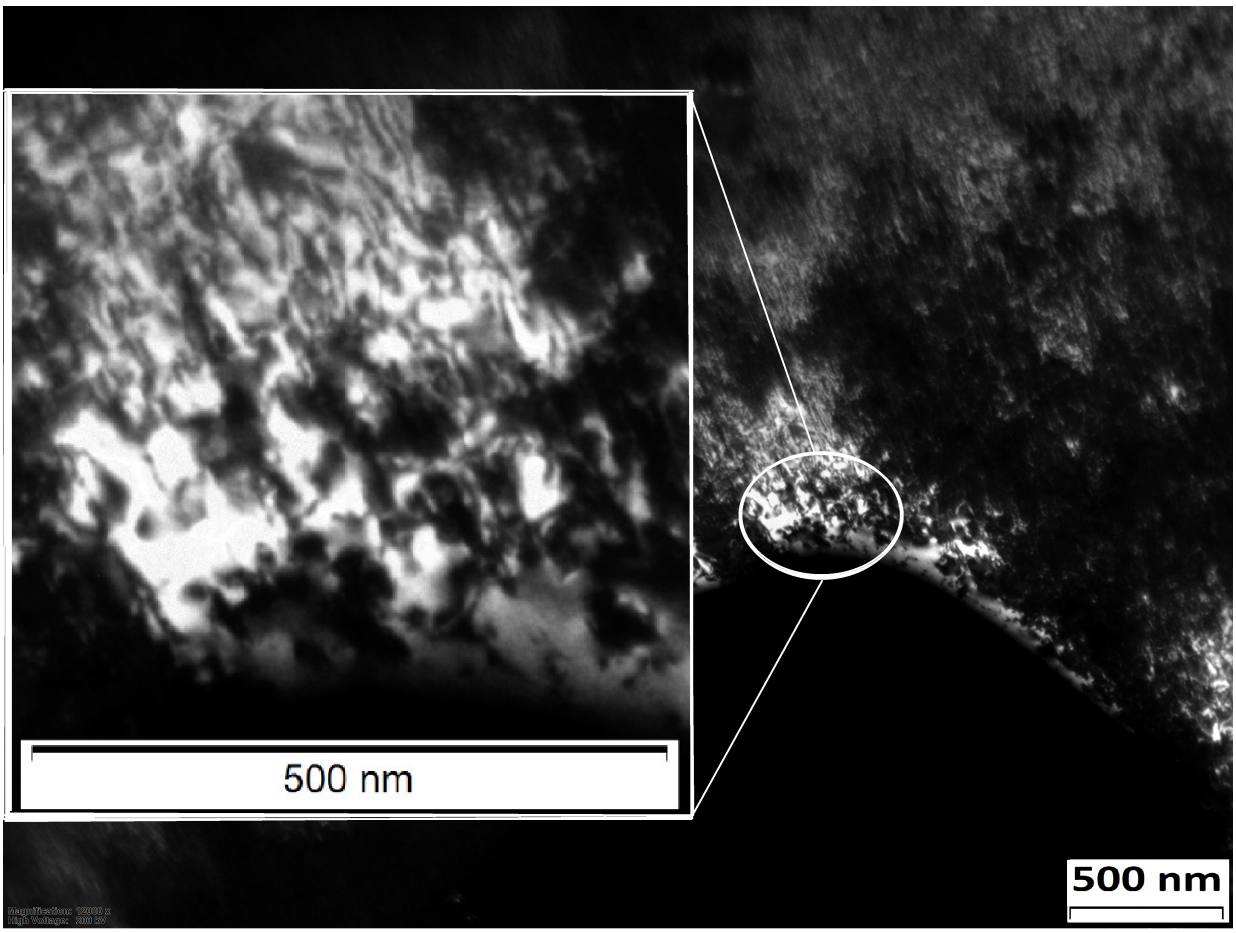

Figure 53: TEM, dark field image of as-build specimen bottom surface, XY-section

5 Discussion

Hardness is an important property of super-alloy that needs to be considered while making parts used at high temperature and pressure conditions. It is observed that the hardness of AM Inconel 625 super alloy decreases on heat treatment. A Significant decrease in the hardness is observed in the specimen that is heat treated for 30 minutes. However, there is a possibility that a similar decrease in hardness may be observed for less heat treatment time e.g. after 15 minutes. Specimens that were heat treated for a longer time (60-, 120- and 300 minutes) showed a little decrease (4HV - 5HV) in average hardness (HV5) value after 30 minutes of heat treatment.

A Significant reduction in hardness after 30 minutes of heat treatment is due to the recovery process. The recovery process starts early with the beginning (approximately within 30 minutes) of heat treatment (1175°C). During the recovery process, partially release of residual stresses occurs causing relaxation in dislocations that are present in as-built specimen.

Readings of hardness (HV5) indentations on YZ-section slightly differ at all the indentation points. This variation is due to presence of residual stresses and welding defects like cracks and pores as shown in Figure 44 and Figure 47 (b). On YZ-section, the highest reading of average hardness is in the middle, observations show that the layer with highest average hardness (HV5) values is present at the junction of two deposited layers (Figure 31). Heat affected zone, coarse grains and residual stresses are present in the proximity of the layer junction that is the possible reason for the high average hardness values. Average hardness (HV5) values are nearly similar for all layers except for two layers considering the standard deviation and confidence interval of average hardness (HV5) value (Figure 31).

The standard deviation of the average hardness readings are within ±10HV. Relatively lower standard deviation of hardness values in most of the areas show that the specimen have relatively uniform properties except in some areas. Considering the confidence interval of 95%, the hardness measurements of 30-, and 300 minutes heat treated specimens are approximately similar (see Table 11).

For as-build specimen, bottom-, middle- and top surfaces (XY-section) of the specimen shows a difference in average hardness and strain values. The bottom surface show highest average hardness i.e. 281HV, the strain reading at bottom surface is $3.756 \cdot 10^{-3}$. Top surface show lowest average hardness i.e. 258HV (Figure 54), the strain reading at top surface is highest i.e. $3.359 \cdot 10^{-3}$ (Figure 54). The difference in hardness and strain values can be related to residual stress and the cooling rate of the deposited layers during additive manufacturing process of Inconel 625 super alloy. Bottom surface has a fast cooling rate as the heat is transferred to the base metal giving a high hardness to the bottom surface. The middle and top surface have slower cooling rate than the bottom surface, resulting in lower hardness as compare to bottom surface. Therefore, if the cooling rate is slow, the hardness will be lower and if the cooling rate is fast the hardness will be higher.

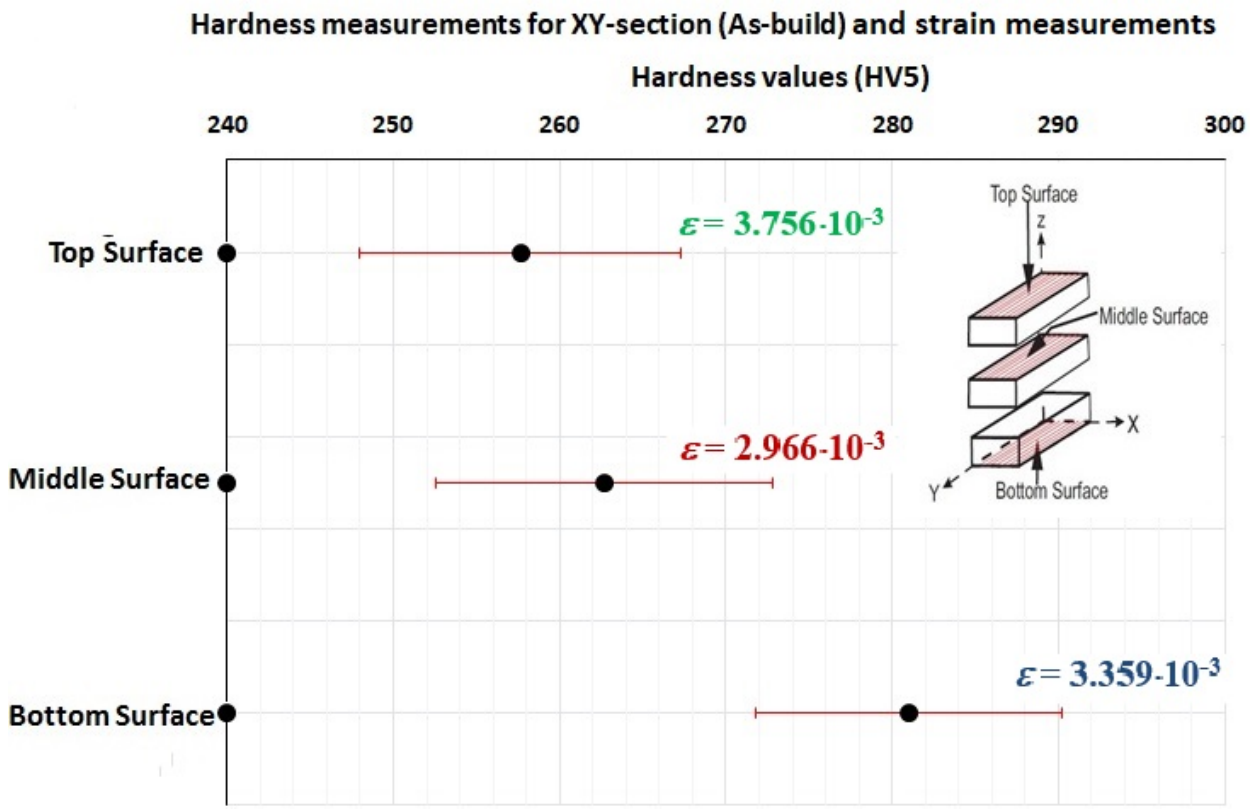

Figure 54: Average hardness and strain measurements((ϵ) at top, middle and bottom surface.

Another important property to be considered while selecting an alloy for manufacturing of parts used in high temperature and high pressure conditions is tensile strength. A decrease in tensile strength after heat treatment of Inconel 625 specimens is observed. The E-modulus, UTS, yield strength and percentage of elongation values for identical tested pairs of as-build

and heat treated specimen seems partially inconsistent.

Different values of ultimate tensile strength and percentage of elongation are observed in two as-built specimens used for tensile test. As-build specimen-2 show lower tensile strength and percentage of elongation (Table 14). The as-build specimen-2 developed fracture at 25% elongation as compared to as-build specimen-1 which showed elongation up-to 39% before fracture. Inconsistency in the readings is due to presence of welding defects, that affect both hardness and tensile strength. Concluding that casting defects and in-homogeneity can greatly affect the mechanical properties of the super alloy.

For heat treated specimens, it can be observed that the percentage of elongation increase with the increase in heat treatment time in response to similar tensile stress (see figure 36). This increase in percentage of elongation is due to partial release of residual stresses and relaxation of dislocations due to heat treatment.

No necking was observed in both as-build and heat treated specimens upon application of tensile strength, a sudden fracture was observed in all specimens. The fractures fall it category of brittle fracture i.e. no appreciable plastic deformation occurred at fracture point before fracturing (Figure 37). The fractures are diagonal, either fracture followed a welding defect such as micro fracture as shown in optical microscope image (Figure 43) or crystal cleavage.

Columnar and cellular structures with heavy, bright and segregated elements are observed in as-build specimen (Figure 47). Due to heat treatment the grain boundaries become clearly visible (Figure 47 b) with segregates of heavy elements. In heat treated specimens equiaxed grains were observed, which can sometimes be considered as a recrystalization of the microstructures. However, there was no evidence of recrystalization in all heat treated specimens.

EDS analysis of heat treated specimens shows that there was no change in chemical composition on heat treatment. The electron backs scatter (EBSD) results shows an increase in the misorientation angle up to 60° for 300 minute heat treated specimens. This increase in misorentation angle contribute to reduction of hardness and yield strength of heat treated specimens compare to as-build specimen.

TEM images of the top surface (XY-section) shows the presence of dislocations (Figure 51),

while the bottom surface shows a coherent structure where the dislocations are not easily observed (Figure 52). The bottom surface is coherent possibly due to the diffusion of elements from the base metal or the fast cooling rate. Diffusion of elements from the base metal can also cause an increase in hardness. However, EDS analysis shows that there was no change in the chemical composition in the bottom surface (XY-section) compared to middle and top surface. Considering that there is no chemical change, the diffusion of elements from bottom surface didn't happened. It could be concluded that the rapid cooling rate maybe the reason for this coherent bottom surface.

5.1 Future work

Limited access to the labs due to covid-19 situation had negatively impacted the experimental work. Further studies is required to improve understanding of mechanical properties of additive manufactured Inconel 625 by DED. Followings are recommendations for further work:

- Tensile test specimens using different printing directions and patterns can be tested e.g. horizontally printed tensile test specimen. This will provide information about impact of direction of printing on mechanical properties.
- Applying heat treatment followed by HIP can possibly improve mechanical properties, which needs to be tested.
- Heating base material before starting printing process of super alloy can help in maintaining uniform mechanical properties through out the alloy specimen, which also need to bested.
- Comparing the mechanical properties of a wrought and a reverse engineered Inconel 625, will also provide an opportunity to understand the difference between mechanical properties of both alloy types.
- Fracture surfaces needs to be studied using scanning electron microscope (SEM) in order to understand the fracture behaviour.

6 Conclusion

Mechanical and micro-structural properties of additive manufactured Inconel 625 produced by Direct energy deposition (DED) were studied in both as-build state and heat treated (1175°C) condition. Following results are concluded:

1. The effect of heat treatment (1175°C) on the residual stresses resulted in reduction of average hardness (HV5), yield strength, average UTS and average E-modulus. Therefore, resulting an increase in percentage of elongation.

2. Increase in misorientation angle of grains occur due to heat treatment resulting in decrease of hardness and yield strength.

3. Difference in average hardness at top, middle and bottom surface (XY-section) of the specimen is depends on the cooling rate.

4. Welding defects have a great influence on the mechanical properties such as yield strength and hardness. Pores, cracks were observed in all of the specimens. Showing welding defects does not disappear on heat treatment.

5. Release of residual stresses resulted in a positive impact on heat treated specimen improving the consistency of the super alloy's structural integrity.

6. Misorientation angles distribution changed upon heat treatment due to decrease of the residual strain. With an increase of the grain boundary angle a decrease of the residual stress is observed.

7. No carbides, intermetallic phases or other precipitation are observed in as-build and heat treated specimen. Heat treatment time longer than 300 minutes is required for the process of precipitation to occur.

8. Epitaxial grain growth may happen during the printing process. Similarly, cellular and columnar structures develop in DED printing of super alloy.

9. No change in chemical composition or recrystallization occur for heat treatment of 300 minutes at 1175°C. However, occurrence of recovery stage is observed on heat treatment.

References

[1] H. Eiselstein and D. Tillack, "The invention and definition of alloy 625", *Superalloys*, vol. 718, no. 625, pp. 1–14, 1991.

[2] B. Dutta, S. Babu, and B. H. Jared, *Science, technology and applications of metals in additive manufacturing*. Elsevier, 2019.

[3] G. Marchese, X. Garmendia Colera, F. Calignano, M. Lorusso, S. Biamino, P. Minetola, and D. Manfredi, "Characterization and comparison of inconel 625 processed by selective laser melting and laser metal deposition", *Advanced Engineering Materials*, vol. 19, no. 3, p. 1 600 635, 2017.

[4] A. Nayyar and A. Kumar, *A roadmap to industry 4.0: Smart production, sharp business and sustainable development*.

[5] J. I. Arrizubieta, M. Cortina, A. Mendioroz, A. Salazar, and A. Lamikiz, "Thermal diffusivity measurement of laser-deposited aisi h13 tool steel and impact on cooling performance of hot stamping tools", *Metals*, vol. 10, no. 1, p. 154, 2020.

[6] Z. Yan, W. Liu, Z. Tang, X. Liu, N. Zhang, M. Li, and H. Zhang, "Review on thermal analysis in laser-based additive manufacturing", *Optics & Laser Technology*, vol. 106, pp. 427–441, 2018.

[7] A. Dass and A. Moridi, "State of the art in directed energy deposition: From additive manufacturing to materials design", *Coatings*, vol. 9, no. 7, p. 418, 2019.

[8] T. Á. Tejedor, "Gas turbine materials selection, life management and performance improvement", in *Power Plant Life Management and Performance Improvement*, Elsevier, 2011, pp. 330–419.

[9] D. Klarstrom, "Characteristics of nickel and nickel-base alloys", *ASM Handbook*, vol. 13, pp. 641–43, 1992.

[10] G. E. Dieter and D. Bacon, *Mechanical metallurgy*. McGraw-hill New York, 1986, vol. 3.

[11] A. P. Mouritz, *Introduction to aerospace materials*. Elsevier, 2012.

[12] K. R. Trethewey and J. Chamberlain, "Corrosion for science and engineering", 1995.

[13] P. A. Schweitzer *et al.*, *Fundamentals of metallic corrosion: atmospheric and media corrosion of metals*. CRC press, 2006.

[14] D. Murfet, *Inconel alloy 625*, Accessed: 5-3-2020.

[15] W. F. Smith, *Structure and properties of engineering alloys*. McGraw-Hill, 1993, pp. 487–536.

[16] E. Torres, R. Caram, and A. J. Ramirez, "Grain boundary sliding phenomenon and its effect on high temperature ductility of ni-base alloys", in *Materials science forum*, Trans Tech Publ, vol. 638, 2010, pp. 2858–2863.

[17] S. Metals, "High-performance alloys for resistance to aqueous corrosion", *SM Aqueous Corrosion Book*, p. 28, 2000.

[18] D. Verdi, M. Garrido, C. J. Múnez, and P. Poza, "Cr3c2 incorporation into an inconel 625 laser cladded coating: Effects on matrix microstructure, mechanical properties and local scratch resistance", *Materials & Design*, vol. 67, pp. 20–27, 2015.

[19] J. R. Davis *et al.*, *Nickel, cobalt, and their alloys*. ASM international, 2000.

[20] AZoM, *The properties and effects of manganese as an alloying element*. [Online]. Available: `https://www.azom.com/article.aspx?ArticleID=13027/%5C~%7B%7Duno/abcde.html`.

[21] X. Xie, X. Liu, Y. Hu, B. Tang, Z. Xu, J. Dong, K. Ni, Y. Zhu, S. Tien, L. Zhang, *et al.*, "The role of phosphorus and sulfur in inconel 718", *Superalloys 1996*, vol. 599, 1996.

[22] D. Herzog, V. Seyda, E. Wycisk, and C. Emmelmann, "Additive manufacturing of metals", *Acta Materialia*, vol. 117, pp. 371–392, 2016.

[23] L. Yang, K. Hsu, B. Baughman, D. Godfrey, F. Medina, M. Menon, and S. Wiener, *Additive manufacturing of metals: the technology, materials, design and production*. Springer, 2017, pp. 23–24.

[24] P. A. Pidge and H. Kumar, "Additive manufacturing: A review on 3 d printing of metals and study of residual stress, buckling load capacity of strut members", *Materials Today: Proceedings*, 2019.

[25] L. Yang, K. Hsu, B. Baughman, D. Godfrey, F. Medina, M. Menon, and S. Wiener, *Additive manufacturing of metals: the technology, materials, design and production*. Springer, 2017, pp. 37–39.

[26] R. Koike, T. Misawa, T. Aoyama, and M. Kondo, "Controlling metal structure with remelting process in direct energy deposition of inconel 625", *CIRP Annals*, vol. 67, no. 1, pp. 237–240, 2018.

[27] engineeringproductdesign, *Direct energy deposition (ded)*. [Online]. Available: `https://engineeringproductdesign.com/knowledge-base/direct-energy-deposition/`.

[28] A. Wimmer, C. G. Kolb, M. Assi, J. Favre, A. Bachmann, A. Fraczkiewicz, and M. F. Zaeh, "Investigations on the influence of adapted metal-based alloys on the process of laser beam melting", *Journal of Laser Applications*, vol. 32, no. 2, p. 022 029, 2020.

[29] Z. Wang, E. Denlinger, P. Michaleris, A. D. Stoica, D. Ma, and A. M. Beese, "Residual stress mapping in inconel 625 fabricated through additive manufacturing: Method for neutron diffraction measurements to validate thermomechanical model predictions", *Materials & Design*, vol. 113, pp. 169–177, 2017.

[30] Z. Wang and A. M. Beese, "Effect of chemistry on martensitic phase transformation kinetics and resulting properties of additively manufactured stainless steel", *Acta Materialia*, vol. 131, pp. 410–422, 2017.

[31] W. J. Sames, F. List, S. Pannala, R. R. Dehoff, and S. S. Babu, "The metallurgy and processing science of metal additive manufacturing", *International Materials Reviews*, vol. 61, no. 5, pp. 315–360, 2016.

[32] L. N. Carter, M. M. Attallah, and R. C. Reed, "Laser powder bed fabrication of nickel-base superalloys: Influence of parameters; characterisation, quantification and mitigation of cracking", *Superalloys*, vol. 2012, pp. 577–586, 2012.

[33] K. Kempen, L. Thijs, B. Vrancken, S. Buls, J. Van Humbeeck, and J. Kruth, "Producing crack-free, high density m2 hss parts by selective laser melting: Pre-heating the baseplate", in *Proc. 24th Int. Solid Free. Fabr. Symp*, 2013, pp. 131–139.

[34] A. Hussein, L. Hao, C. Yan, R. Everson, and P. Young, "Advanced lattice support structures for metal additive manufacturing", *Journal of Materials Processing Technology*, vol. 213, no. 7, pp. 1019–1026, 2013.

[35] R. Nalla, R. Ritchie, B. Boyce, J. Campbell, and J. Peters, "Influence of microstructure on high-cycle fatigue of ti-6al-4v: Bimodal vs. lamellar structures", *Metallurgical and Materials Transactions A*, vol. 33, no. 3, pp. 899–918, 2002.

[36] A. Prabhu, T. Vincent, A. Chaudhary, W. Zhang, and S. Babu, "Effect of microstructure and defects on fatigue behaviour of directed energy deposited ti–6al–4v", *Science and Technology of Welding and Joining*, vol. 20, no. 8, pp. 659–669, 2015.

[37] C. J. Hassila, P. Harlin, and U. Wiklund, "Rolling contact fatigue crack propagation relative to anisotropies in additive manufactured inconel 625", *Wear*, vol. 426, pp. 1837–1845, 2019.

[38] Z. Tian, C. Zhang, D. Wang, W. Liu, X. Fang, D. Wellmann, Y. Zhao, and Y. Tian, "A review on laser powder bed fusion of inconel 625 nickel-based alloy", *Applied Sciences*, vol. 10, no. 1, p. 81, 2020.

[39] Q. Chen, G. Guillemot, C.-A. Gandin, and M. Bellet, "Three-dimensional finite element thermomechanical modeling of additive manufacturing by selective laser melting for ceramic materials", *Additive Manufacturing*, vol. 16, pp. 124–137, 2017.

[40] R. Heim, *Structural durability: Methods and concepts*.

[41] C. Li, Z. Liu, X. Fang, and Y. Guo, "Residual stress in metal additive manufacturing", *Procedia Cirp*, vol. 71, pp. 348–353, 2018.

[42] Y. Kudryavtsev and J. Kleiman, "Residual stress management: Measurement, fatigue analysis and beneficial redistribution, x int", in *Congress and Exposition on Experimental and Applied Mechanics (Costa Mesa, 2004) pp*, pp. 1–8.

[43] R. Acevedo, P. Sedlak, R. Kolman, and M. Fredel, "Residual stress analysis of additive manufacturing of metallic parts using ultrasonic waves: State of the art review", *Journal of Materials Research and Technology*, 2020.

[44] R. Chakrabarti, P. Biswas, and S. Saha, "A review on welding residual stress measurement by hole drilling technique and its importance", *Journal of Welding and Joining*, vol. 36, no. 4, pp. 75–82, 2018.

[45] M. E. Fitzpatrick, A. T. Fry, P. Holdway, F. Kandil, J. Shackleton, and L. Suominen, "Determination of residual stresses by x-ray diffraction.", 2005.

[46] A. Steuwer, J. Santisteban, M. Turski, P. Withers, and T. Buslaps, "High-resolution strain mapping in bulk samples using full-profile analysis of energy-dispersive synchrotron x-ray diffraction data", *Journal of applied crystallography*, vol. 37, no. 6, pp. 883–889, 2004.

[47] ——, "High-resolution strain mapping in bulk samples using full-profile analysis of energy dispersive synchrotron x-ray diffraction data", *Nuclear Instruments and Methods in Physics Research Section B: Beam Interactions with Materials and Atoms*, vol. 238, no. 1-4, pp. 200–204, 2005.

[48] I. C. Noyan and J. B. Cohen, *Residual stress: measurement by diffraction and interpretation*. Springer, 2013.

[49] S. Paranjpe, "Measurement of residual stress in materials using neutrons", in *Proc. of a Technical Meeting (Held Vienna, 13–17 October 2003)*, 2005.

[50] A. J. Wilkinson and T. B. Britton, "Strains, planes, and ebsd in materials science", *Materials today*, vol. 15, no. 9, pp. 366–376, 2012.

[51] S. Abuku and B. Cullity, "A magnetic method for the determination of residual stress", *Experimental Mechanics*, vol. 11, no. 5, pp. 217–223, 1971.

[52] S. Silva, T. Mansur, and E. Palma, "Determining residual stresses in ferromagnetic materials by barkhausen noise measurement", in *Proceedings of 15th World Conference on Nondestructive Testing, Roma*, 2000.

[53] S. Kokubo, "On the change in hardness of a plate caused by bending", *Science Reports of the Tohoku Imperial University*, vol. 21, pp. 256–267, 1932.

[54] J. I. Jang, "Estimation of residual stress by instrumented indentation: A review", *J. Ceram. Process. Res*, vol. 10, no. 3, pp. 391–400, 2009.

[55] P. Harwood, "Residual stress determination using hardness testing", Bachelor's Thesis, University of Limerick, Aug. 2018.

[56] Q. Zhang, Y. Chang, L. Gu, Y. Luo, and B. Ge, "Study of microstructure of nickel-based superalloys at high temperatures", *Scripta Materialia*, vol. 126, pp. 55–57, 2017.

[57] B. Dubiel and J. Sieniawski, "Precipitates in additively manufactured inconel 625 superalloy", *Materials*, vol. 12, no. 7, p. 1144, 2019.

[58] G. Dinda, A. Dasgupta, and J. Mazumder, "Laser aided direct metal deposition of inconel 625 superalloy: Microstructural evolution and thermal stability", *Materials Science and Engineering: A*, vol. 509, no. 1-2, pp. 98–104, 2009.

[59] A. H. Committee *et al.*, "Asm handbook volume 4 heat treating", *ASM Standards, American Society for Metals, Materials Park, OH*, 1991.

[60] I. Z. Awan and A. Q. Khan, "Recovery, recrystallization, and grain-growth", *Journal of the Chemical Society of Pakistan*, vol. 41, no. 1, pp. 1–1, 2019.

[61] S. Goel, M. Ahlfors, F. Bahbou, and S. Joshi, "Effect of different post-treatments on the microstructure of ebm-built alloy 718", *Journal of Materials Engineering and Performance*, vol. 28, no. 2, pp. 673–680, 2019.

[62] P. J. Goodhew and J. Humphreys, *Electron microscopy and analysis*. CRC Press, 2000.

[63] A. Chauhan, "Deformation and damage mechanisms of ods steels under high-temperature cyclic loading", 2018.

[64] J. K. S. $\cdot V.Hansen$, "Introduction to transmission electron microscopy", COmpendium produced at University of Stavanger.

[65] V. H. Jan Ketil Solberg, *Introduction to transmission electron microscopy*, Accessed: 5-5-2020.

[66] S. K. Rai, A. Kumar, V. Shankar, T. Jayakumar, K. B. S. Rao, and B. Raj, "Characterization of microstructures in inconel 625 using x-ray diffraction peak broadening and lattice parameter measurements", *Scripta materialia*, vol. 51, no. 1, pp. 59–63, 2004.

[67] P. Scott A Speakman, *Introduction to x-ray powder diffraction data analysis*, Accessed: 5-5-2020.

[68] W. D. Callister and D. G. Rethwisch, *Materials science and engineering*. John wiley & sons NY, 2011, vol. 5.

[69] H. A. Youssef, H. A. El-Hofy, and M. H. Ahmed, *Manufacturing technology: materials, processes, and equipment*. Crc Press, 2011.

[70] P. Sassatelli, G. Bolelli, M. L. Gualtieri, E. Heinonen, M. Honkanen, L. Lusvarghi, T. Manfredini, R. Rigon, and M. Vippola, "Properties of hvof-sprayed stellite-6 coatings", *Surface and Coatings Technology*, vol. 338, pp. 45–62, 2018.

A Appendix for Average hardness measurements

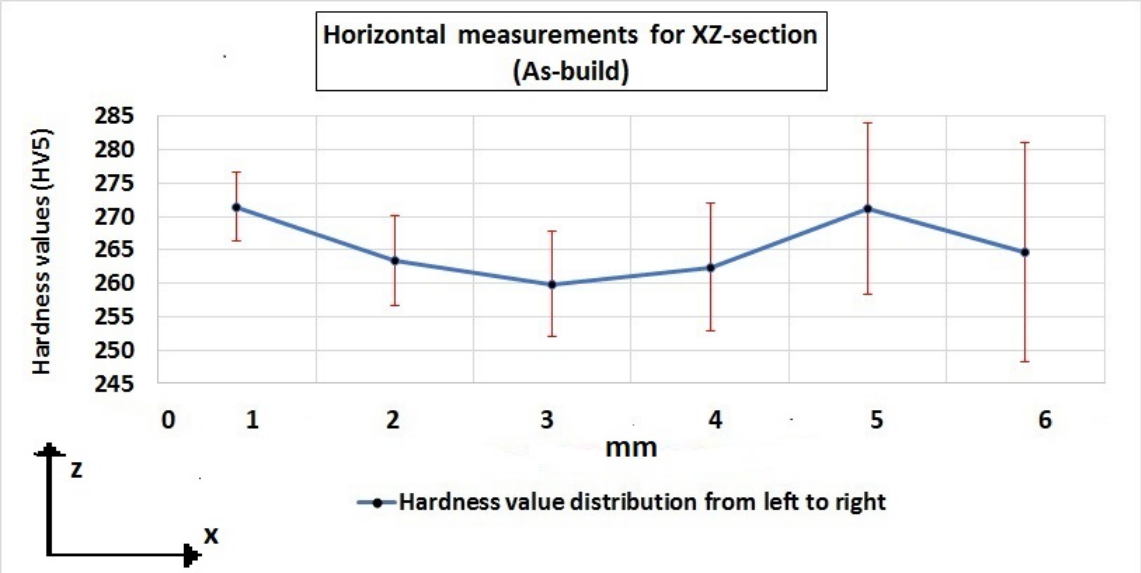

Figure 55: Horizontal average hardness measurements XZ-section (As-build).

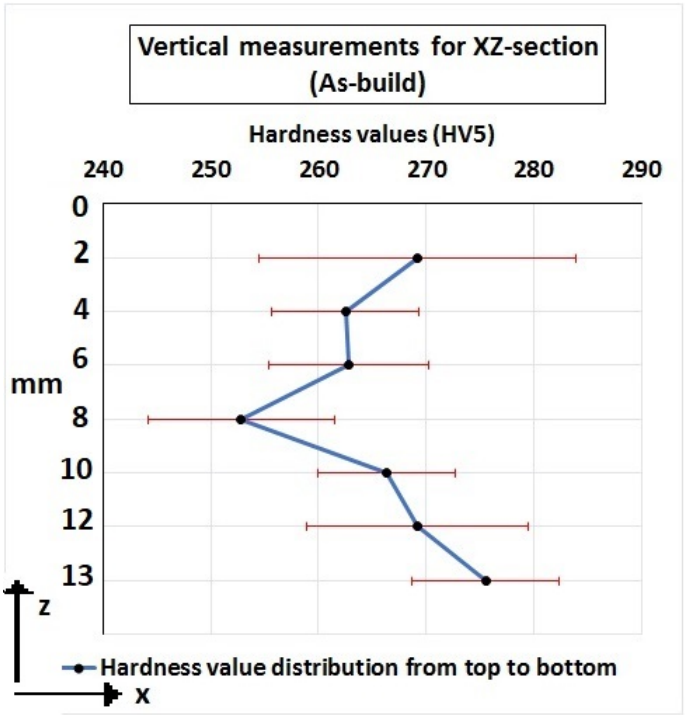

Figure 56: Vertical average hardness measurements XZ-section (As-build).

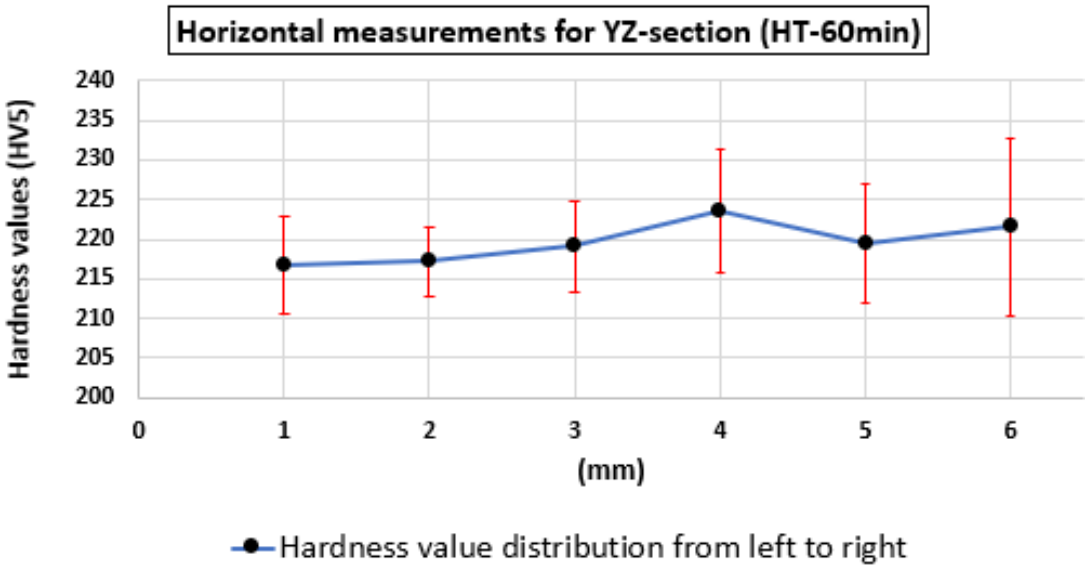

Figure 57: Horizontal average hardness measurements XZ-section (HT-60min).

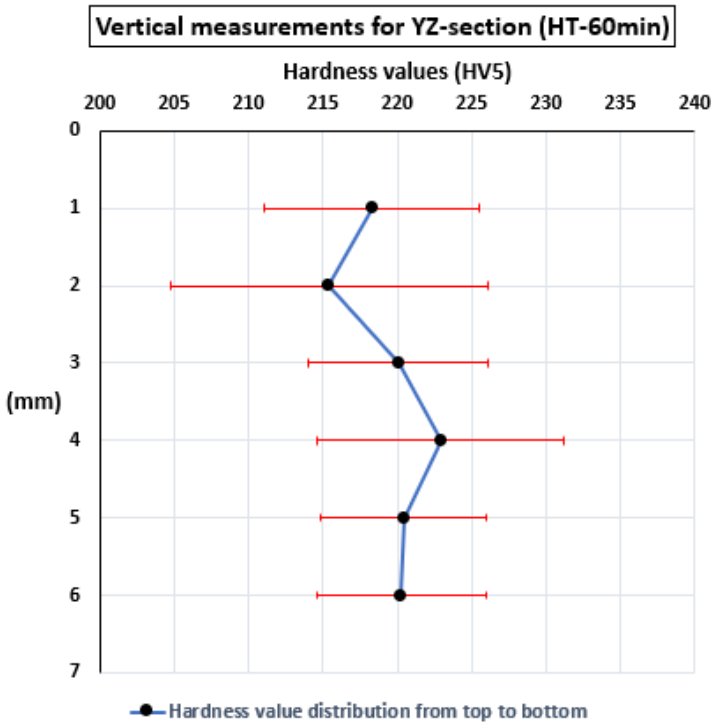

Figure 58: Vertical average hardness measurements XZ-section (HT-60min).

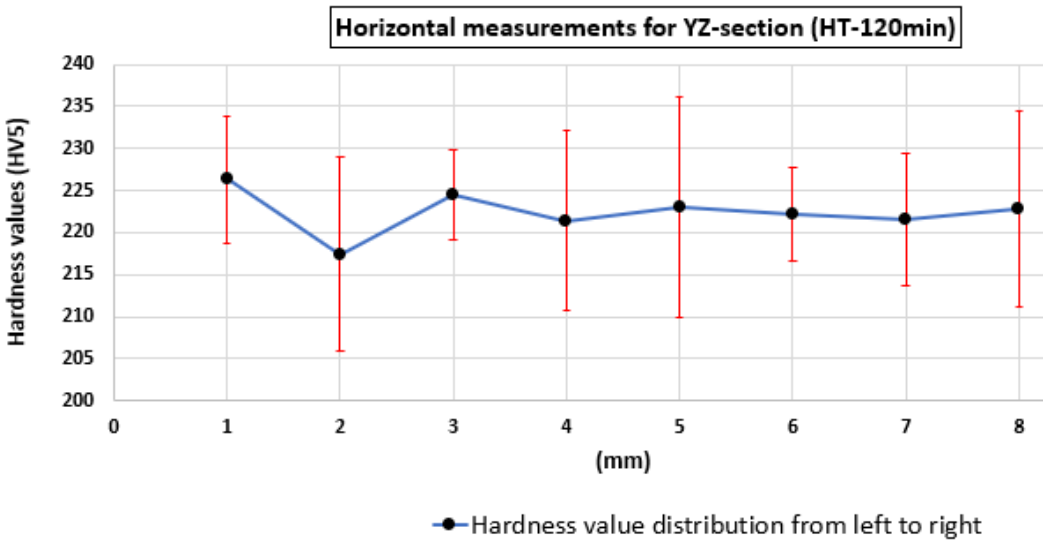

Figure 59: Horizontal average hardness measurements XZ-section (HT-120min).

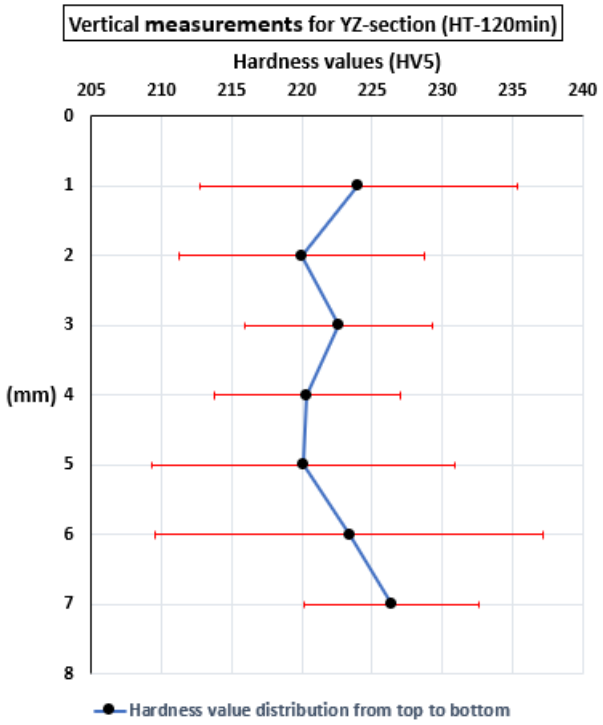

Figure 60: Vertical average hardness measurements XZ-section (HT-120min).

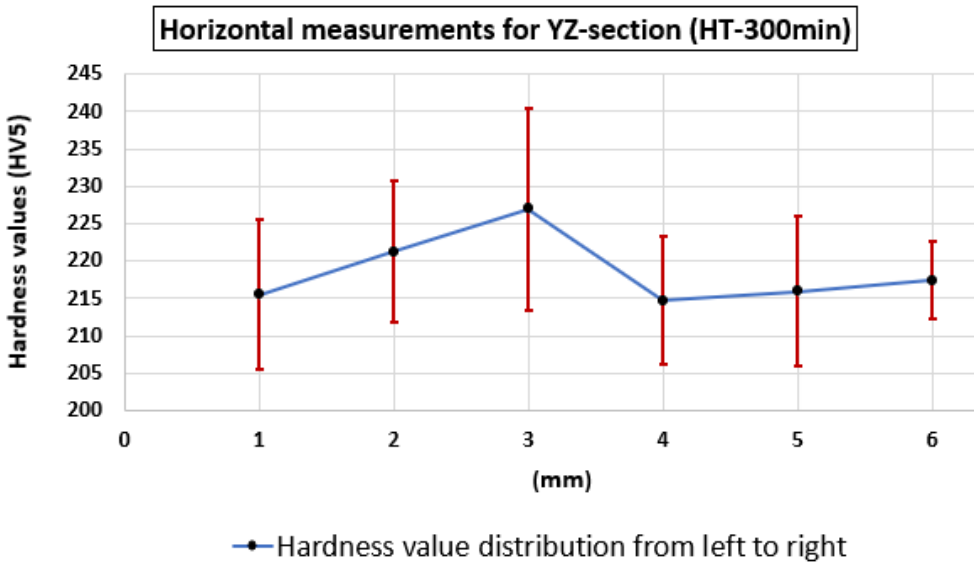

Figure 61: Horizontal average hardness measurements XZ-section (HT-300min).

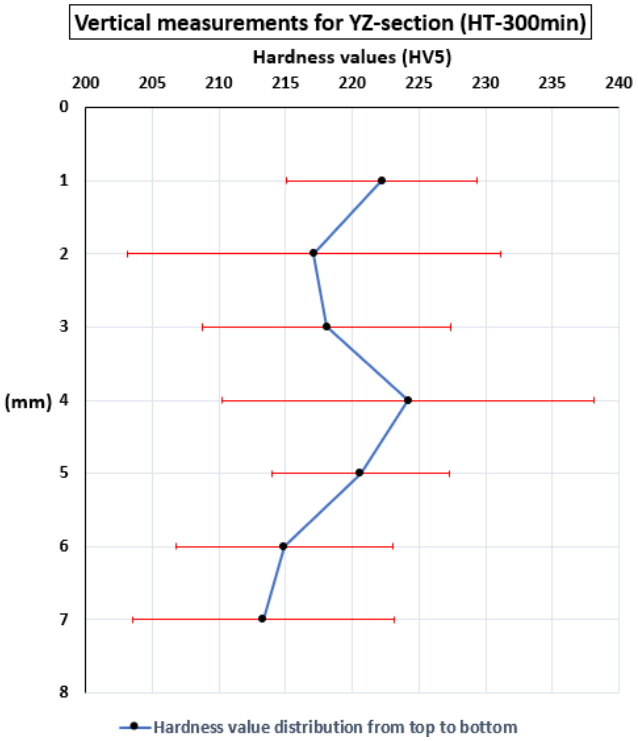

Figure 62: Vertical average hardness measurements XZ-section (HT-300min).

B Appendix for SEM images

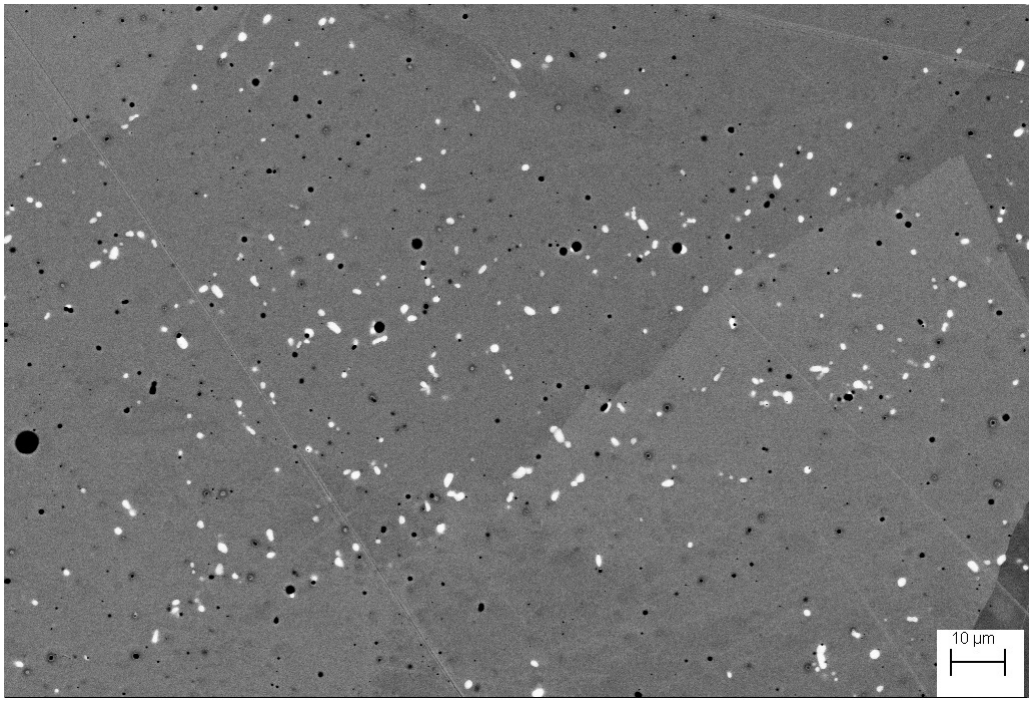

Figure 63: Segregated heavy elements, pores, XY-section, heat treated for 120 minutes.

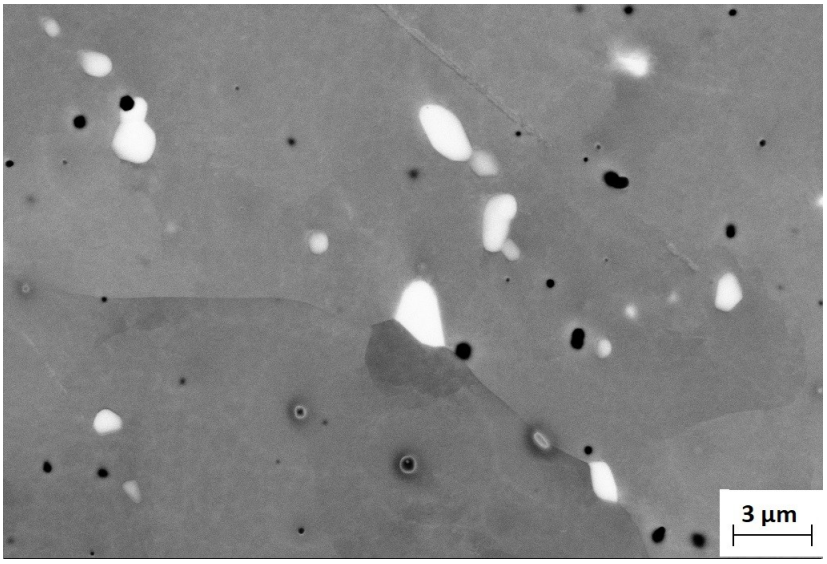

Figure 64: Segregated heavy elements, pores, XY-section, heat treated for 300 minutes.

oerlikon metco

Inspection Certificate
EN 10204 - 3.1

Oerlikon Metco Europe GmbH
Spreestrasse 2
D-65451 KELSTERBACH
Phone: +49 6142 6033 0
Fax: +49 6142 6033 400

WESTAD INDUSTRI AS
Heggenveien 530
3360 GEITHUS
NORWEGEN

Shipping Doc/Date
800472712 / 27.01.2017

Customer PO: Thomas
PO: 200274654
Product: 1075751 MetcoClad 625 / 10#
Quantity: 20,000 LB

Lot No: 451473

Characteristic	Inspection Method	Value	Unit
Chemical Analysis			
Al		0,02	WT%
C		0,01	WT%
Co		< 0,1	WT%
Cr		21,8	WT%
Fe		4,0	WT%
Mn		0,3	WT%
Mo		8,9	WT%
Nb		3,98	WT%
Ni		60,29	WT%
Si		0,4	WT%
Ti		< 0,1	
T.A.O.		< 0,10	WT%
Other Tests			
A.D.		4,5	G/CC
Flowrate		15	s/50g
Sieve Size			
+140 mesh (106 µm)		0	WT%
+170 mesh (90 µm)		3	WT%
-170 +325 mesh		95	WT%
-325 mesh (45 µm)		2	WT%
-400 mesh (38 µm)		0	WT%

Approved Specifications:
Internal Specification
Material produced / packaged, inspected and released by Oerlikon Metco (US) Inc., Troy, MI unless otherwise stated.

Trace element analysis and any required metallurgical analysis is performed by a qualified Nadcap approved laboratory. Any element reported as less than 50 ppm is considered as a trace element except for Carbon, Sulfur, Oxygen, Nitrogen and Hydroger Details available upon request.

By i.V.
Quality Assurance Representative on behalf of
Joern Lindner

C Appendix for EDS analysis (As-build)

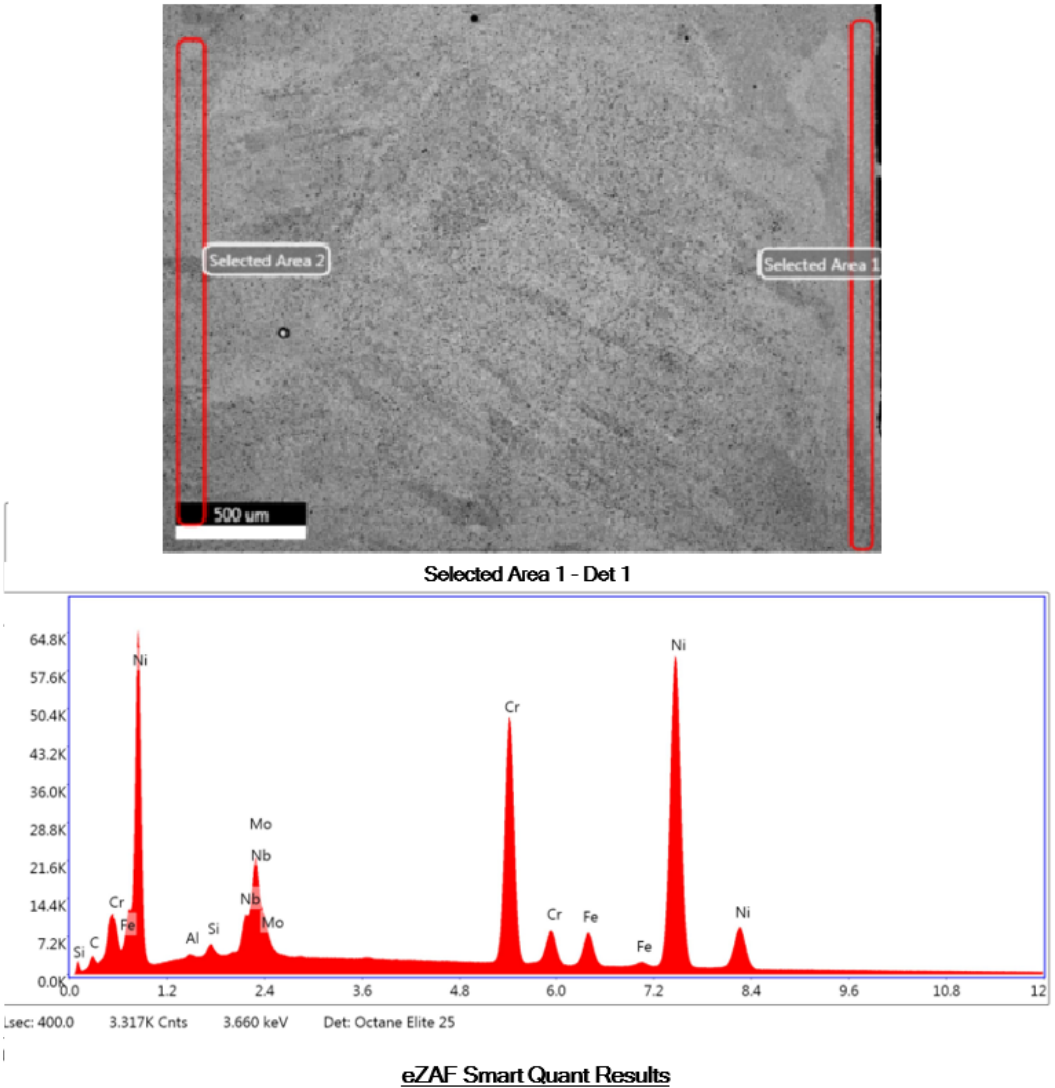

eZAF Smart Quant Results

Element	Weight %	Atomic %	Net Int.	Error %	Kratio	Z	A	F
C K	1.34	6.24	36.80	12.25	0.0032	1.3135	0.1820	1.0000
AlK	0.06	0.12	8.12	47.55	0.0002	1.1356	0.3383	1.0018
SiK	0.35	0.69	69.38	9.72	0.0019	1.1624	0.4605	1.0030
NbL	2.70	1.62	296.92	4.43	0.0192	0.9014	0.7883	1.0011
MoL	7.40	4.30	838.50	3.50	0.0545	0.8920	0.8259	1.0010
CrK	24.34	26.13	3333.75	1.92	0.2491	0.9994	0.9721	1.0531
FeK	4.55	4.55	493.26	3.06	0.0468	0.9971	0.9474	1.0892
NiK	59.26	56.34	4765.64	1.96	0.5824	1.0110	0.9661	1.0062

Figure 65: Chemical composition analysis XY-section (As-build), top surface.